A MEASUREMENT OF $\sin^2\theta_W$ FROM THE FORWARD–BACKWARD ASYMMETRY IN $p\bar{p} \to Z^0 \to e^+e^-$ INTERACTIONS AT $\sqrt{s} = 1.8$ TeV

BY

PETER TODD HURST

B.S., Massachusetts Institute of Technology, 1985
M.S., University of Illinois, 1986

THESIS

Submitted in partial fulfillment of the requirements
for the degree of Doctor of Philosophy in Physics
in the Graduate College of the
University of Illinois at Urbana-Champaign, 1990

Urbana, Illinois

MAG 2007

A MEASUREMENT OF $\sin^2\theta_W$ FROM THE FORWARD–BACKWARD ASYMMETRY IN $p\bar{p} \to Z^0 \to e^+e^-$ INTERACTIONS AT $\sqrt{s} = 1.8$ TeV

Peter Todd Hurst, Ph.D.
Department of Physics
University of Illinois at Urbana-Champaign, 1990
Professor L.E. Holloway, advisor

An analysis of the forward–backward asymmetry in Z^0 decays using data from the Collider Detector at Fermilab provides a measurement of $\sin^2\bar{\theta}_W$. The forward–backward asymmetry is measured to be $(5.2 \pm 5.9\ (\mathrm{stat}) \pm 0.4\ (\mathrm{sys}))\%$, which implies $\sin^2\bar{\theta}_W = 0.228^{+0.017}_{-0.015}\ (\mathrm{stat}) \pm 0.002\ (\mathrm{sys})$, after QCD, QED, and weak corrections. When higher order weak corrections are included, the measured value of $\sin^2\theta_W$ is consistent with previous measurements over a broad range of top quark masses.

Acknowledgments

Let me begin by thanking Melissa for guiding me through my formative years, for encouraging a critical and independent way of thinking, and for generally watching out for me. Thanks also to Lee Holloway, who first gave me the opportunity to join the CDF collaboration and gave me the freedom to pursue my interests. I'm greatly indebted to the members of the CDF collaboration and to the Fermilab Accelerator Division and the CDF support staff, who made the whole experiment work. I'm especially grateful to Ed Kearns for his considerable help during phases of my analysis, and to Craig Blocker.

Phil, Vic, and Hovhannes were (and are) a source of tremendous amusement at Fermilab, and I'm thankful for their companionship. Phil is to be commended for taking on the job of my business manager, along with his other odious tasks. Paul Tipton made me feel calm during periods of stress (as did Steve Behrends, on one notable occasion).

I'm grateful to George Brandenburg and the members of the Harvard University High Energy Physics Lab for their kind hospitality during my extended stay. Special thanks go to Ed, Rowan, Tom, Johnny, Phil, Rob, and Dave who made sure I ate nutritious meals, saw the occasional movie, and me feel at home.

I wish also to thank Fred, Toni, Tom, Matt, Brad and Robert and many others in Urbana and Boston for friendship and support over (seemingly) many years.

Lastly, and by no means least, I wish to thank my parents, my brother, and my network of other family and friends for their unflagging support, encouragement, and sense of humor. My debt to them is one I can never properly repay.

This research was supported in part by the U.S. Department of Energy under contracts DE-AC02-76ERO1195 and DE-AC02-76ER03064.

Contents

Chapter

Appendix

List of Tables

List of Figures

Chapter 1

Introduction

The Standard Model of electroweak interactions [1, 2, 3] successfully unites the electromagnetic and weak interactions, and describes a wide range of physical phenomena with great accuracy. The origins of the Standard Model lie in weak interaction phenomenology as it was understood in the late 1950's. It was recognized that the charged weak interactions share important similarities with the electromagnetic interaction, and that a unification of the two interactions might be possible. In 1961, Glashow [1] proposed a model in which the weak and electromagnetic interactions are described by vector boson fields whose operators obey an $\mathrm{SU}(2)_L \times \mathrm{U}(1)_Y$ group structure. In this model, the charged weak interactions are mediated by $\mathrm{W}^{\pm}$ bosons, and the electromagnetic interaction is mediated by the photon. The model also predicts the existence of a new Z^0 boson, which mediates a neutral weak interaction, and predicts many of the properties of the neutral current interaction. The neutral current predicted by Glashow was first observed in neutrino interactions in 1973 [4], and the W [5] and Z^0 [6] bosons themselves were later observed at the CERN proton–antiproton collider. At present, many experiments are probing the detailed structure of the Standard Model, checking for consistency and searching for new phenomena.

This thesis describes a measurement of the forward–backward asymmetry in the angular distribution of electrons from $p\bar{p} \to \mathrm{Z}^0 \to e^+e^-$ events. From the asymmetry measurement one can derive a value for the “mixing angle”, θ_W. This angle describes the mixing of the SU$(2)_L$ and U$(1)_Y$ sectors of the Standard Model, and is an integral parameter of the theory. If the Standard Model is correct, then the measured values of θ_W must be the same for all physical phenomena. Measurement of the mixing angle with many different processes, then, is an important test of the consistency of the model.

Chapter 2

Theory

By 1960, the phenomenology of the charged weak interactions was beginning to be understood, but there was no complete theory, like QED, for the weak interactions. It was clear, however, that both the weak and electromagnetic interactions share important properties: each uses a single coupling constant to describe a large number of physical phenomena, and both are mediated by spin–one fields. As early as 1957 Schwinger [7] suggested that the weak and electromagnetic forces were generated by an isospin triplet of fields; the two charged fields generated the weak interactions, while the neutral field was responsible for electromagnetism. This simple model ran into phenomenological trouble, but it is of historical importance as the first to suggest that the weak and electromagnetic interactions could be unified.

In 1961, Glashow [1] proposed a "partial symmetry" for the weak and electromagnetic interactions. In this model, weak interactions are described by two components of an isotopic spin group, $\mathrm{SU}(2)_L$, which has coupling constant g and couples only to left–handed particles and right–handed antiparticles. The form of the $\mathrm{SU}(2)_L$ interaction is determined by weak interaction phenomenology. The electromagnetic interaction is included by introducing a U(1) group with coupling constant g' which couples to hypercharge, in analogy with the Gell-Mann–Nishijima [8] model relating strangeness, baryon number, isospin, and charge in strong interactions. The electric charge is given by

$$Q = I^3 + \frac{Y}{2}, \tag{2.1}$$

where I^3 is the third component of isospin, and Y is the weak hypercharge. This implies a form for the electromagnetic current:

$$j_\mu^{em} = J_\mu^3 + \tfrac{1}{2} j_\mu^Y. \tag{2.2}$$

The structure of the hypercharge interaction is determined by requiring agreement between this implied form and the observed electromagnetic interaction.

In this $\mathrm{SU}(2)_L \otimes \mathrm{U}(1)_Y$ theory of electroweak interactions, the interaction Lagrangian consists of currents coupled to vector fields, and is given by

$$\mathcal{L}_{int} = -ig(J^i)^\mu W_\mu^i - i\frac{g'}{2}(j^Y)^\mu B_\mu. \tag{2.3}$$

There are four vector fields: the three fields W_μ^i associated with the three $\mathrm{SU}(2)_L$ generators and a field B_μ associated with the $\mathrm{U}(1)_Y$ group. The charged weak interactions are mediated by two of the $\mathrm{SU}(2)_L$ fields,

$$W_\mu^\pm = \sqrt{\tfrac{1}{2}}(W_\mu^1 \mp iW_\mu^2), \tag{2.4}$$

which describe the charged W$^\pm$ vector bosons. The electromagnetic interaction is described by a linear combination of the W_μ^3 and B_μ fields. There remains, then, a second linear combination of W_μ^3 and B_μ, orthogonal to the electromagnetic combination, which describes a weak neutral current interaction. The existence of this new neutral current interaction is an important prediction of the theory.

The linear combinations of W_μ^3 and B_μ which correspond to the photon and the Z^0, the vector boson which mediates the weak neutral current, are determined by requiring that the photon and Z^0 be mass eigenstates. One then finds that the photon and Z^0 fields are given by

$$A_\mu = W_\mu^3 \sin\theta_W + B_\mu \cos\theta_W \tag{2.5}$$

$$Z_\mu = W_\mu^3 \cos\theta_W - B_\mu \sin\theta_W. \tag{2.6}$$

The mixing angle θ_W describes the mixing of the SU(2)$_L$ and U(1)$_Y$ sectors in physical processes, and is an integral parameter of the electroweak theory. The value of the mixing angle is not predicted by the theory, and must be measured experimentally.

With these forms for the physical fields, the interaction Lagrangians for the physical fields become

$$\mathcal{L}_{int}^{em} = -i(g\sin\theta_W J_\mu^3 + g'\cos\theta_W \frac{j_\mu^Y}{2})A^\mu \tag{2.7}$$

$$\mathcal{L}_{int}^{NC} = -i(g\cos\theta_W J_\mu^3 - g'\sin\theta_W \frac{j_\mu^Y}{2})Z^\mu. \tag{2.8}$$

Adopting the form for the electromagnetic current given in Equation 2.2, and equating the electromagnetic interaction given in Equation 2.7 with that of QED,

$$\mathcal{L}_{int}^{QED} = -ie(j^{em})^\mu A_\mu, \tag{2.9}$$

one finds that g, g', and the electromagnetic coupling constant e are related by

$$e = g\sin\theta_W = g'\cos\theta_W. \tag{2.10}$$

Using Equation 2.2 and the relations of Equation 2.10, the neutral current interaction of Equation 2.8 becomes

$$\mathcal{L}_{int}^{NC} = -i\frac{g}{\cos\theta_W}J_\mu^{NC}Z^\mu, \tag{2.11}$$

where the neutral current J_μ^{NC} is given by

$$J_\mu^{NC} = J_\mu^3 - \sin^2\theta_W j_\mu^{em}. \tag{2.12}$$

Equation 2.11 implies that the neutral current interaction couples with strength $g/\cos\theta_W$, while the charged current couples with strength g. The relative strength of the charged and neutral couplings is given by

$$\rho = \frac{M_W^2}{M_Z^2\cos^2\theta_W}. \tag{2.13}$$

While the model proposed by Glashow successfully unites the weak and electromagnetic interactions, it leaves some questions unanswered. First, the SU(2)$_L \otimes$ U(1)$_Y$ symmetry is "broken" – the W_μ^3 and B_μ fields do not themselves mediate physical processes, but mix to produce the photon and Z^0. Second, there is a large mass difference between the (massless) photon and the heavy particles which transmit the weak force. Both of these problems were solved in 1967 when Weinberg [2] and Salam [3] recast the Glashow model in the form of a spontaneously broken gauge symmetry. It only remained for 'tHooft [9] to prove in 1971 that the Glashow–Weinberg–Salam theory was renormalizable to complete the so–called Standard Model.

The Standard Model of electroweak interactions predicts the existence of a weak neutral interaction, and also predicts the properties of this interaction. Any test of the properties of the weak neutral interaction is therefore a direct test of the Standard Model. Many physical processes are sensitive to the value of the mixing angle θ_W, so many of the experimental tests of the Standard Model involve a measurement of θ_W, or, more commonly, $\sin^2\theta_W$. If the Standard Model is correct, then the measured values of $\sin^2\theta_W$ must be the same (after the appropriate higher order corrections) for all physical phenomena. Measurement of the mixing angle in many processes, then, is an important test of the consistency of the model.

2.1 Angular Distributions in Weak Interactions

The $SU(2)_L$ sector of the electroweak theory is left–handed; *i.e.* it couples only to left–handed fermions and right–handed antifermions. The left–handed coupling establishes a preferred direction in particle interactions and leads to parity violation, one of the most distinctive characteristics of weak interactions. The $W^\pm$ bosons, described entirely by $SU(2)_L$, violate parity maximally, while the photon is parity conserving. The Z^0, however, has both parity conserving and parity violating components. The parity violating nature of the weak interactions leads to measurable asymmetries in the angular distributions of weak processes.

Parity violation is best illustrated in the charged weak interactions, which violate parity maximally. The charged weak interaction has a vector minus axial vector form, with currents

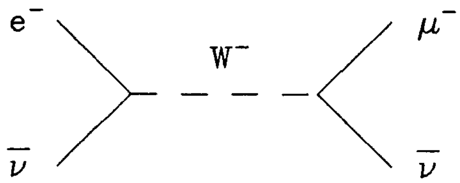

Figure 2.1: Feynman diagram for inverse muon decay, $e^-\bar{\nu}_e \rightarrow \mu^-\bar{\nu}_\mu$.

given by [10]

$$J_\mu^{weak} = \bar{\psi}\gamma_\mu\frac{1}{2}(1-\gamma^5)\psi, \tag{2.14}$$

where γ_μ and γ^5 are Dirac γ matrices. The left–handed helicity operator $\frac{1}{2}(1-\gamma^5)$ is implicit in the current. The handedness of the interaction has profound effects on the angular distribution in many reactions. An example is inverse muon decay, $e^-\bar{\nu}_e \rightarrow \mu^-\bar{\nu}_\mu$, which proceeds by virtual W$^-$ exchange as shown in Figure 2.1. In this reaction a right–handed antineutrino and a left–handed electron annihilate to produce a spin–one W$^-$ boson. The momenta and angular momentum projections for the particles are shown in Figure 2.2. Angular momentum conservation requires that the spin of the W$^-$ be aligned with the spins of the incoming fermions. When the W$^-$ decays, it produces a left–handed muon and a right–handed antineutrino. Angular momentum conservation requires that the spin polarizations of the final particles be the same as that of the parent W$^-$, which, in turn, has the same polarization as the initial particles. As a result, the decay muon is preferentially emitted in the direction of the incoming electron. In short, the left–handed coupling of the charged weak interaction establishes preferred directions for the particles' spins, and angular momentum conservation ensures that the preferred direction is maintained throughout the reaction. This is a clear violation of parity, in that the cross section changes with spatial

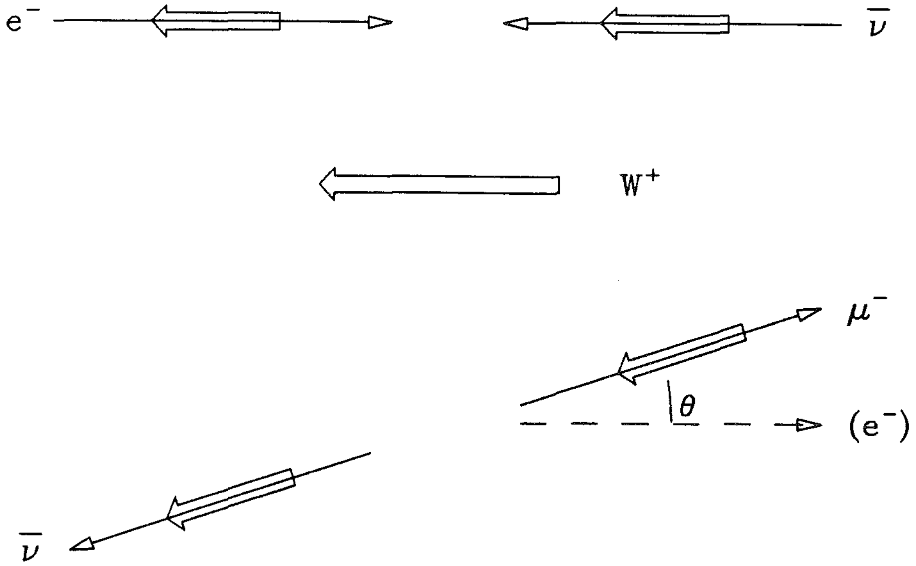

Figure 2.2: Momenta and spins in inverse muon decay, $e^-\bar{\nu}_e \rightarrow \mu^-\bar{\nu}_\mu$. A single arrow indicates the direction of a particle's momentum vector, while the double arrow shows the projection of the particle's spin.

inversion.

Assuming massless fermions, the angular distribution of the emitted muon in the inverse muon decay example is given by [11]

$$\frac{d\sigma}{d\cos\theta} = (1 + \cos\theta)^2, \tag{2.15}$$

where θ is defined to be the angle between the incoming electron and outgoing muon in the rest frame of the W$^-$, as shown in Figure 2.2. A convenient quantity for characterizing the angular distribution is the forward–backward asymmetry, A_{FB}, defined by

$$A_{\mathrm{FB}} = \frac{\int_0^1 \frac{d\sigma}{d\cos\theta}\, d(\cos\theta) - \int_{-1}^0 \frac{d\sigma}{d\cos\theta}\, d(\cos\theta)}{\int_{-1}^1 \frac{d\sigma}{d\cos\theta}\, d(\cos\theta)}. \tag{2.16}$$

The forward–backward asymmetry in inverse muon decay is 75%.

The neutral current is described as a mixture of the weak isospin and electromagnetic currents, with mixing angle θ_W, as shown in Equation 2.12:

$$J_\mu^{NC} = J_\mu^{I_3} - \sin^2\theta_W J_\mu^{EM}$$

The weak isospin component of the neutral current leads to a parity violating V − A form for the neutral current interaction, which is then slightly modified by the (vector) electromagnetic current. The relative magnitudes of the parity violating and parity conserving components of the weak neutral current are determined by the mixing angle θ_W.

The vertex factor for the neutral interaction is given by

$$\frac{-ig}{2\cos\theta_W}\gamma^\mu(I_f^3 - 2Q_f\sin^2\theta_W - I_f^3\gamma^5), \tag{2.17}$$

taking I_f^3 and Q_f to be the third component of weak isospin and the charge of the fermion, respectively. This vertex factor can be simplified using the relations of Equation 2.10 to give

$$-ie\gamma^\mu(g_V^f - g_A^f\gamma^5) \tag{2.18}$$

where the vector and axial vector fermion couplings g_V^f and g_A^f are given by

$$g_V^f = \frac{I_f^3 - 2Q_f\sin^2\theta_W}{2\sin\theta_W\cos\theta_W}, \qquad g_A^f = \frac{I_f^3}{2\sin\theta_W\cos\theta_W} \tag{2.19}$$

Due to the weak component of the neutral current interaction, the Z^0 couples more strongly, though not exclusively, to left–handed fermions and right–handed antifermions. Using the same helicity and angular momentum conservation arguments used in the charged current example, one finds that in $f\bar{f} \to Z^0 \to f'\bar{f}'$ interactions the outgoing fermion (antifermion) is preferentially emitted in the direction of the incoming fermion (antifermion). This implies that there will be an asymmetry in the decay angular distribution of the Z^0. Assuming massless fermions, the angular distribution of fermions in Z^0 production is given by [11]

$$\frac{d\sigma}{d\cos\theta} \propto ((g_V^f)^2 + (g_A^f)^2)((g_V^{f'})^2 + (g_A^{f'})^2)(1 + \cos^2\theta) + 8 g_V^f g_A^f g_V^{f'} g_A^{f'} \cos\theta \tag{2.20}$$

where θ is defined to be the angle between the incoming fermion and the outgoing fermion in the rest frame of the Z^0. The forward–backward asymmetry is given by

$$A_{\mathrm{FB}} = \frac{3 g_V^f g_A^f g_V^{f'} g_A^{f'}}{((g_V^f)^2 + (g_A^f)^2)((g_V^{f'})^2 + (g_A^{f'})^2)} \tag{2.21}$$

The magnitude of the asymmetry depends on the values of the vector and axial vector couplings of the Z^0, which, in turn, depend only on $\sin^2\theta_W$ and the (known) values of fermion charge and isospin. One can therefore infer a value for $\sin^2\theta_W$ from a measurement of the charge asymmetry in Z^0 decays.

There is another way of producing and understanding a forward–backward asymmetry, even in a theory which is parity–conserving. It was Putzolu [12] who first pointed out that asymmetries can arise from the interference between diagrams having different charge conjugation parities. Take, as an example, two Feynman diagrams which contribute to the same physical process, and have matrix elements $\mathcal{M}_1$ and $\mathcal{M}_2$. The cross section for this process is proportional to the square of the sum of the matrix elements,

$$\begin{aligned} |\mathcal{M}|^2 &= (\mathcal{M}_1 + \mathcal{M}_2)^*(\mathcal{M}_1 + \mathcal{M}_2) && (2.22) \\ &= |\mathcal{M}_1|^2 + |\mathcal{M}_2|^2 + \mathcal{M}_1^*\mathcal{M}_2 + \mathcal{M}_2^*\mathcal{M}_1. && (2.23) \end{aligned}$$

The cross section has four terms; two terms which correspond to the squares of the individual matrix elements, and two interference terms.

One can apply the charge conjugation operator to each of these matrix elements. Charge conjugation of a matrix element is mathematically well–defined, and is equivalent to exchanging all particles for antiparticles (without changing the particles' spins) and recalculating the matrix element. One finds that the matrix elements can have definite charge conjugation parities. For the purposes of this example, the matrix elements $\mathcal{M}_1$ and $\mathcal{M}_2$ are assumed to have opposite charge conjugation parities,

$$C' < \mathcal{M}_1 > \; = + < \mathcal{M}_1 > \tag{2.24}$$

$$C' < \mathcal{M}_2 > \; = - < \mathcal{M}_2 >, \tag{2.25}$$

where C' is used to imply charge conjugation. When the cross section is calculated using the charge-conjugated matrix elements, one finds

$$|\mathcal{M}|^2 = (\mathcal{M}_1 + \mathcal{M}_2)^*(\mathcal{M}_1 + \mathcal{M}_2) \tag{2.26}$$

$$= |\mathcal{M}_1|^2 + |\mathcal{M}_2|^2 - \mathcal{M}_1^*\mathcal{M}_2 - \mathcal{M}_2^*\mathcal{M}_1. \tag{2.27}$$

The interference terms in the cross section change sign under charge conjugation. Interference between diagrams with different charge conjugation parities leads to a cross section which is not invariant under charge conjugation. This charge conjugation violation can lead to a forward–backward asymmetry. The forward–backward asymmetry, then, is not evidence for parity violation; a forward–backward asymmetry can appear even in interactions (like QED) which are parity conserving. While the forward–backward asymmetry seen in Z^0 decays is due predominantly to the parity–violating nature of the weak neutral current, there are higher order QED and weak corrections which also contribute to the asymmetry. These higher order contributions are discussed in Chapter 6.

2.2 Z^0 Production in Hadronic Collisions

There are three complications which arise when considering Z^0 production in hadronic collisions. First, hadrons are not the fundamental fermions which interact to produce Z^0's. The QCD parton model describes hadrons as bound states of quarks, and it is these quarks which interact. Experimentally measured distribution functions describe the momentum distribution of the quarks inside hadrons. Since the colliding quarks generally do not have equal and opposite momenta in the lab frame, the center of mass frame of the collision moves

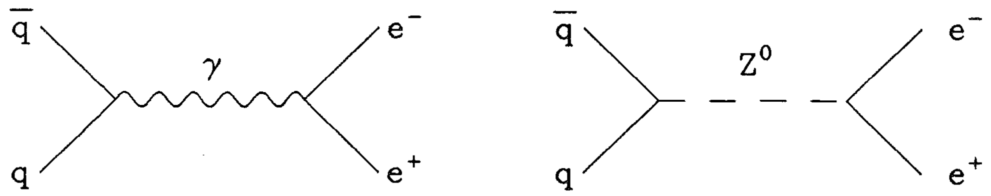

Figure 2.3: Lowest order Feynman diagrams for $p\bar{p} \rightarrow e^+e^-$.

with respect to the lab frame. Second, there is an overwhelming QCD background to the process $q\bar{q} \rightarrow Z^0 \rightarrow q'\bar{q}'$. Experimentally, then, one can distinguish only the leptonic decays of Z^0's produced in hadronic collisions. This thesis examines only the process $q\bar{q} \rightarrow Z^0 \rightarrow e^+e^-$. Third, at lowest order, both photon exchange and Z^0 exchange contribute to electron pair production in hadronic collisions; the Feynman diagrams for these processes are shown in Figure 2.3. Any measurement must include the effects of both of these processes.

A calculation of the cross section for $p\bar{p} \rightarrow e^+e^-$ based on the diagrams of Figure 2.3 gives [13, 14]

$$\begin{aligned} \frac{d\sigma}{d\cos\hat{\theta}} = {} & \frac{1}{3} \int_0^1 dx_a \int_0^1 dx_b \sum_q q(x_a,\hat{s})\bar{q}(x_b,\hat{s}) \left(\frac{\pi\alpha^2}{2\hat{s}}\right) \Big\{ Q_q^2 Q_e^2 (1+\cos^2\hat{\theta}) \\ & + 2Q_q Q_e \mathrm{Re}\chi(\hat{s})[g_V^e g_V^q (1+\cos^2\hat{\theta}) + 2g_A^e g_A^q \cos\hat{\theta}] \\ & + |\chi(\hat{s})|^2 [((g_V^e)^2 + (g_A^e)^2)((g_V^q)^2 + (g_A^q)^2)(1+\cos^2\hat{\theta}) + 8g_V^e g_A^e g_V^q g_A^q \cos\hat{\theta}] \Big\} \end{aligned} \tag{2.28}$$

where $\hat{\theta}$ is defined to be the angle between the outgoing electron and incoming quark (or outgoing positron and incoming antiquark) in the rest frame of the electron pair, as shown in Figure 2.4. The leading factor of 1/3 is a color factor which comes from averaging over initial quark color states. The functions $q(x_a, \hat{s})$ and $\bar{q}(x_b, \hat{s})$ are the quark momentum distribution functions in the proton and antiproton; x_a and x_b are the momentum fractions

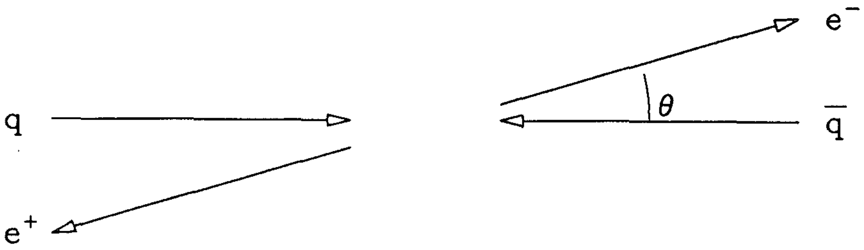

Figure 2.4: $\hat{\theta}$, the angle between the outgoing electron and the incoming quark in the rest frame of the electron pair.

carried by the quark and antiquark, and $\hat{s}$ is the square of the center of mass collision energy. The sum is over quark species. The Z^0 propagator $\chi(\hat{s})$ is given by

$$\chi(\hat{s}) = \frac{\hat{s}}{\hat{s} - M_Z^2 + iM_Z\Gamma_Z}. \tag{2.29}$$

The first and third terms in the cross section are due to photon exchange and Z^0 exchange, respectively, while the second term arises from the quantum mechanical interference of these two subprocesses. Each term has a component proportional to $(1 + \cos^2\hat{\theta})$ which is symmetric in $\cos\hat{\theta}$, and both the Z^0 and interference terms have antisymmetric components proportional to $\cos\hat{\theta}$. The antisymmetric component of the interference term comes from interference between the photon and the axial vector component of the Z^0 and leads to observable asymmetries away from the region of the Z^0 resonance. These asymmetries have been observed in $e^+e^- \to \mu^+\mu^-$ and $e^+e^- \to \tau^+\tau^-$ interactions by many experiments [15]. The photon-Z^0 interference term is antisymmetric in $\hat{s}$ with respect to $\hat{s} = M_Z^2$. While the interference term is important in the charge asymmetries seen away from the Z^0, its contribution to the forward–backward asymmetry in a region symmetric in $\hat{s}$ about $\hat{s} = M_Z^2$ is small (of order 1.5% for the region $75 < \sqrt{\hat{s}} < 105$ GeV).

The measured asymmetry in $p\bar{p} \to Z^0 \to e^+e^-$ depends on the quark momentum distribution functions in two ways. First, the asymmetry is a function of both the quark couplings and the lepton couplings to the Z^0. Since the u–type and d–type quark couplings to Z^0's are different, the observed asymmetry depends on the relative contributions of u–type quarks and d–type quarks in Z^0 production. Second, $\hat{\theta}$ is properly defined by the quark and antiquark directions. In practice, only the directions of the protons and antiprotons are known; one assumes that the initial quark is moving in the proton direction and the initial antiquark is moving in the antiproton direction. While this is always true for interactions involving valence quarks, it is wrong half the time for interactions in which both quarks come from the Fermi sea. Since the sign of $\cos\hat{\theta}$ is mismeasured for half of the sea–sea interactions, the sea–sea interactions give a symmetric "background" contribution to the angular distribution. Any determination of $\sin^2\theta_W$ from the asymmetry, then, will depend on the size of the sea–sea contribution to Z^0 production.

Figure 2.5 shows the forward–backward asymmetry integrated over the region $75 < \sqrt{\hat{s}} < 105$ GeV as a function of $\sin^2\theta_W$. The dotted and dashed curves are for $u\bar{u} \to e^+e^-$ and $d\bar{d} \to e^+e^-$ processes, respectively, while the solid line shows the asymmetry in $p\bar{p} \to e^+e^-$ interactions, assuming the EHLQ 1 [16] parametrization of the proton and antiproton momentum distribution functions. Note that the asymmetry goes to 0 near $\sin^2\theta_W = 0.250$. When $\sin^2\theta_W$ equals 0.250, the vector coupling of the Z^0 to charged leptons is 0, and the asymmetry in $q\bar{q} \to e^+e^-$ due to Z^0 exchange goes to zero. There is a small residual contribution to the asymmetry from the γ-Z^0 interference term in the cross section, which causes the asymmetry to go to zero at a value of *sinthe* near 0.245. For values of $\sin^2\theta_W$ near the expected value of 0.23 [17], the asymmetries for u–type and d–type quarks are very similar, and so the measured asymmetry in $p\bar{p}$ interactions is expected to be rather insensitive to the relative size of the u–type and d–type contributions to Z^0 production. At $\sin^2\theta_W = 0.23$, the expected asymmetry in $p\bar{p}$ interactions for EHLQ 1 distribution functions in the region $75 < \sqrt{\hat{s}} < 105$ GeV is 5.54%.

It is clear from Figure 2.5 that there may be more than one value of $\sin^2\theta_W$ which pro-

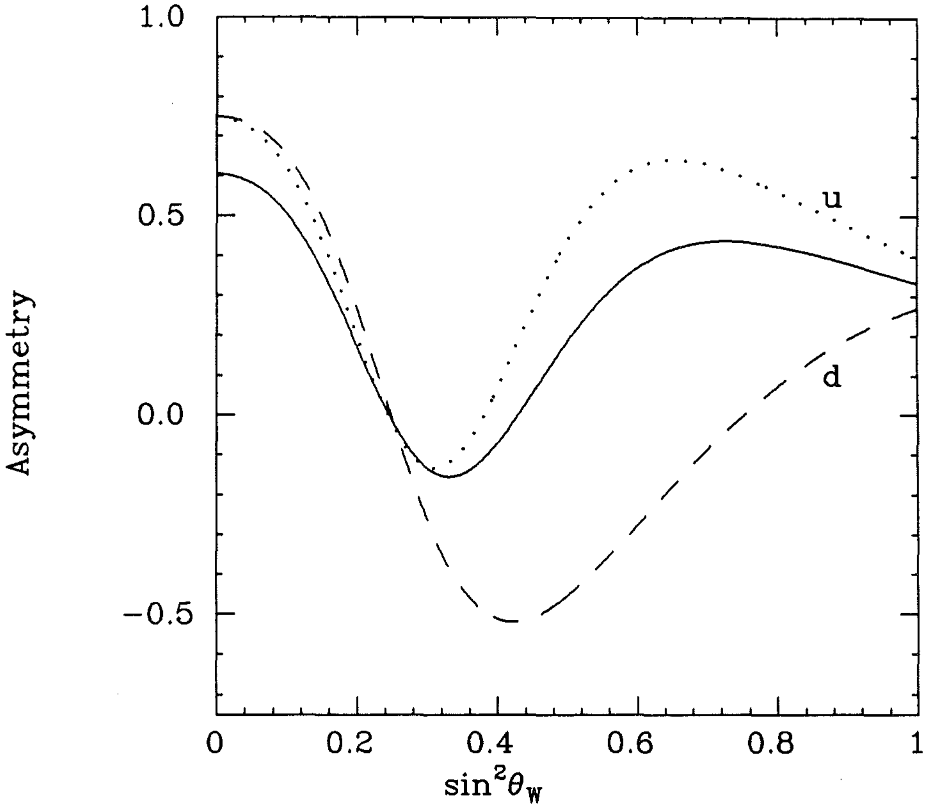

Figure 2.5: Forward–backward asymmetry as a function of $\sin^2 \theta_W$. The dotted curve shows the u–type asymmetry while the dashed curve shows the asymmetry for d–type quarks. The solid curve is the observed asymmetry for EHLQ 1 momentum distribution functions.

duces a given forward–backward asymmetry. When solving for the $\sin^2\theta_W$ value associated with the measured asymmetry, there may be more than one solution. The value of $\sin^2\theta_W$ is constrained to be near 0.23 by other neutral current data [17], and so the solution nearest this expected value is used.

Due to QCD effects such as initial state gluon bremsstrahlung, the Z^0's are produced with varying amounts of transverse momentum, p_t^Z. When a Z^0 is produced with non–zero p_t^Z, the proton and antiproton directions are not collinear in the rest frame of the dileptons, and so the quark directions are not completely determined; the quarks can only be said to be travelling in approximately the direction of the proton or antiproton, and the approximation gets worse as p_t^Z increases. Since the initial quark directions are ill–defined, $\cos\hat{\theta}$ can no longer be precisely measured. One must therefore define a new $\hat{z}$ axis in the dilepton rest frame to take the place of the quark direction when making angular measurements. Several definitions have been proposed [18]. For this thesis, the method of Collins and Soper [19], in which the $\hat{z}$ axis is taken to be the bisectrix of the proton and minus the antiproton directions, as shown in Figure 2.6, is chosen. In effect, the Collins–Soper definition divides the p_t^Z contribution equally between the quark and antiquark, and possesses the feature that $\hat{z}$ reduces to the quark direction in the limit $p_t^Z \to 0$. A Lorentz–invariant form for $\cos\hat{\theta}$ as defined by Collins and Soper is given by [19]

$$\cos\hat{\theta} = \frac{(P_{e^-}^0 + P_{e^-}^3)(P_{e^+}^0 - P_{e^+}^3) - (P_{e^-}^0 - P_{e^-}^3)(P_{e^+}^0 + P_{e^+}^3)}{M_{e^+e^-}\sqrt{M_{e^+e^-}^2 + P_T^2}}, \tag{2.30}$$

where $P_{e^-}^\mu$ and $P_{e^+}^\mu$ are the electron and positron 4–vectors, and $M_{e^+e^-}$ is the dielectron invariant mass.

All of the alternate, p_t^Z dependent, definitions of $\hat{\theta}$ are approximations which begin to break down for Z^0's with large transverse momentum. The $\cos\hat{\theta}$ distribution will therefore be smeared somewhat by the high p_t^Z events, and the observed angular distribution will be flatter and more symmetric than that predicted by the lowest order cross section. While the Collins–Soper definition is used in the measurement of $\cos\hat{\theta}$ in the data, $\sin^2\theta_W$ is

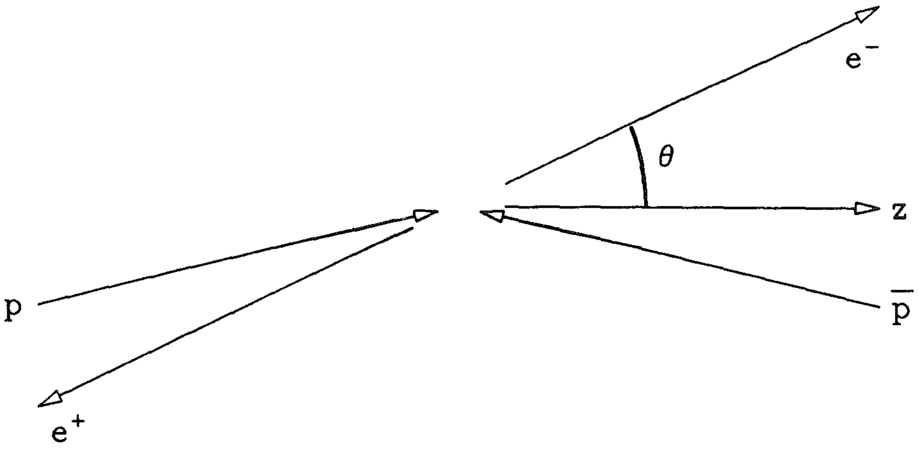

Figure 2.6: The Collins–Soper definition of the angle $\hat{\theta}$. The $\hat{z}$ axis bisects the proton and minus the antiproton directions.

extracted based on the lowest order cross section of Equation 2.29. The effect of the $\cos\hat{\theta}$ smearing on the measurement of $\sin^2\theta_W$ must be determined. The size of this smearing effect is discussed in Chapter 6.

2.3 Higher Order Effects

There are many higher order diagrams which contribute to dielectron production in hadronic collisions, and some of these diagrams affect the measured asymmetry. The higher order QCD processes which produce Z^0's with transverse momentum smear out the angular distribution somewhat. Many higher order QED processes contribute directly to the asymmetry. The size of all of these contributions to the asymmetry must be calculated before one can extract a meaningful value for $\sin^2\theta_W$ from the asymmetry measurement. Furthermore, when higher order weak effects are included, values for $\sin^2\theta_W$ determined from different physical processes get different corrections and are no longer directly comparable [20]. In particular, the value of $\sin^2\theta_W$ determined from the charge asymmetry is not directly comparable to the value determined from the measurement of the W and Z^0 masses, $\sin^2\theta_W = 1 - M_W^2/M_Z^2$, until higher order corrections are made and a particular definition for $\sin^2\theta_W$ is adopted. The calculation of these higher order effects is complicated, and further discussion is deferred to Chapter 6.

Chapter 3

The CDF Experiment

The CDF experiment has two main components: the combination accelerator and storage ring system which produces collisions between protons and antiprotons, and the CDF detector, which analyzes the final state particles produced when a proton and antiproton collide. This chapter contains a brief description of the accelerator, and describes the detector elements used in the current analysis.

3.1 The Accelerator

The accelerator complex at the Fermi National Accelerator Laboratory contains seven separate accelerator/storage components. Figure 3.1 shows an overhead view of the Fermilab accelerator complex. A Cockroft–Walton generator (not shown in Figure 3.1) produces a beam of 750 keV H^- ions, which is then injected into a linear accelerator. The linear accelerator accelerates the H^- ions to approximately 500 MeV, and injects them into the circular Booster ring. The Booster accelerates the beam of ions to 8 GeV, strips both electrons off of the H^- ions to leave bare protons, and injects the protons into the Main Ring. The Main Ring is a proton synchrotron 2 kilometers in diameter. It was once used to produce beams of 400 GeV protons for use in fixed target experiments, but now serves as an injector

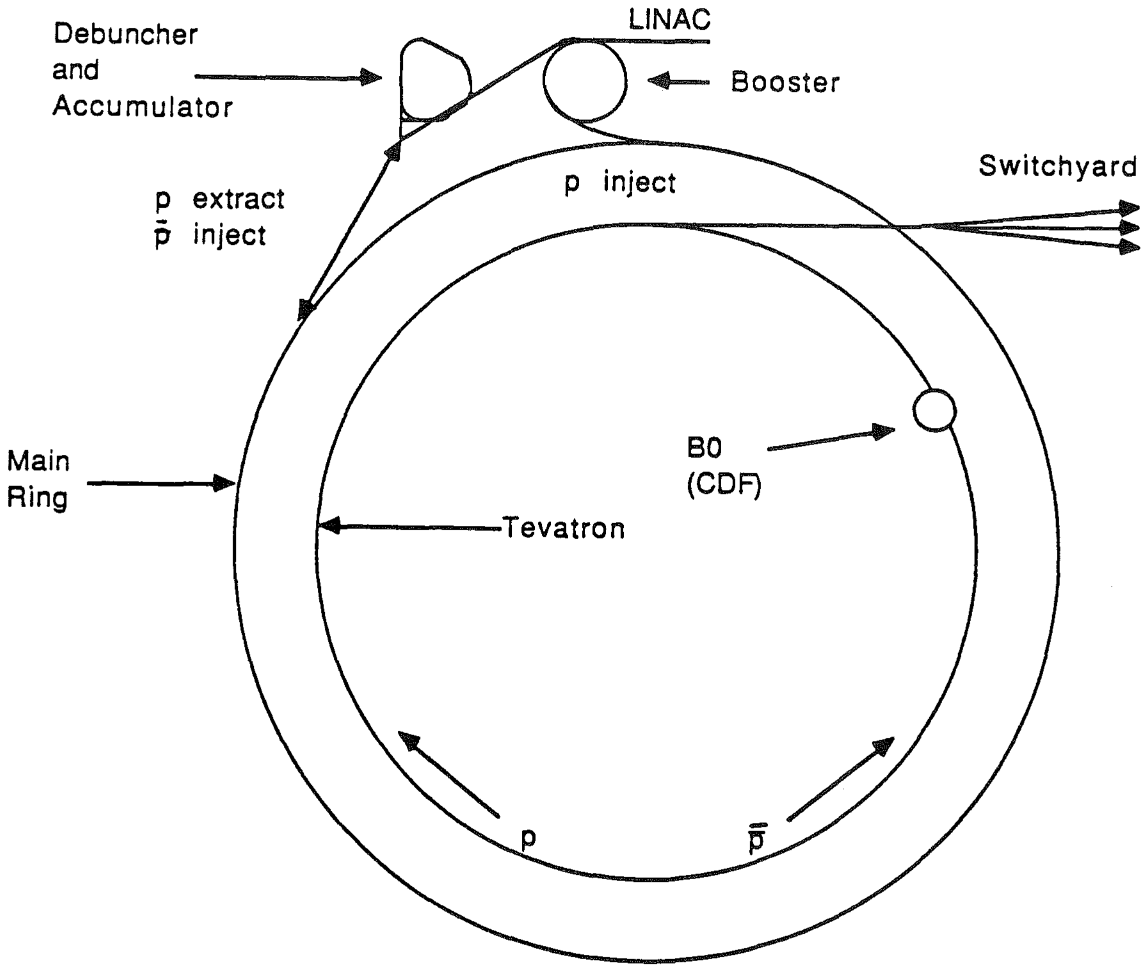

Figure 3.1: An overhead view of the Fermilab accelerator complex. The fixed target beam lines are shown, as is the position of the B0 intersection region where the CDF detector is located.

for the Tevatron ring and as a source of 120 GeV protons for antiproton production. The Tevatron accelerator uses a ring of superconducting magnets, and is housed in the same 2 km diameter tunnel as the Main Ring. The Tevatron accepts 150 GeV particles from the Main Ring and accelerates them to 900 GeV.

The antiproton production system produces antiprotons with a large initial energy spread, and then uses two storage rings to reduce this energy spread and store a nearly monoenergetic beam of antiprotons. Antiprotons are produced when 120 GeV protons from the Main Ring hit a tungsten target. The antiprotons are focused by a current pulsed lithium lens, and are then directed into a storage ring called the Debuncher. The antiprotons enter the Debuncher in a short time pulse, and have energies of approximately 8.5 GeV with an energy spread of about 2%. Two techniques are used in the Debuncher to reduce the energy spread and the transverse motion of the beam; bunch rotation and stochastic cooling [21]. Bunch rotation is a radio frequency technique in which the energy spread of an antiproton pulse is reduced by increasing its time spread. In stochastic cooling, a probe senses the position of the beam, and sends a signal across a chord of the accelerator ring to a kicker. The kicker then applies a correction to the beam as it passes by. After two seconds in the Debuncher, the beam is directed into the Accumulator, where it undergoes further stochastic cooling. The Accumulator is used both to cool the antiprotons and to store them, and accepts a new antiproton pulse from the Debuncher every two seconds. After several hours in the Accumulator, the antiprotons end up in a tight core with a very narrow energy distribution.

When a sufficient number of antiprotons have been collected, six bunches of antiprotons are extracted from the core in the Accumulator, and injected into the Main Ring. There they are accelerated to 150 GeV and injected into the Tevatron, where six bunches of protons are already circulating. Since protons and antiprotons have opposite charges, the proton and antiproton bunches will circulate in opposite directions inside the same accelerator ring. The 6 antiproton bunches will intersect with the 6 proton bunches at 12 points around the accelerator ring. A radio frequency process called cogging moves the intersection points around the ring so that one of the 12 intersections is located inside the CDF detector. When the proton and antiproton bunches are aligned properly, they are simultaneously accelerated to 900 GeV.

The rate at which the protons and antiprotons collide is characterized by a quantity called luminosity. The luminosity is given by

$$\mathcal{L} = \frac{N_p N_{\bar{p}} C}{4\pi\sigma^2}, \tag{3.1}$$

where N_p and $N_{\bar{p}}$ are the number of protons and antiprotons per bunch, C is the bunch crossing rate, and σ is the rms width of the Gaussian beam profile. (The proton and antiproton beams are assumed to have the same rms width, and the beams are assumed to overlap completely.) The rms width for particle beams is related to the beam emittance ϵ and the accelerator β function by

$$\sigma^2 = \frac{\epsilon\beta(s)}{6\pi}. \tag{3.2}$$

The emittance ϵ is a measure of the transverse phase space occupied by the beam. It is independent of the beam's position around the ring, but grows with time. The beta function $\beta(s)$ describes the transverse envelope of the beam. $\beta(s)$ is determined by the focusing magnets in the accelerator, and varies with s, the position around the accelerator ring. Superconducting quadrupole magnets located on either side of and near to the nominal collision point reduce the β function at the collision point, thereby reducing σ and increasing the luminosity. The luminosity falls exponentially as a function of time, due to emittance growth and proton and antiproton losses due to collisions. Characteristic beam lifetimes are of the order of 12 hours.

The total inelastic cross section for $p\bar{p}$ interaction at 1.8 TeV is approximately 70 mb, where one barn (b) is 10^{-24}cm^2. A large fraction of the total inelastic cross section consists of small angle scattering in which the final state particles escape undetected down the beam pipe. Two planes of scintillator counters, discussed in Section 3.2.4, surround the beam

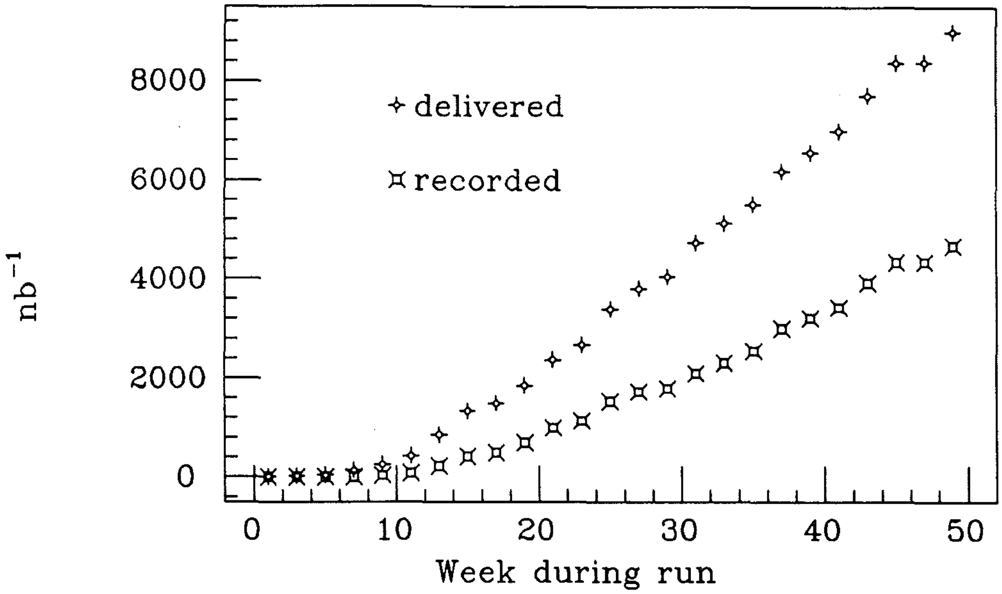

Figure 3.2: The integrated luminosities delivered by the accelerator and recorded by the CDF detector.

pipe and detect final state particles which are emitted at angles greater than approximately 1.25° with respect to the proton and antiproton beams. These scintillator counters signal the presence of an inelastic collision and are used to trigger the readout of the detector. The effective cross section seen by the scintillator counters is approximately 44 mb; *i.e.* the inelastic cross section for $p\bar{p}$ interactions in which final state particles are produced at angles greater than 1.25° is 44 mb. At a luminosity of $2 \times 10^{30}\text{cm}^{-2}\text{s}^{-1}$, the CDF detector observes $p\bar{p}$ collisions at a rate of 88 kHz. At this luminosity, approximately 31% of the beam crossings produce a $p\bar{p}$ collision in which particles strike the CDF detector, and approximately 9% of the beam crossings have more than one such collision. Peak luminosities grew from $3 \times 10^{29}\text{cm}^{-2}\text{s}^{-1}$ at the beginning of the 1988-1989 data run to over $2 \times 10^{30}\text{cm}^{-2}\text{s}^{-1}$.

The integrated luminosity is a measure of the total number of collisions produced. Figure 3.2 shows the total integrated luminosity delivered by the accelerator, and the integrated luminosity collected by the CDF detector and written to tape. The overall data collection efficiency during the 1988-1989 run was approximately 50%.

3.2 The CDF Detector

The Collider Detector at Fermilab (CDF) is a large multipurpose solenoidal detector designed to observe the leptons and jets produced in $p\bar{p}$ collisions. A detailed description is given in the literature [22]. Perspective and elevation views of the CDF detector are shown in Figure 3.3. CDF uses a right handed coordinate system in which x lies in the horizontal plane, y is vertical, and z is in the direction of the proton beam. The coordinate system is indicated on the perspective view of the CDF detector in Figure 3.3 Below are descriptions of individual detector elements, with special emphasis on the elements used in the asymmetry analysis.

3.2.1 Tracking Detectors

Nearest the interaction point are eight time projection chambers (VTPC) which measure the position of the event vertex and the R-z positions of charged tracks. Together the chambers extend 2.8 m along the beam direction, centered on the nominal interaction point, and extend in radius from $R = 6.8$ cm to $R = 21$ cm. Each chamber consists of two separate drift volumes, extending 15 cm in the z direction, which are separated by a high voltage grid. Each drift volume ends in an octagonal proportional chamber endcap which is divided into octants, each octant having 24 sense wires arranged perpendicular to the radial direction. Adjacent chambers are rotated relative to one another by approximately 11° to eliminate inefficiencies at octant boundaries and provide ϕ information.

Charged particles leave ionized tracks in the drift volume as they pass through the detector. The electrons from the track drift in the z direction toward the proportional

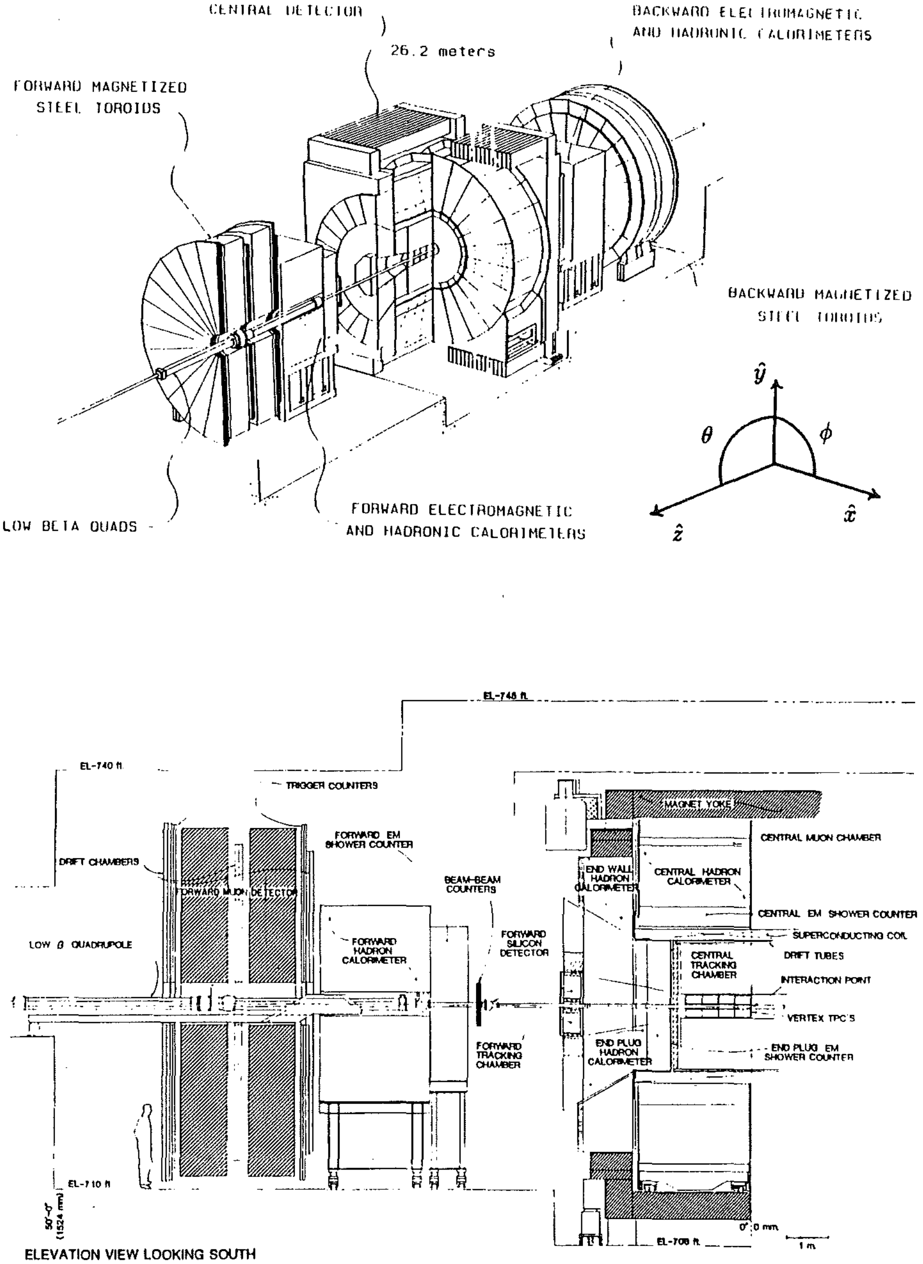

Figure 3.3: Perspective (top) and elevation views of the CDF detector. The coordinate system is indicated on the perspective view.

chamber endcap, where they are detected. The time of arrival of the electrons gives the R-z position of the track. Track positions in the z direction are measured to better than $500\mu m$. By extrapolating the R-z VTPC tracks back to the beam axis, one can determine the position of the event vertex (for events with only one vertex) with a resolution of 1 mm.

Surrounding the VTPC is a large cylindrical drift chamber (CTC) which is used to measure the R-ϕ position of charged particle tracks and, in conjunction with a 1.4 Tesla magnetic field, the particle momentum. The CTC extends 3.2 m in the z direction and has inner and outer radii of 0.3 m and 1.3 m, respectively. The CTC uses 84 layers of sense wires, organized into 9 "superlayers". The sense wires in each superlayer are organized into R-ϕ cells, which are tilted 45° with respect to the radial direction. The electrons from the ionized tracks drift in crossed E and B fields inside the CTC; the tilt of the R-ϕ cells compensates for the Lorentz angle of the electron drift, and ensures that the electrons move in the azimuthal direction. This azimuthal drift simplifies the conversion from time to distance. In five of the superlayers, 12 wires are strung axially along the beam direction, while in the remaining 4 superlayers 9 wires are tilted $\pm 3^\circ$ with respect to the beamline to obtain stereo information about the z positions of tracks. Figure 3.4 shows an R-ϕ view of the CTC. The superlayers and the 45° tilt of the cells can be clearly seen.

In some sense, the CTC is self–calibrating. The TDC pedestal offset (or t_0) for each channel can be determined by demanding that tracks be continuous as they cross the plane of sense wires in a single R-ϕ cell. The drift velocity is determined by demanding that the tracks be continuous as they cross the boundary between two R-ϕ cells. Knowledge of the wire positions, the t_0 offset, and the drift velocity is sufficient to convert TDC track data into R-ϕ positions. Drift velocity and t_0 data are analyzed online during each run, and written to database files for use during offline track reconstruction.

Positions along a track in the CTC are determined to better than $200\mu m$ in the R-ϕ direction and $6mm$ in the z direction. The momentum of a track is determined with a resolution $\delta p_t/p_t^2 < 0.002$ in the region $40^\circ < \theta < 140^\circ$. By constraining the track to pass

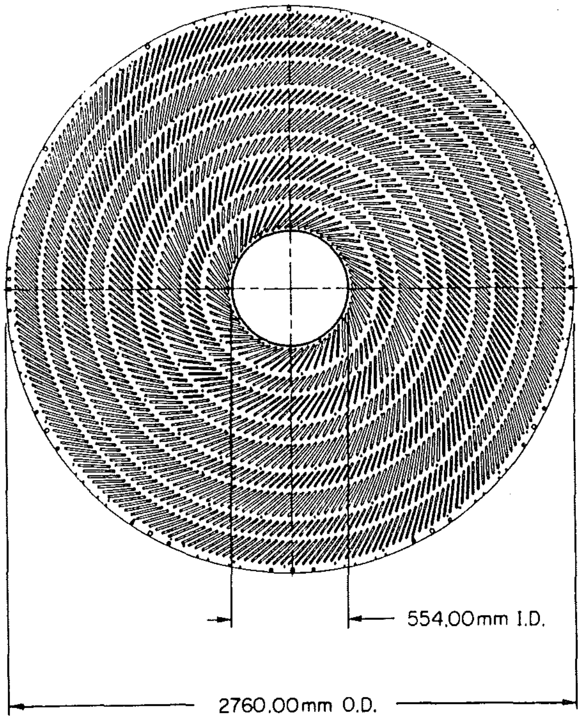

Figure 3.4: R-ϕ view of the CTC. The 9 superlayers are clearly seen, as is the 45° tilt of the R-ϕ cells.

through the nominal R-ϕ position of the beam, the effective path length of the track is extended from 1 m to 1.3 m. The momentum resolution, which goes as $1/(Bl^2)$ where l is the track length, is reduced to $\delta p_t/p_t^2 = 0.0011$.

Outside the CTC are three layers of drift tubes (CDT) which use drift times and charge division to measure the R-ϕ and z positions of tracks, respectively. Typical resolutions are 2.5 mm in the z direction and $200\mu m$ in R-ϕ.

3.2.2 Calorimeters

Electromagnetic and hadronic calorimeters are used to measure the energies and positions of electromagnetic showers and jets. Calorimeter coverage extends to within 2° of the proton and antiproton beams and covers the full azimuth. The calorimeters are mechanically divided into three subsystems (central, plug and forward) as shown in Figure 3.3. Within each calorimeter, coverage is divided into projective towers which point toward the interaction point. The polar segmentation is in units of pseudorapidity, η, where $\eta \equiv -\ln(\tan\theta/2)$. Pseudorapidity is used as an approximation to the true rapidity y, where y is defined by

$$y = \frac{1}{2}\ln\frac{E+p_z}{E-p_z} \tag{3.3}$$

Rapidity is a convenient quantity for calorimeter segmentation for jet physics. Since rapidity is an additive quantity under Lorentz boosts, both the shape of a jet in y-ϕ space (*i.e.* its extent $\Delta y \times \Delta\phi$) and the calorimeter segmentation are invariant under the longitudinal boosts inherent in $p\bar{p}$ collisions. True rapidity depends on mass, however, and for particles of different masses there is no single relation between polar angle and rapidity. Pseudorapidity is a simple approximation which gives good results for particle with energies very much larger than their masses. In the central region ($|\eta| < 1.1$), each projective tower subtends 15° in ϕ and 0.1 unit of pseudorapidity η. In the plug ($1.1 < |\eta| < 2.2$) and forward ($2.2 < |\eta| < 4.2$) regions, the towers subtend 5° in ϕ and 0.1 units of η.

All of the calorimeters are of the sampling variety: they use alternating layers of absorber

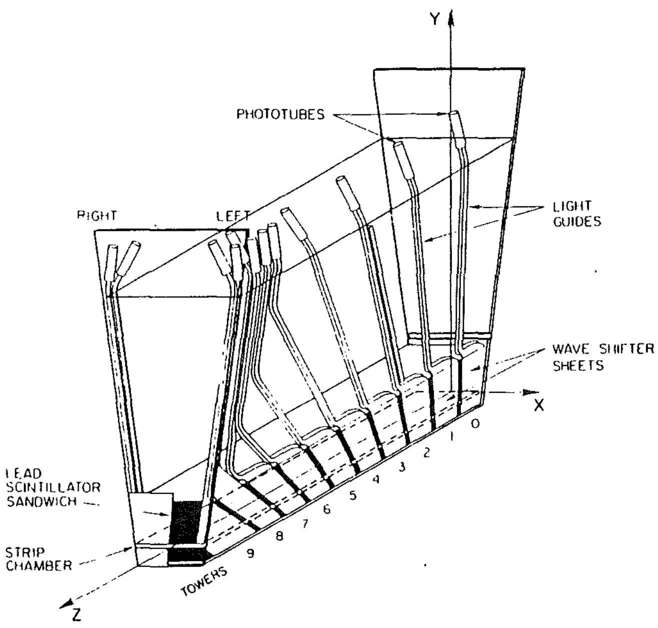

Figure 3.5: Cutaway view of a central calorimeter wedge showing the central electromagnetic calorimeter and light transmission system.

in which the incident particles shower and an active material which samples the energy flow of the showers. In the central region plastic scintillator is used as a sampling medium in both the electromagnetic and hadronic calorimeters. The plug and forward calorimeters use proportional tube chambers with segmented cathode pad readout.

Central Calorimeters

The central electromagnetic (CEM) and central hadronic (CHA) calorimeters are constructed in 15° wedges, which are then assembled to form a barrel with full azimuthal coverage. Figure 3.5 is a cutaway view of a central calorimeter wedge showing the electromagnetic calorimeter. The CEM calorimeter is a sandwich of 31 layers of 5 mm thick polystyrene scintillator and 30 layers of $\frac{1}{8}$ inch thick aluminum clad lead sheets. To maintain a constant thickness in radiation lengths as polar angle changes, some lead is replaced with acrylic and the scintillator behind the acrylic is painted black. On average, each tower is 18 radiation lengths thick. The scintillator light is collected through wavelength shifters on both sides of the wedge. The wavelength shifters transmit the light to acrylic light guides which are attached to photomultiplier tubes located at the rear of each wedge.

Each of the CEM towers has been calibrated using 50 GeV electrons from a test beam. This calibration has been maintained to approximately 2.5% over several years by means of a cross calibration to Cs^{137} source signals. A map of the response across the face of an individual tower has also been obtained from the test beam. The response is found to vary by some 6% across the face of a tower, due to shower leakage at the edges of the calorimeter and to variations in light collection in the scintillator–wavelength shifter system. The measured energy resolution for electromagnetic showers is

$$\left(\frac{\sigma_E}{E}\right)^2 = \left(\frac{13.5\%}{\sqrt{E\sin\theta}}\right)^2 + (1.7\%)^2, \tag{3.4}$$

where the constant term is the average uncertainty in the individual tower calibrations.

A gas proportional strip chamber (CES) is embedded in the CEM calorimeter near shower maximum to measure the shape and position of electromagnetic showers. Wires run parallel to the beam direction and give a ϕ view of electromagnetic showers, while cathode strips are positioned perpendicular to the wires and provide z information. Typical position resolutions are 2 mm in both the strip and wire views for 50 GeV electrons from a test beam.

The central hadronic (CHA) and endwall hadronic (WHA) calorimeters measure the hadronic energy in the central region. The CHA modules are located in the wedges just behind the CEM. They are constructed from a sandwich of 32 layers of 1.0 cm scintillator and 2.5 cm steel. The WHA calorimeter occupies the transition region between the central barrel and the plug. Because the particle energies here are greater for the same transverse energy E_T, the steel of the WHA is thicker than that of the CHA. The WHA is a sandwich of 15 layers of 1.0 cm scintillator and 5.0 cm steel. As in the CEM, the scintillator light from the CHA and WHA is read out through a system of wavelength shifters and acrylic

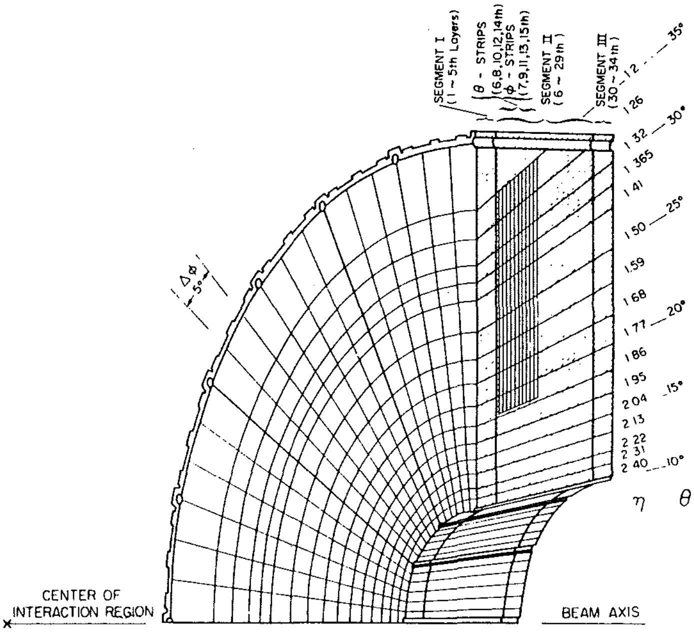

Figure 3.6: View of a plug electromagnetic calorimeter quadrant.

light guides. Pions from a test beam are used to calibrate both the CHA and the WHA, and the calibration is maintained with Cs^{137} sources. The typical resolution (σ/E) for 50 GeV pions is 11% for the CHA and 14% for the WHA.

Plug Calorimeters

The plug electromagnetic (PEM) and plug hadronic (PHA) calorimeters cover the polar angles from 10° to 30° and 150° to 170° ($1.1 < |\eta| < 2.4$). The PEM calorimeters are divided into 4 quadrants, and consist of 34 layers of proportional tubes alternating with 2.7 mm lead sheets. A PEM quadrant is shown in Figure 3.6. The proportional tubes are made of a resistive plastic and are epoxied to sheets of copper–clad G10 which have been etched to form projective towers of cathode pads. When a particle showers in the calorimeter, the gas in the proportional tubes is ionized. The electrons move quickly toward the anode wire, leaving a cloud of slowly moving positive ions behind. These positive ions induce a charge on the cathode pads, which is integrated by the front end electronics. The cathode pads in the PEM are ganged to form projective towers with three depth segments, containing 5, 24, and 5 layers. The depth segmentation provides information about the longitudinal development of electron showers. The anode signals for each layer in the quadrant are also read out, and provide additional longitudinal information. Ten layers of the PEM near shower maximum in the region $1.2 < |\eta| < 1.9$ are equipped with finely segmented η and ϕ cathode strips as well as cathode pads. The strips are used to provide better position and shape resolution for electromagnetic showers.

The gain of the proportional tubes is a function of the density and composition of the gas which flows through them. This so–called gas gain is monitored by a system of small proportional tubes and Fe^{55} sources. The 6 keV photon from the Fe^{55} source deposits a known amount of energy in the monitor tube. By measuring the charge collected on the anode wire of the monitor tube, one can measure the gain of the gas. The response of the calorimeter as a function of gas gain is determined during the test beam calibration, and the data are adjusted online for the gas gain on a run by run basis before being written to tape.

The resolution function of the PEM is determined from studies of electrons from a test beam and is found to be

$$\frac{\sigma}{E} = \frac{28\%}{\sqrt{E}} + 2\%. \tag{3.5}$$

The PHA calorimeters are divided into twelve 30° stacks, and consist of 20 layers of proportional tubes separated by 5 cm of steel. The cathode pads are ganged to form projective towers, and anode signals are read out of each layer of the stacks. As with all gas calorimeters, the calorimeter response is a function of the gas gain, and the data are corrected for gas gain variations before being written to tape. The resolution of the PHA is determined from studies of pions from a test beam and is found to be

$$\frac{\sigma}{E} = \frac{86\%}{\sqrt{E}} + 4\%. \tag{3.6}$$

Forward Calorimeters

The forward electromagnetic (FEM) and hadronic (FHA) calorimeters cover the region from 2° to 10° ($2.4 < \eta < 4.2$). The FEM is divided into quadrants, and consists of a sandwich of 30 layers of proportional tubes and 4.5 mm lead sheets. The cathode pads are ganged in groups of 15 layers to form projective towers with two depth segments. Each 90° anode plane is divided into 5 anode regions, each of which is read out separately. The energy response to electrons from a test beam is linear up to 100 GeV, and the resolution is determined to be

$$\frac{\sigma}{E} = \frac{25\%}{\sqrt{E}} + 0.5\%. \tag{3.7}$$

The FHA is also divided into quadrants, and is composed of 27 layers of proportional tubes and 5 cm steel plates. Each anode plane is divided into 6 regions, which are read out in addition to the projective towers of cathode pads. The low-β quadrupoles of the accelerator penetrate into the FHA, and require part of the small angle coverage to be cut away. The FHA covers the full azimuth only for $|\eta| < 3.6$. The FHA energy resolution is approximately

$$\frac{\sigma}{E} = \frac{140\%}{\sqrt{E}}. \tag{3.8}$$

Data from both the FEM and the FHA are corrected for variations in gas gain before being written to tape.

3.2.3 Muon Detectors

Although not used in this analysis, the muon detectors are a source of important physics which is, in some sense, complimentary to the physics derived from electron measurements. There are two muon detection systems at CDF: a set of muon chambers located in the central wedges, and toroidal muon spectrometers located behind the forward calorimeters. The central muon (CMU) chambers consist of four layers of drift tubes and are located inside the central calorimeter wedges, behind the CHA. The muon chambers cover the angular region $56° < \theta < 124°$, and the full azimuth. Tracks found in the muon chambers are matched to CTC tracks for momentum measurement. The forward muon spectrometers (FMU) cover the regions from 3° to 16° and 164° to 177°. Each spectrometer consist of two magnetized steel toroids with three layers drift chambers and two layers of scintillation counters. Tracks are reconstructed with a momentum resolution of 13%, and are matched to VTPC tracks. The scintillation counters provide trigger information.

3.2.4 The Trigger

The trigger system makes use of two planes of scintillator counters (beam–beam counters, or BBC) mounted on the front face of the forward calorimeters. Each scintillator plane consists of 16 scintillator paddles arranged in a square about the beam pipe and covering the region $3.2 < \eta < 4.5$. Hits in the BBC signal that an inelastic $p\bar{p}$ collision has taken place. In addition to its trigger duties, the BBC is the primary luminosity monitor, provides a measurement of the time of the interaction for the tracking chambers, and can make a crude measurement of the vertex position.

The CDF trigger is itself a four–level combined hardware and software system. The initial level (Level 0) is the minimum bias trigger. It requires at least one of the 16 trigger counters on each side of the interaction to fire within a 15 ns window centered on the beam crossing. The Level 0 decision is available within 100 ns of the collision. After a valid Level 0 trigger, data taking is inhibited to give the next trigger levels time to make decisions.

The Level 1 calorimeter trigger uses fast analog signals from the front end electronics. Signals are ganged into trigger towers measuring $\Delta\eta = 0.2$ by $\Delta\phi = 15°$, and are weighted by $\sin\theta$ to provide a crude estimate of transverse energy. Analog comparators and summers look for trigger towers with large energy depositions and calculate the total scalar transverse energy in the event. The Level 1 trigger decision is made within $7\mu s$. If there is no valid Level 1 trigger, the front end electronics are reset, in time for the second beam crossing after the initial Level 0 trigger. If a valid Level 1 trigger exists, data taking remains inhibited and the Level 2 trigger takes over.

The Level 2 trigger digitizes the fast analog signals used in Level 1, and has access to data from fast hardware track processors. Level 2 uses the digitized calorimeter information to form energy clusters. The cluster energies, positions, and widths are then passed, along with track information, to a set of programmable processors. These processors apply simple algorithms for identifying physics signals and generate the Level 2 trigger decision. The Level 2 decision is made, on average, in approximately $20\mu s$, although this time can vary with the complexity of the event and the processor algorithms. If there is no valid Level 2 trigger, the front end electronics are reset and data taking is resumed. If a valid Level 2 trigger exists, then the entire detector is digitized and the digitized data is formatted. The formatted event is sent to the Level 3 processors for further analysis, and the front end electronics are reset after readout.

The Level 3 trigger is software–based. An entire formatted event is loaded into one of 60 Motorola 68020 based microprocessors, each of which is capable of running the CDF offline analysis code. The Level 3 trigger has access to all the data in an event, and uses streamlined versions of the offline reconstruction algorithms to harden the Level 2 trigger thresholds. Events passing the Level 3 selection algorithms are written to tape.

Chapter 4

Event Reconstruction and Selection

Event reconstruction begins with the raw ADC and TDC data which is written to tape, and ends with a sample of identified Z^0 and photon events. This chapter describes the reconstruction steps and the event selection criteria which culminate in the final sample of Z^0 events.

4.1 Energy Reconstruction

Jets and electrons are reconstructed from the calorimeter ADC data. The raw calorimeter ADC data are corrected for amplifier gain, gas gain, and gross pedestal offsets by the data acquisition system before being written to tape. Small pedestal shifts are subtracted in the offline analysis. The ADC data are converted to energies by multiplying by a detector dependent conversion factor determined from studies of testbeam data. Due to broken wires, some anode planes in the gas calorimeters are turned off, reducing the signal seen in the ganged cathode pad towers. Tower energies are corrected to compensate for these dead anode planes. The ADC to energy conversion produces an η-ϕ array of calorimeter tower energies and lists of anode plane energies.

There are four types of noise in the calorimeter tower array which must be removed before further processing. First, single phototubes in the central calorimeters can give anomalously large signals, due to high voltage breakdown within the phototube or from Cerenkov light from particles which shower in the lightguides. Each calorimeter tower is viewed by two phototubes, and real energy can be distinguished from noise by requiring that both phototubes register the presence of energy.

Second, low energy neutrons produced in hadronic showers indirectly produce large energy deposits in the gas calorimeters. These low energy neutrons are able to penetrate the calorimeters, and have a large cross section for interactions with protons. The neutrons knock loose protons from the hydrogen rich ethane gas filling the proportional tubes or from the plastic walls of the proportional tubes in the plug calorimeters. These protons range out quickly, losing all their energy through ionization of the gas in the proportional tube. This ionization appears as a large energy deposit over a small number of cathode pads in a single layer of the calorimeter. This noise is removed by an algorithm which searches for highly localized energy depositions.

Third, there is occasional high voltage leakage from the ends of the PEM proportional tubes. This produces a large signal in a single anode layer and in a small number of cathode pads near the perimeter of the PEM. The same algorithm which removes the neutron noise removes these localized energy spikes.

Fourth, ground loops in the signal cables running from the calorimeters to the front end electronics produce purely electronic noise in the PHA and FHA. Each ribbon cable carries signals from 12 adjoining calorimeter towers. The cable noise appears as a nearly uniform signal in all 12 of the towers in a cable, with no corresponding signal in any of the anode layers. This noise is removed by an algorithm which searches for the characteristic 12 tower pattern.

4.2 Electron Identification

The electron identification process begins with an energy clustering algorithm. Electromagnetic clusters are then matched to tracks found in the tracking chambers, and various electron quality parameters are calculated.

4.2.1 Clustering

The electron clustering algorithm searches the η-ϕ array of calorimeter towers for "seed" towers having transverse electromagnetic energy, E_t^{EM}, greater than 3 GeV. Adjoining towers sharing a side or a corner are associated with the cluster if they have $E_t^{EM} > 0.1$ GeV. Clustering proceeds until there are no adjoining towers above threshold or until the cluster reaches a predetermined size. This size limit is based on the size of real electron showers and the physical size of the towers in each detector, and is fixed to be 3 towers in η by 1 tower in ϕ in the CEM, 5 by 5 towers in the PEM, and 7 by 7 towers in the FEM. The transverse hadronic energy in the cluster, E_t^{HAD}, is summed separately. Electromagnetic clusters are retained only if the total cluster E_t^{EM} is greater than 5 GeV and the ratio of hadronic to electromagnetic transverse energies, E_t^{HAD}/E_t^{EM}, is less than 0.125.

After clusters are formed, the electron identification algorithm loops over all the reconstructed tracks in the event and extrapolates them into the calorimeters. Tracks with extrapolated positions which lie within an electromagnetic cluster region are associated with the cluster. The associated track with the highest transverse momentum, p_t, is taken to be the electron track.

4.2.2 Electron Quality Parameters

Two electron quality parameters are defined for all the calorimeter elements and help to separate electrons from jets and other background. The ratio of hadronic to electromagnetic transverse energies, E_t^{HAD}/E_t^{EM} (abbreviated HAD/EM), is sensitive to hadronic energy associated with an electromagnetic cluster. Isolation (abbreviated I) is a measure of the energy near the electromagnetic cluster. Isolation is defined by

$$I = \frac{E_t^{Cone} - E_t^{EM}}{E_t^{Cone}}, \tag{4.1}$$

where E_t^{Cone} is the total transverse energy contained in a cone of radius $r = ((\Delta\eta)^2 + (\Delta\phi)^2)^{1/2} < 0.4$ centered on the electromagnetic cluster. A small number of jets fragment in such a way that one or more very energetic π^0's are produced along with a few low energy charged particles. The π^0's decay quickly into photons which shower in the electromagnetic portion of the calorimeter to produce an electromagnetic cluster. The electron track requirement can be satisfied by one of the low energy charged particles. Background of this type can be removed by looking for residual (hadronic) energy in or near the electron cluster.

There can be additional energy deposition near a real electron due to the "underlying event" - the low energy spray of particles inevitable in $p\bar{p}$ collisions. Analysis cuts on HAD/EM or I are never fully efficient, then, due to this underlying energy.

Various other electron quality parameters have been defined for each calorimeter, based primarily on the shape of showers from electrons from test beams. The electron finding algorithm calculates these quantities for each identified electromagnetic cluster. For the CEM, five additional parameters are used for electron selection:

- E/p, the ratio of cluster energy to the momentum of the matched CTC track.
- LSHR, a measure of the lateral distribution of energy in a cluster. The z position of the electron shower in the calorimeter as measured by the strip chamber is used in conjunction with a test beam parametrization to predict the distribution of energy among the calorimeter towers in the cluster, and the measured distribution is compared to this prediction. The quantity LSHR is defined by

$$\text{LSHR} = 0.14 * \sum_i \frac{E_i^{Adj} - E_i^{Prob}}{\sqrt{0.14^2 * E + (\Delta E_i^{Prob})^2}} \tag{4.2}$$

where E_i^{Adj} is the measured energy in a tower adjacent to the seed tower, E_i^{Prob} is the energy expected in that tower based on strip chamber information, E is the cluster energy, and ΔE_i^{Prob} is the uncertainty on E_i^{Prob} associated with a 1 cm uncertainty in the strip chamber position measurement.

- χ^2_{strip}, a measure of shower shape in the strip chamber. The energy distribution in the cathode strips is compared to a parametrization derived from electrons from a test beam.
- Δx, Δz, the difference in x and z, in centimeters, between the strip cluster and the extrapolated CTC track. The relative alignment of the CTC and the strip chambers has been measured *in situ* using a sample of 12000 electrons.

Two parameters are used for selecting plug electrons:

- $\chi^2_{3\times3}$, a measure of the transverse shape of the calorimeter cluster. The energy distribution in the calorimeter towers in a 3×3 region centered on the seed tower is compared to a parametrization derived from electrons from a test beam.
- VTPC occupancy, a loose track requirement. A "road" beginning at the collision point and pointing at the calorimeter cluster is defined. The VTPC occupancy is defined to be the number of VTPC hits detected along the road divided by the number of VTPC wires crossed by the road. If the road passes too near one of the internal VTPC structural members, the occupancy defaults to 1.0.

One parameter is used in selecting forward electrons. The ratio E_{front}/E_{total} is the ratio of cluster energy deposited in the front half of the FEM to the total cluster energy. Real electrons deposit most of their energy in the first half of the FEM.

4.3 Energy Corrections

A number of energy corrections must be made to compensate for relative tower response and variations in detector calibrations. Ultimately, all calorimeter energies are tied to or compared with an absolute momentum scale determined by the CTC.

To establish an absolute CTC momentum scale, it is necessary first to calibrate the drift velocities and TDC offsets using charged particle tracks from minimum bias events, as described in Section 3.2.1 and then to correct for errors in the CTC wire positions. Errors in the azimuthal alignment of the CTC wires are studied using a sample of 17000 inclusive electrons. By equalizing the mean of the E/p distribution for the positrons and electrons in the inclusive sample, azimuthal offsets are determined for each of the 84 wire layers in the CTC. This E/p alignment correction is checked using cosmic rays. To the track reconstruction algorithms, cosmic rays which traverse the CTC and pass near the beam axis appear as two oppositely charged tracks originating from a vertex near the beam. If the CTC wires are aligned correctly, the two tracks reconstructed from a cosmic ray should have the same curvature and should have the same reconstructed vertex.

The CTC momentum scale is determined by the magnetic field. The absolute magnetic field has been mapped to ±0.05%, and so the CTC momentum scale is well known *a priori*. The momentum scale is checked using a sample of $J/\psi \rightarrow \mu^+\mu^-$ and $\upsilon \rightarrow \mu^+\mu^-$ events. The measured J/ψ mass agrees with published values within its 0.03% statistical uncertainty, and the υ is $0.1\% \pm 0.1\%$ high.

Three energy corrections are applied to the CEM data. First, the CEM calorimeter response to electrons varies across the face of a calorimeter tower. This response has been measured in a test beam, as described in Section 3.2.2, and is found to vary by approximately 6% across the tower face. The position of an electron within the tower is determined from strip chamber information, and a position dependent correction is applied. Second, the CEM response varies on a tower by tower basis. Using a sample of 17000 inclusive electrons, the

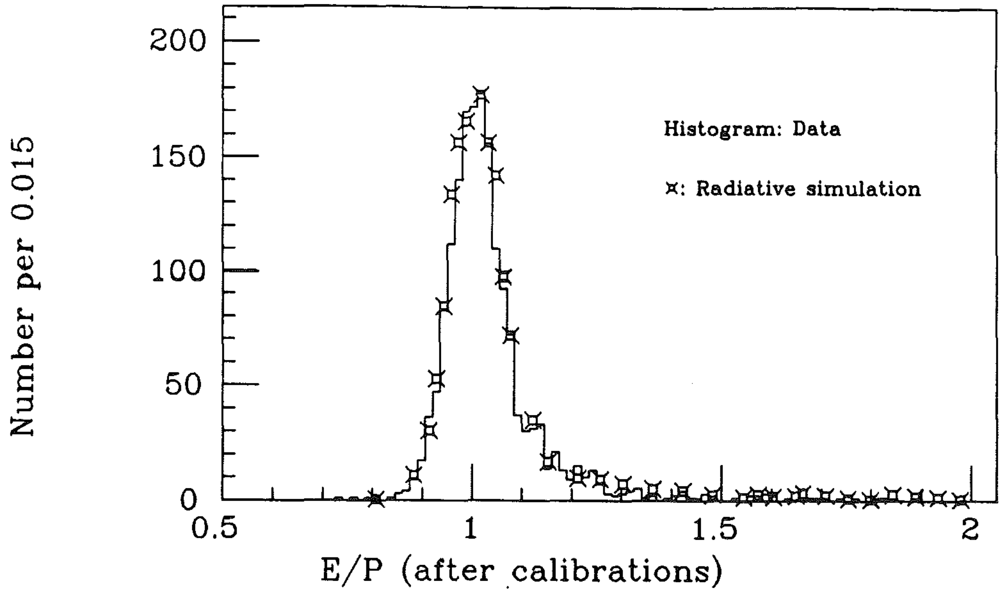

Figure 4.1: The E/p distribution from a radiative Monte Carlo compared to the E/p distribution from 1800 W± → $e\nu$ events after energy corrections are made to the W data.

relative tower responses are measured by measuring the average of the E/p distribution on a tower by tower basis. Typical tower to tower corrections are of order 3%. Third, an overall correction factor determined from 1800 W± → $e\nu$ events is used to tie the CEM energy scale to the absolute scale determined from CTC momentum measurements. A Monte Carlo simulation which includes radiative effects is used to predict the shape of the E/p distribution. Matching the mean of the E/p distribution from 1800 measured W± → $e\nu$ events to the Monte Carlo prediction indicates that the CEM energy scale must be scaled up by 1.7%. The E/p distributions from the radiative Monte Carlo and from the data after corrections are shown in Figure 4.1. Using these corrections, CDF has used 65 Z^0 events in which both electrons are found in the CEM to measure the Z^0 mass to be 91.1 ± 0.5 GeV/c^2 [23], in good agreement with the SLC result of 91.14 ± 0.12 GeV/c^2 [24] and the average LEP result 91.161 ± 0.031 GeV/c^2 [25].

There are three energy corrections which are applied to the PEM data, in addition to the dead layer correction discussed in Section 4.3. First, the PEM calorimeter response varies on a tower by tower basis. The tower to tower variations in each quadrant have been measured using electrons from a test beam, and a correction factor is applied. Typical tower to tower variations are of the order 6%. Second, the PEM calorimeter response is nonlinear for high energy electrons. This nonlinearity has been measured using test beam electrons, and is found to be approximately 7% at 200 GeV. Third, quadrant to quadrant variations are measured using Z^0 events in which one decay electron is contained in the CEM. Quadrant correction factors are found by constraining the average Z^0 mass found in each quadrant to the average mass value from a quadrant whose response is well measured in test beam studies. After these corrections, the Z^0 mass found using CEM–PEM events is 90.7 ± 1.9 GeV/c^2, in good agreement with the published CEM-only Z^0 mass.

The FEM response is nonlinear for very high energy electrons, and a nonlinearity correction must be applied in addition to the dead layer correction. The FEM response has been measured with test beam electrons up to 200 GeV. Due to longitudinal boosts, however, the energies of electrons from Z^0 decay can range up to 400 GeV in the FEM. The test beam results are extrapolated by measuring the average Z^0 mass as a function of FEM electron energy using Z^0's in which one electron is contained in the CEM. By constraining the CEM–FEM masses to the CEM–CEM Z^0 mass, the energy nonlinearity is determined, and the FEM energy scale is tied to the CEM scale. The nonlinearity correction increases the cluster energy by approximately 10% for 200 GeV electrons. FEM quadrant to quadrant variations are measured using the energy spectrum of the neutron induced energy spikes. These neutron data are in good agreement with the quadrant to quadrant variations seen in Z^0 events.

4.4 Event Selection

Event processing and selection proceeds in several distinct steps. First, all events are processed with the so-called "production" code: calorimeter ADC data are converted to energies, full track reconstruction is performed, [1] and the electron identification algorithm (as well as jet, muon, and other physics algorithms) is applied. Events having one or more identified electromagnetic clusters are written to an initial set of summary tapes. Next, this initial set of summary tapes is processed by a simple program which applies loose electron energy and quality cuts to find candidate $W^{\pm}$ and Z^0 events; the Z^0 events are used in the asymmetry analysis, while the $W^{\pm}$ events are used to measure various efficiencies. The Z^0 candidates are required to have two electromagnetic clusters with transverse energies greater than 10 GeV, and the $W^{\pm}$ candidates must have one CEM electron with transverse energy greater than 10 GeV, and missing transverse energy ($\not{E}_t$, an indirect signature for neutrinos which have large transverse momentum and escape the detector without interacting) greater than 20 GeV. The $W^{\pm}$ and Z^0 candidate events are written to a second set of summary tapes. The final event selection is made using this second set of $W^{\pm}$ and Z^0 summary tapes. Energy corrections as discussed above are applied, and energy-dependent quality parameters are recalculated. More restrictive electron quality cuts and transverse energy thresholds are applied to the corrected data, along with fiducial volume restrictions, an event vertex cut, and a trigger requirement to produce samples of well-measured W's and Z^0's. These cuts and requirements are described below.

4.4.1 Electron Quality Requirements

The angle $\hat{\theta}$ is defined to be the angle between the incoming quark (or antiquark) and the outgoing electron (or positron). This definition is charge dependent, and so the charge of

---

[1] The track reconstruction used in the "production" processing does not include the azimuthal correction factors discussed in Section 4.3. Some charge dependent differences are therefore expected in the final event sample.

E_t	$>$	15	GeV
E/p	$<$	1.5	
LSHR	$<$	.20	
χ^2_{strip}	$<$	15	
$\lvert\Delta x\rvert$	$<$	1.5	cm
$\lvert\Delta z\rvert$	$<$	3.0	cm
Iso(r=.4)	$<$	.10	

Table 4.1: Tight CEM electron quality cuts.

CEM:	E_t	$>$	15	GeV
	E/p	$<$	1.5	
	Iso(r=.4)	$<$	.10	
PEM:	E_t	$>$	15	GeV
	$\chi^2_{3\times3}$	$<$	20	
	VTPC occupancy	$>$	0.5	
	HAD/EM	$<$	.05	
	Iso(r=.4)	$<$	.10	
FEM:	E_t	$>$	15	GeV
	E_{front}/E_{total}	$>$	.6	
	HAD/EM	$<$	.05	
	Iso(r=.4)	$<$	.10	

Table 4.2: Electron quality requirements for the second electron in a Z^0 event.

at least one of the electrons from the Z^0 decay must be measured. For the asymmetry measurement, then, at least one of the electrons must be produced in the central region and leave a well reconstructed track in the CTC. Each event is required to have at least one electron in the CEM with transverse energy greater than 15 GeV and which passes the cuts listed in Table 4.1. A second electromagnetic cluster with transverse energy greater than 15 GeV is required. The second cluster can be contained in any calorimeter, and must pass the looser quality cuts shown in Table 4.2. Figures 4.2 through 4.4 show the distributions of the various quality parameters for electrons in the Z^0 data sample. For each of the parameters, the electron is required to pass all of the quality requirements except for

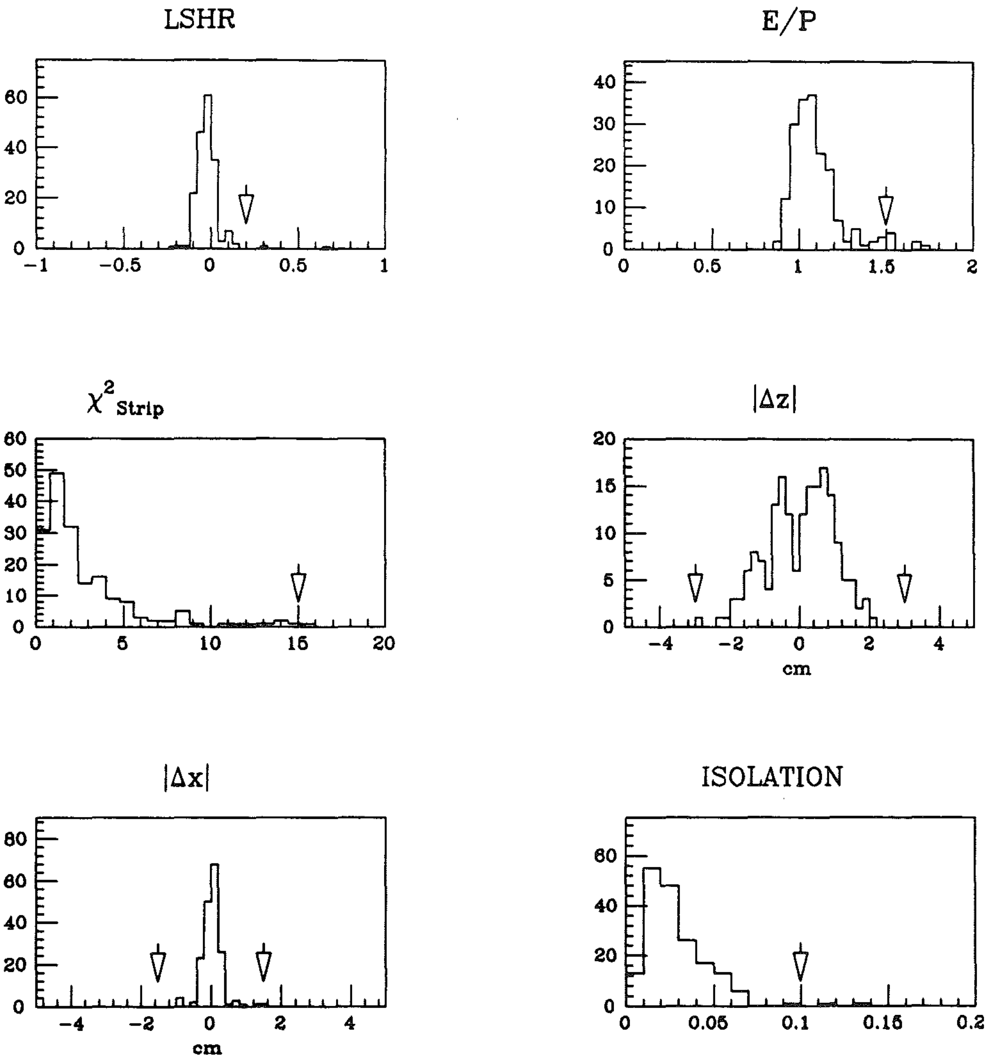

Figure 4.2: Electron quality parameters for electrons in the CEM. Arrows indicate the value of the quality requirement.

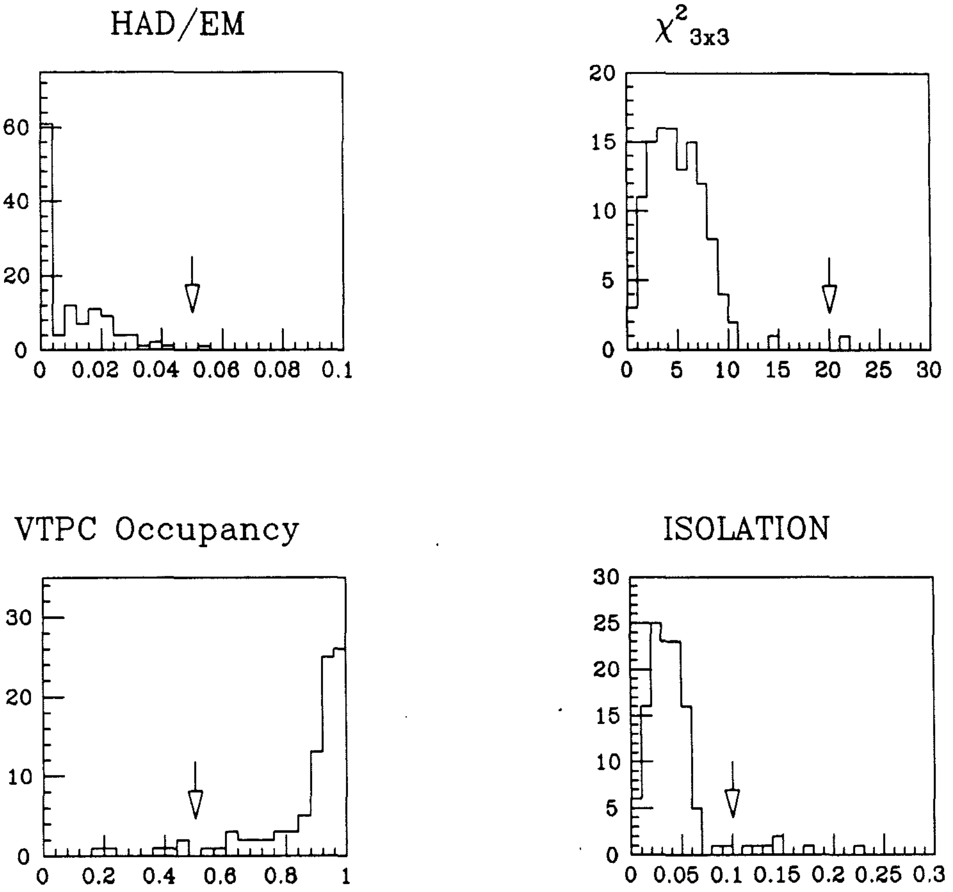

Figure 4.3: Electron quality parameters for electrons in the PEM. Arrows indicate the value of the quality requirement.

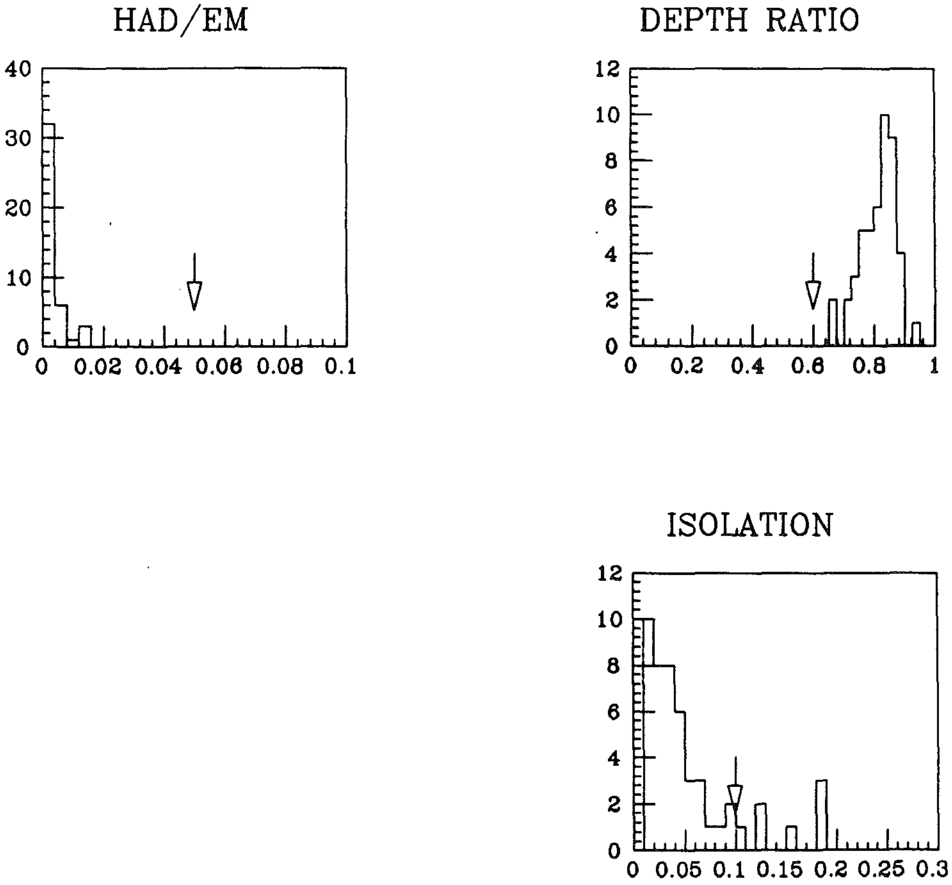

HAD/EM

DEPTH RATIO

ISOLATION

Figure 4.4: Electron quality parameters for electrons in the FEM. Arrows indicate the value of the quality requirement.

the parameter being plotted. Arrows indicate the cut values.

4.4.2 Fiducial Requirements

In addition to the electron quality cuts, the electrons in the W and Z^0 samples are restricted to a fiducial detector volume in which the calorimeter response is well understood and energies are reliably measured. For the most part, this simply means avoiding cracks and dead spaces between calorimeter modules, although some dead PEM towers are explicitly removed. Electrons in the CEM are restricted in the following ways:

- Dead spaces between adjacent wedges are excluded by requiring that the extrapolated track position be within 21 cm in ϕ from the tower center. This requires electrons to be more than 3 cm from the 15° wedge boundaries.
- The crack at $\theta = 90^\circ$ between the two halves of the central calorimeter barrel is excluded. The extrapolated track position is required to have $|z| > 9$ cm.
- The cluster seed tower must not be the outermost tower in the central wedge. The projective geometry for this tower is somewhat extreme; a large amount of radiator and scintillator is removed, as discussed in Section 3.2.2, and large energy corrections are required.
- A cryogenic and electrical feedthrough for the superconducting solenoid penetrates one of the central calorimeter wedges. This wedge has seven normal towers, one highly modified tower, and two missing towers. Electrons are excluded from the missing and modified towers in this wedge.

Electromagnetic clusters in the PEM are restricted from border regions and dead calorimeter towers as follows:

- The seed tower must not be in any of the towers adjacent to the ϕ boundary between quadrants.

- The seed tower must not be in the two outermost or two innermost η annuli. This excludes the cracks between the CEM and PEM and between the PEM and FEM.
- The seed tower is excluded from 16 dead PEM towers. Of these 16 towers, 13 are in regions already excluded by the quadrant boundaries.

Electromagnetic clusters in the FEM are restricted from quadrant borders and from regions with partial hadronic coverage as follows:

- The seed tower must not be in any of the towers adjacent to the ϕ boundary between quadrants.
- The seed tower is must not be in the 5 innermost η annuli. This excludes a region in which there is only partial hadronic coverage; the low beta quadrupoles penetrate the FHA, as discussed in Section 3.2.2, and hadronic coverage is limited in this region.

A plot of the allowed η-ϕ regions is shown in Figure 4.5. The fiducial cuts reduce the detector acceptance by approximately 29%.

4.4.3 Vertex Requirement

The proton and antiproton bunches circulating in the accelerator have finite lengths, and so collisions can occur at some distance from the nominal interaction point. The position of the collision, as determined by the vertex of VTPC tracks, is Gaussian distributed about the nominal position with a sigma of 30 cm. The projective tower geometry is distorted for events with large vertex displacement. Furthermore, the detector's hermiticity is compromised; particles from displaced vertices can escape without detection through the crack between the plug and forward calorimeters. To preserve the detector geometry, events are required to have vertex positions within ±60 cm of the nominal interaction point.

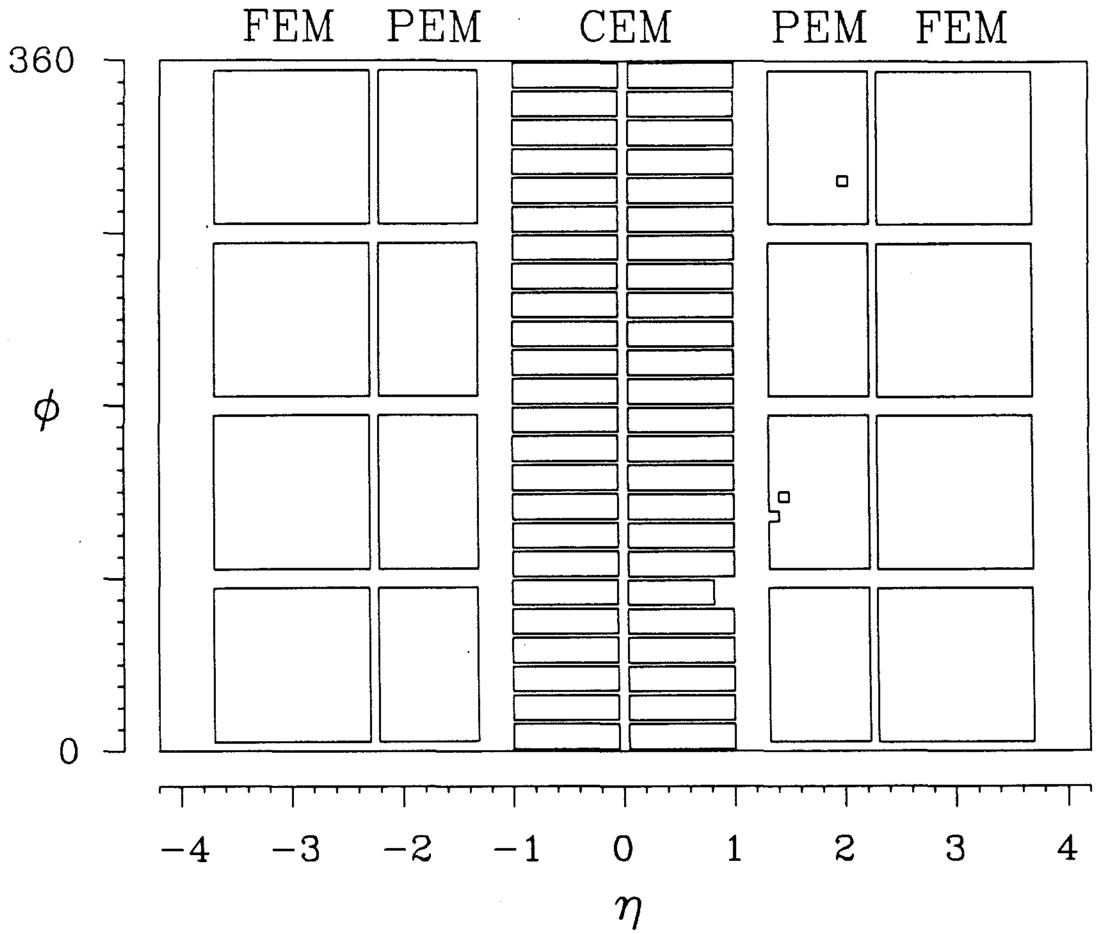

Figure 4.5: Calorimeter fiducial region for electrons. Three dead towers in the PEM and the cryogenic solenoid feedthrough at 90° are indicated

4.4.4 Electron Trigger Requirement

There are a number of different triggers which will accept Z^0 events, and a single event may satisfy more than one set of trigger requirements. In order to understand the trigger efficiency and potential trigger biases, the data are required to satisfy a single trigger. With all events satisfying one set of trigger requirements, only one trigger efficiency and bias estimate need be calculated.

All the events are required to satisfy the so–called ELECTRON_12 trigger. This is a Level 2 based trigger, and requires:

- an electromagnetic cluster in the CEM with transverse energy greater than 12 GeV,
- the ratio of hadronic to electromagnetic transverse energy $HAD/EM < 12.5\%$,
- a track from the fast track processor matched in ϕ to the calorimeter cluster, and having transverse momentum $p_t > 6$ GeV.

This trigger requires a valid Level 0 trigger from the BBC and a Level 1 trigger requiring at least one CEM trigger tower with E_t greater than 6 GeV as prerequisites.

Much of the data was collected with no Level 3 electron trigger requirement. During the latter part of the run a Level 3 algorithm was introduced which required the Level 2 ELECTRON_12 trigger as a prerequisite. This Level 3 algorithm calculates the LSHR variable and uses a more sophisticated tracking algorithm to harden the 6 GeV p_t threshold. For the asymmetry analysis, the final analysis cuts are more restrictive than those imposed by the Level 3 algorithm, and so the fundamental trigger efficiency is determined by the Level 2 trigger.

The efficiency of the ELECTRON_12 trigger is measured using events which pass a similar prescaled 7 GeV trigger. The efficiency of the ELECTRON_12 trigger as a function of E_t is shown in Figure 4.6. The trigger becomes fully efficient before 15 GeV, and the trigger efficiency for electrons passing the tight CEM cuts and having transverse energies

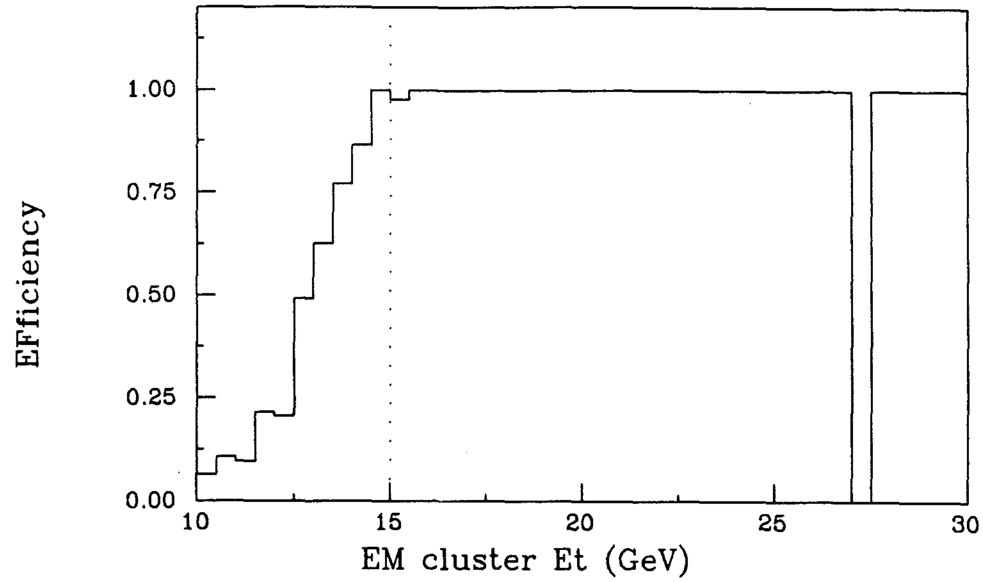

Figure 4.6: The efficiency of the ELECTRON_12 trigger as a function of electron cluster transverse energy.

greater than 15 GeV is measured to be 97.3 ± 0.5%.

4.4.5 The Final Z^0 Sample and the Angular Distribution

Applying the dielectron cuts to a data sample corresponding to an integrated luminosity of 4.4 pb^{-1} produces a sample of 302 events. A 4-vector is defined for each of the electrons in this sample. The direction of the electron 4-vector is determined by the position of the z vertex and the direction of the electron track in the CTC for CEM electrons, and by the vertex and the plug strip cluster or the energy weighted cluster centroid for PEM and FEM electrons. In all cases, the energy component of the 4-vector is taken to be the corrected calorimeter cluster energy. The invariant mass distribution of the 302 dielectron events is shown in Figure 4.7. There is a prominent Z^0 peak on a Drell-Yan continuum. (The efficiency for low mass Drell-Yan pairs falls due to the electron E_t requirement.) Backgrounds appear to be low. The Z^0 sample is taken to be the 252 events with 75 <

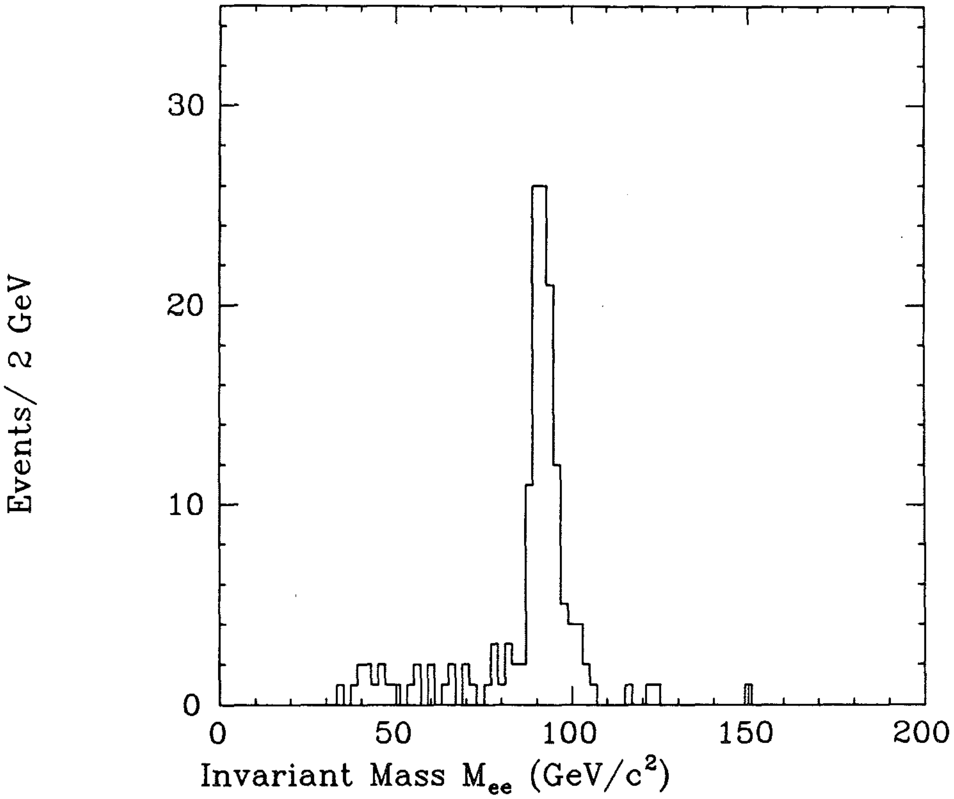

Figure 4.7: Invariant mass distribution of dielectron events satisfying the electron quality requirements.

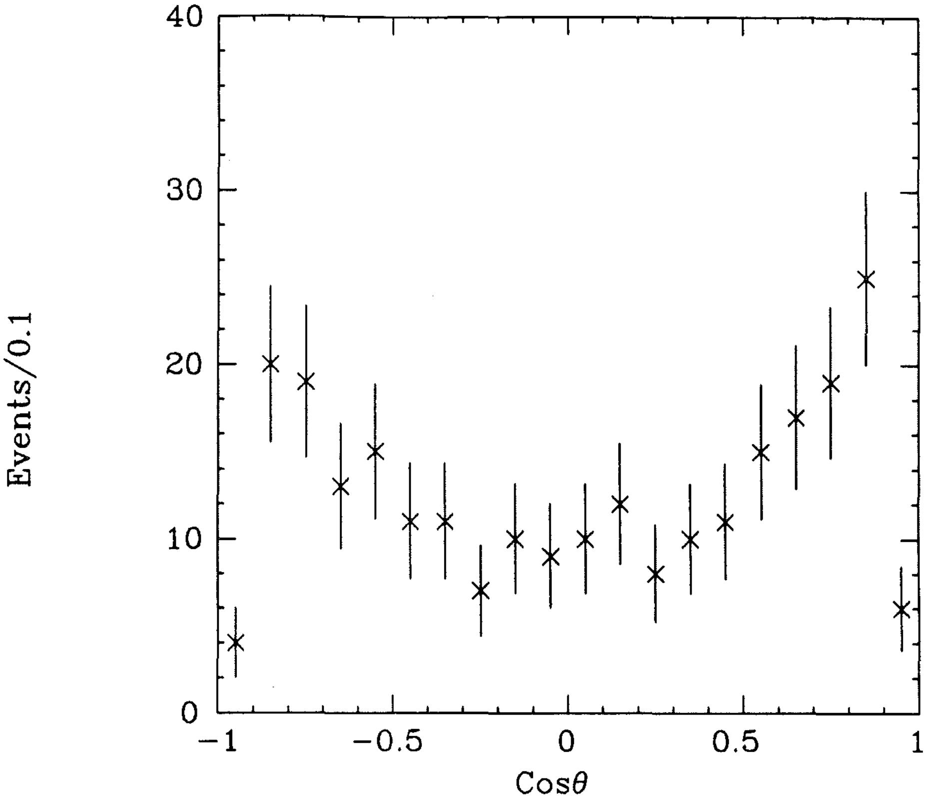

Figure 4.8: The uncorrected $\cos\hat{\theta}$ distribution for the 252 events in the invariant mass region $75 < M_{ee} < 105$ GeV.

$M_{ee} < 105$ GeV. A log likelihood fit of the mass values to a simple Breit–Wigner form yields a Z^0 mass of 91.05 ± 0.23 GeV, in good agreement with the published CDF Z^0 mass of 91.1 ± 0.5 GeV/c^2 [23].

The angle $\hat{\theta}$ is calculated using the Collins–Soper method, as discussed in Section 2.2 and defined in Equation 2.30. The angular distribution $dN/d\cos\hat{\theta}$ of the 252 Z^0 events is shown in Figure 4.8. The angular distribution has the parabolic shape predicted by the differential cross section of Equation 2.29, and there are more events with positive values of $\cos\hat{\theta}$, as expected. The electron E_t cut reduces the acceptance for events with large values of $|\cos\hat{\theta}|$, and so there are a reduced number of events in the outermost bins of Figure 4.8. Additional acceptance issues are discussed below.

4.5 Electron Selection Efficiency

The efficiencies for the electron quality cuts and isolation requirement are determined directly from the W and Z^0 data [26]. The efficiency of a particular quality requirement is determined from a Z^0 data sample in which all quality requirements except the one in question are made. Data samples selected in this way contain good electrons with little background, and are unbiased with respect to the quality parameter in question. The efficiency of a quality cut is defined to be

$$\epsilon \equiv \frac{N(pass)}{N(unbiased\ sample)} \tag{4.3}$$

where $N(pass)$ is the number of electrons which satisfy the quality requirement in question, and $N(unbiased\ sample)$ is the number of electrons in an unbiased data sample as discussed above. Isolation is always required for both electrons, and the isolation efficiency is determined in a separate calculation. The total electron efficiency, then, is given by the product of the isolation efficiency and the measured efficiency for isolated electrons. Electron efficiencies (excluding isolation efficiency) determined from the Z^0 data are given in Table 4.3 [26]. The efficiency of the tight combination of CEM cuts is slightly larger than the product of the efficiencies of the individual cuts. This is because the E/p and $|\Delta x|$ cut are slightly correlated.

Efficiencies for the tight and loose CEM cuts are also determined from the W data[26]. The W's are selected by requiring each event to have one isolated CEM electron which satisfies the fiducial volume cuts, and has E_t greater than 25 GeV and a track with p_t greater than 7.5 GeV pointing at the cluster. No further electron quality requirements are made, and this data sample is unbiased with respect to all of the quality parameters except isolation. The W events are further required to have $\not{E}_t$ greater than 20 GeV, and $\not{E}_t$

Quality Parameter		ϵ from Z^0 data	ϵ from W data
CEM:	E/p	0.912 ± 0.020	0.916 ± 0.005
	LSHR	0.985 ± 0.008	0.975 ± 0.003
	χ^2_{Strip}	0.976 ± 0.011	0.974 ± 0.003
	$\lvert\Delta z\rvert$	0.985 ± 0.008	0.979 ± 0.003
	$\lvert\Delta x\rvert$	0.963 ± 0.013	0.966 ± 0.004
	All tight CEM cuts	0.873 ± 0.023	0.877 ± 0.007
	All loose CEM cuts	0.912 ± 0.020	0.916 ± 0.005
PEM:	Had/EM	0.992 ± 0.008	-
	$\chi^2_{3\times 3}$	0.992 ± 0.008	-
	VTPC Occupancy	0.958 ± 0.019	-
	All PEM cuts	0.941 ± 0.022	-
FEM:	Had/EM	1.000 ± 0.005	-
	E_{front}/E_{total}	0.977 ± 0.023	-
	All cuts	0.977 ± 0.024	-

Table 4.3: Efficiencies for individual electron quality parameters determined from the W and Z^0 data samples.

significance greater than 2.5, where the significance is defined to be

$$\sigma_{\not{E}_t} = \frac{\not{E}_t}{\sqrt{\sum_i E_t}}, \tag{4.4}$$

where the sum represents the scalar sum of the transverse energy in all the calorimeter towers. The significance cut helps to reject dijet events in which a mismeasurement of one of the jets contributes a large $\not{E}_t$. To remove residual background from dijet events in which one jet is poorly measured, the W events are required to have no jet with E_t greater than 10 GeV opposite in azimuth (*i.e.* within ±30° of the direction opposite in azimuth) of the electron cluster. The efficiencies of the electron quality cuts (excluding isolation efficiency) determined from the W data are also given in Table 4.3 [26]. The efficiencies determined from the W and Z^0 data samples agree well.

The isolation efficiency depends on the amount of underlying event energy contained in the r = 0.4 isolation cone, as discussed in Section 4.2.2. The isolation efficiency is calculated by artificially moving the electron clusters from Z^0 decays to different regions in the detector, and recalculating the isolation parameter at each new position [26]. Moving

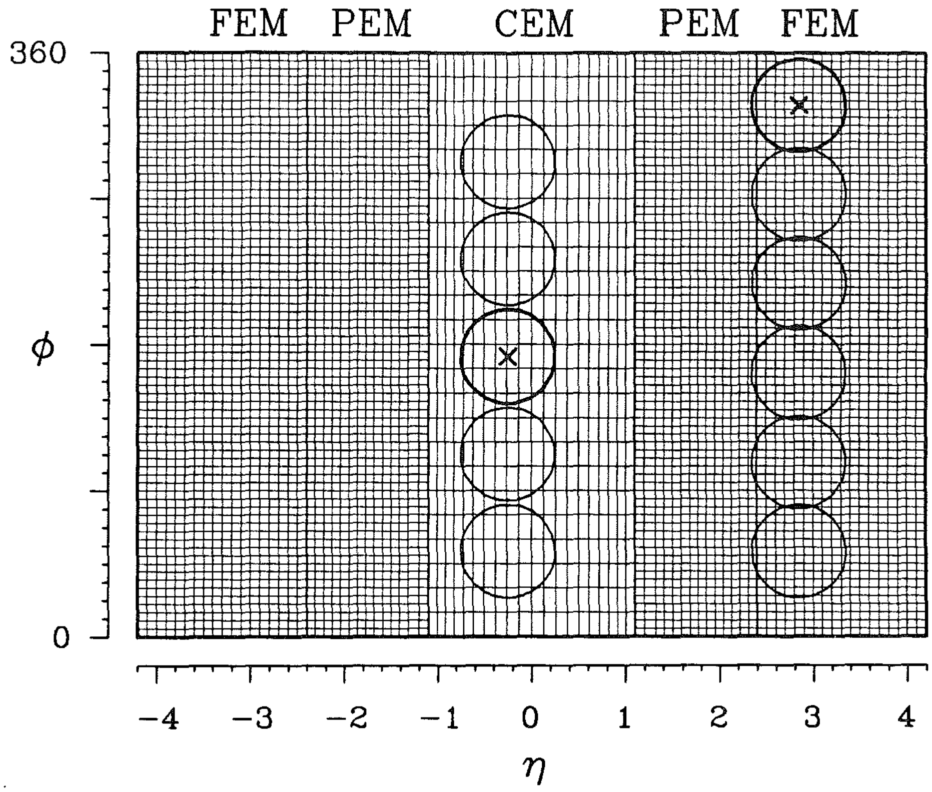

Figure 4.9: Isolation cones used in the calculation of the isolation efficiency. The circles indicate the cones of radius 0.4, and the ×'s sho the location of the electrons in the original Z^0 event.

the electron positions in this way samples different parts of the underlying event, and allows one to measure the effect of underlying event fluctuations on the isolation parameter. In practice, the size of an electron shower in η-ϕ space varies with η, and so the cluster η should remain fixed when varying the position. Furthermore, for events in which both electrons are deposited in the CEM, care must be taken when changing electron positions so that the two electron clusters never overlap. Figure 4.9 shows an η-ϕ plot of a typical Z^0 event, along with the new isolation cones used in the efficiency calculation. The isolation efficiencies

Electron	Isolation Efficiency
CEM	0.985 ± 0.003
PEM	0.976 ± 0.007
FEM	0.977 ± 0.011

Table 4.4: Electron isolation efficiencies.

determined for each detector are given in Table 4.4 [26].

The isolation efficiency for CEM electrons has been checked using the W and Z data [26]. By requiring the electrons to pass all the quality cuts except isolation, one can calculate the isolation efficiency in the same manner used to calculate the efficiency of the quality cuts. The isolation efficiency measured using the W data is 0.977 ± 0.003 [26], and is 0.977 ± 0.011 [26] from the Z^0 sample, in agreement with the CEM value in Table 4.4.

4.6 $\cos\hat{\theta}$ Acceptance

A Monte Carlo event generator and a simple detector simulation are used to determine the acceptance of the CDF detector and analysis cuts as a function of $\cos\hat{\theta}$. The detector geometry and electron E_t cut are easily simulated. The electron quality and isolation cuts are simulated simply by accepting and rejecting events based on the measured efficiency of the cuts. This is much faster than a full simulation of each detector component. The efficiencies used are the product of the electron quality and isolation efficiencies given in Tables 4.3 and 4.4, and are taken to be

$$
\begin{aligned}
\epsilon_{\mathrm{CEM(tight)}} &= 0.860 \pm 0.023 \\
\epsilon_{\mathrm{CEM(loose)}} &= 0.898 \pm 0.020 \\
\epsilon_{\mathrm{PEM}} &= 0.918 \pm 0.023 \\
\epsilon_{\mathrm{FEM}} &= 0.954 \pm 0.026
\end{aligned}
$$

The ISAJET Monte Carlo (version 6.22) [27] is used as the event generator for the acceptance calculation. The EHLQ 1 [16] parametrization is used to describe the quark momentum distribution functions. The steps in the acceptance calculation are as follows:

1. Generate $p\bar{p} \rightarrow e^{+}e^{-}$ events
2. Make histogram of $d\mathrm{N}/d\cos\hat{\theta}$ using generated quantities for events with 75 GeV $<$ $M_{ee} <$ 105 GeV
3. Smear the event vertex with $\sigma_{\mathrm{vertex}} = 30.0$ cm
4. Extrapolate the electron 4-vectors to the detector.
5. Make fiducial cuts on the extrapolated position consistent with those made on the data.
6. Smear the electron energy by the calorimeter resolutions:

$$\begin{array}{lrcll} \mathrm{CEM} & (\sigma_E/E)^2 & = & (0.135/\sqrt{E\sin\theta})^2 & + \; (0.017)^2 \\ \mathrm{PEM} & \sigma_E/E & = & 0.28/\sqrt{E} & + \; .02 \\ \mathrm{FEM} & \sigma_E/E & = & 0.25/\sqrt{E} & + \; .005 \end{array}$$

7. Make the E_t cut on each electron (15 GeV).
8. Discard electrons in each detector based on the combined efficiencies for the electron quality cuts given above
9. Make histogram of $d\mathrm{N}/d\cos\hat{\theta}$ using smeared quantities for events passing the above acceptance cuts and having 75 GeV $< M_{ee} <$ 105 GeV
10. The $\cos\hat{\theta}$ dependent acceptance is defined to be the bin–by–bin ratio of the histogram of step 9 and the histogram of step 2

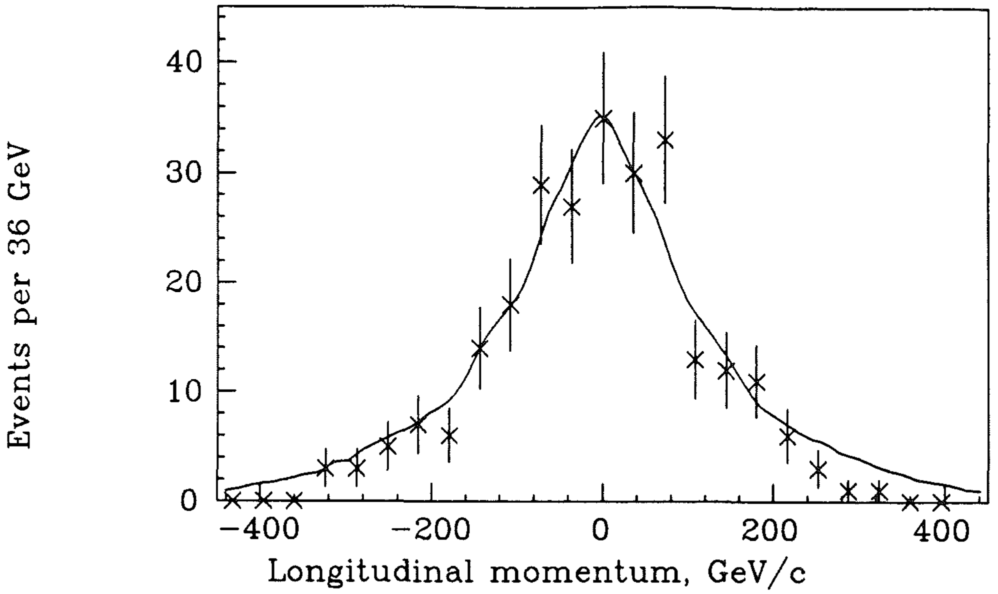

Figure 4.10: Longitudinal momentum of Z^0's. The points show the CDF data and the line shows the ISAJET Monte Carlo prediction.

Figures 4.10 through 4.12 show comparisons between kinematic quantities generated by the Monte Carlo calculations and the real data. The longitudinal and transverse momenta of the Z^0 are shown in Figures 4.10 and 4.11, respectively. There is good agreement between the data and the Monte Carlo for these two kinematic quantities, implying that the Monte Carlo generates events with the proper kinematics. Figure 4.12 shows the detector occupancy for electrons as a function of calorimeter η band. The gaps are due to the fiducial cuts between calorimeter elements. The Monte Carlo and data agree well, implying that the simple simulation correctly reproduces the detector geometry, the vertex smearing, and the relative detector efficiencies.

A plot of acceptance versus $\cos\hat{\theta}$ is shown in Figure 4.13. Histogram bins have been combined in a symmetric fashion in order to increase the statistical accuracy of the acceptance measurement; potential asymmetries in the detector acceptance are discussed in Section 5.2.4. The size of the statistical error bars is small compared to the size of the

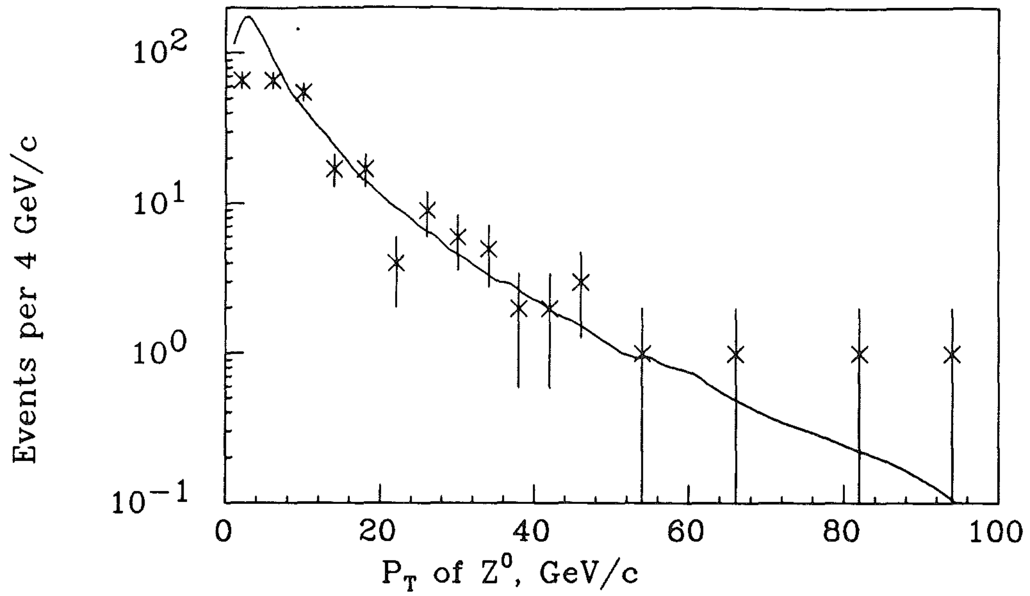

Figure 4.11: Transverse momentum of Z^0's. The points show the CDF data and the line shows the ISAJET Monte Carlo prediction.

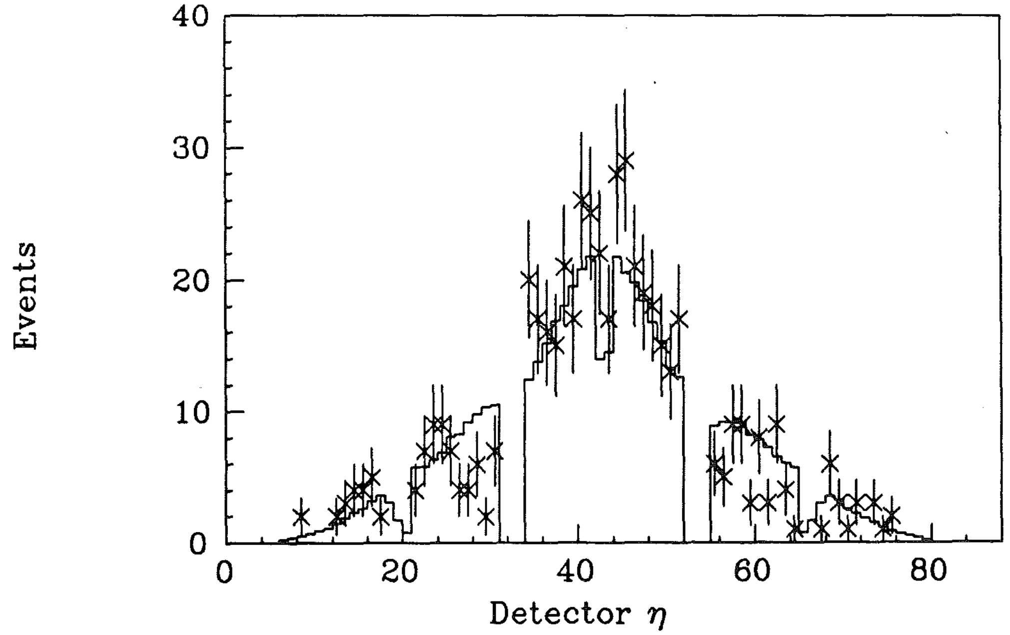

Figure 4.12: Calorimeter η band occupancy. The points show the CDF data and the histogram shows the ISAJET Monte Carlo prediction.

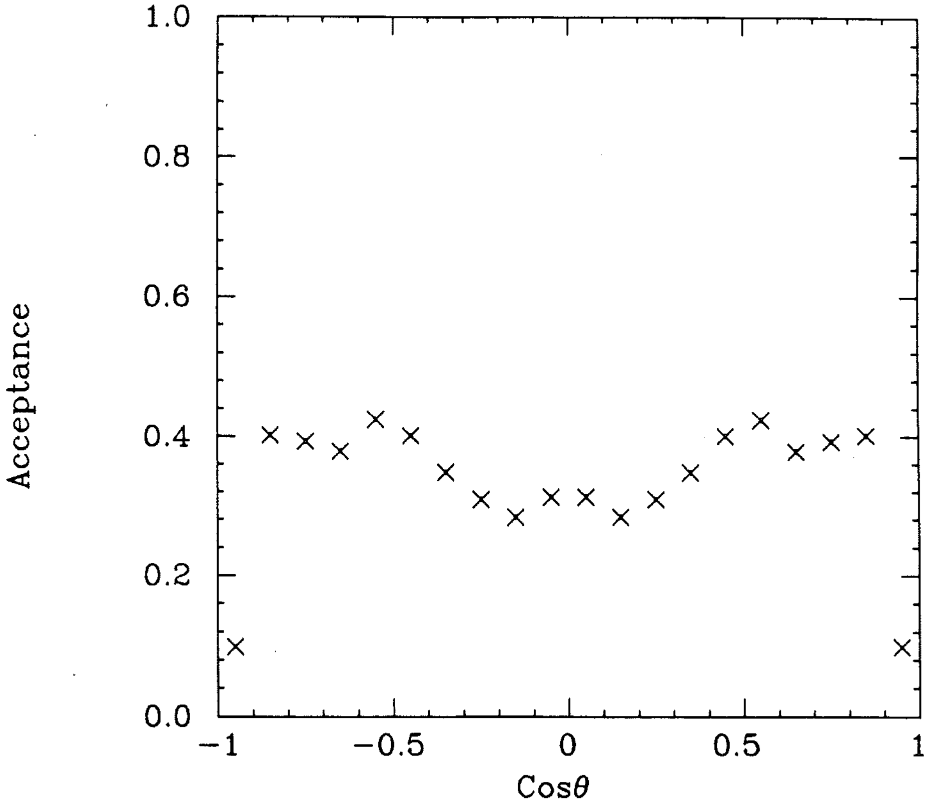

Figure 4.13: The acceptance of the CDF detector and the analysis cuts as a function of $\cos\hat{\theta}$.

plotting symbol. The acceptance for small values of $|\cos\hat{\theta}|$ is reduced by kinematics and the requirement that one electron be located in the CEM. Events with small $|\cos\hat{\theta}|$ values are produced with $\hat{\theta} \simeq 90°$; longitudinal motion of the Z^0 often boosts both the decay electrons in events of this type out of the central region and into the gas calorimeters. The acceptance is significantly reduced for $|\cos\hat{\theta}| > 0.9$ for two reasons. First, the E_t's of the electrons in events with large values of $\cos\hat{\theta}$ tend to peak at low values, due to simple kinematics ($E_t \sim E\sin\hat{\theta}$), and a large number of these events are lost due to the E_t cut. Second, there is an upper limit on $\cos\hat{\theta}$ defined by the geometric extent of the FEM and CEM calorimeters and the requirement that one of the electron clusters be located in the CEM. The angular distribution is corrected bin–by–bin for acceptance to produce the plot of $1/\sigma\ d\sigma/d\cos\hat{\theta}$ shown in Figure 4.14.

4.7 Background Estimates

There are four sources of background events in the Z^0 data sample which are considered;

- real electrons from semileptonic decays of heavy quarks,
- the tail of hadronic jet fragmentation which produces high energy π^0's as leading particles, as discussed in Section 4.2.2,
- $W \to e\nu$ + jet events in which the jet produces an electromagnetic cluster,
- real electrons from decays of τ's in $Z^0 \to \tau^+\tau^- \to e^+\nu_e\bar{\nu}_\tau e^-\bar{\nu}_e\nu_\tau$ events.

The first two sources are lumped together and investigated using isolation. The second two are investigated using Monte Carlo techniques.

4.7.1 QCD Background

The QCD background is estimated from three studies of the invariant mass spectrum and an isolation parameter called I_{max}, where I_{max} is defined to be the larger of the isolation values

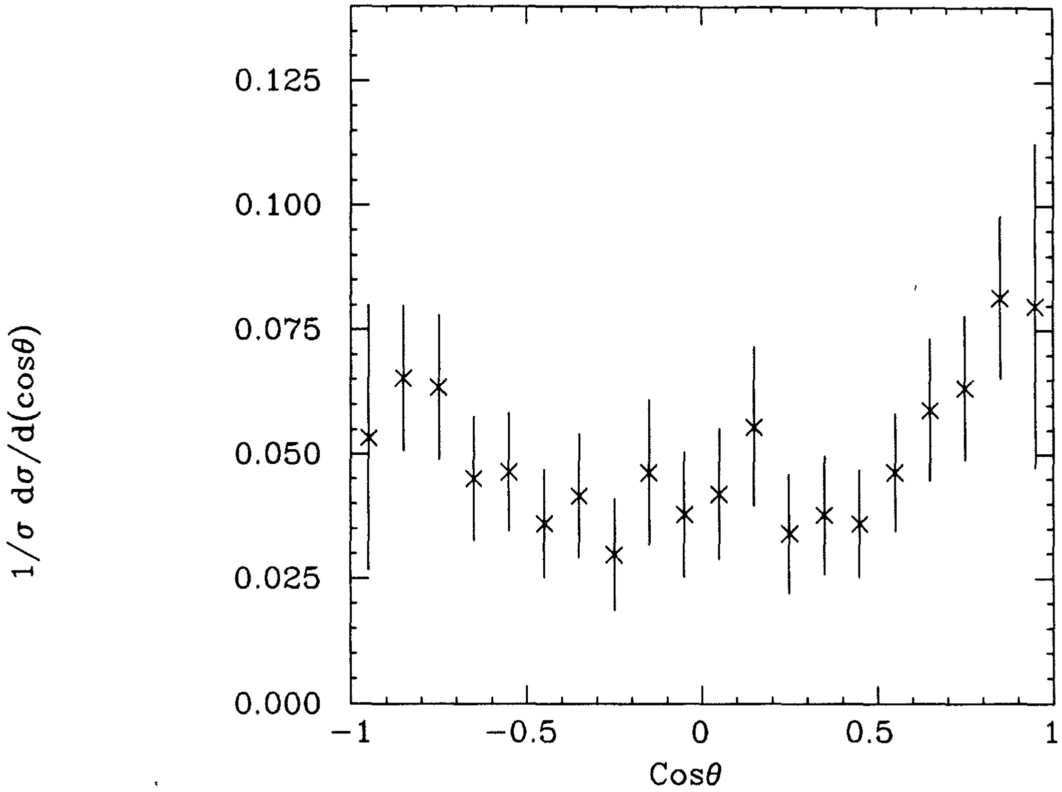

Figure 4.14: The $\cos\hat{\theta}$ distribution after acceptance corrections.

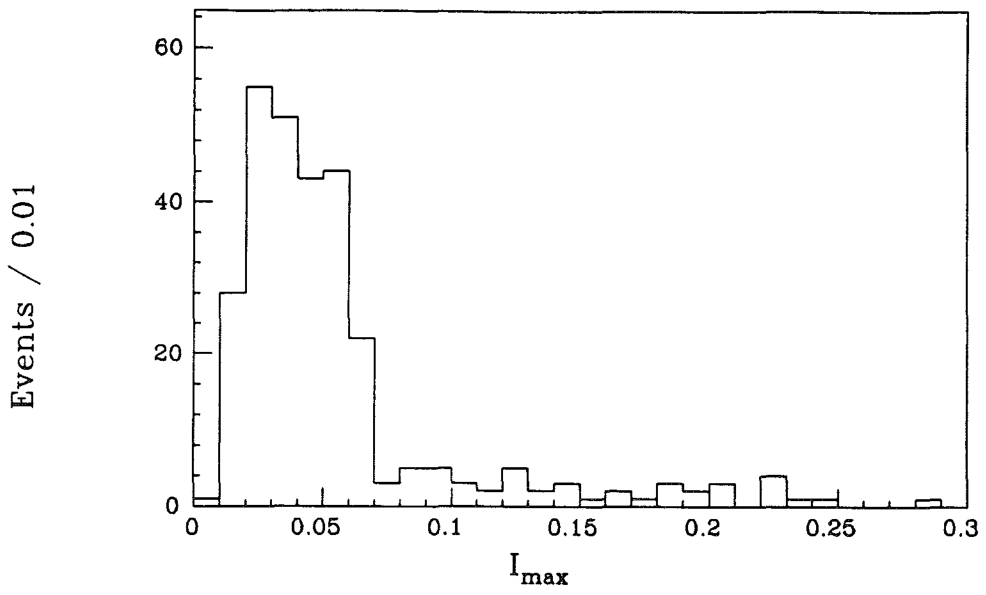

Figure 4.15: Maximium isolation I_{max} for dielectron events in the mass region between 75 and 105 GeV/c^2.

for the two electromagnetic clusters in the event. A plot of I_{max} for events with two electrons passing all the electron quality cuts except isolation and having invariant masses between 75 and 105 GeV/c^2 is shown in Figure 4.15. The I_{max} distribution shown in Figure 4.15 peaks at a somewhat higher value than the distributions of isolation shown in Figures 4.2 through 4.4. The QCD background is assumed to be flat in I_{max} above $I_{max} = 0.1$, and then to fall linearly with I_{max} in the region $0 < I_{max} < 0.1$, going to 0 at $I_{max} = 0$. This is approximately consistent with the behavior of I_{max} for identified photon conversions and π^0's in the data, and with the behavior of $b\bar{b}$ events generated with the ISAJET Monte Carlo, as shown in Figure 4.16. The QCD background is expected to be a steeply falling function of the invariant mass. For the purposes of the background estimation, the QCD background is assumed to fall linearly with invariant mass in the region of the Z^0, going to 0 at 120 GeV.

A plot of I_{max} versus invariant mass for events with two electrons passing all the electron

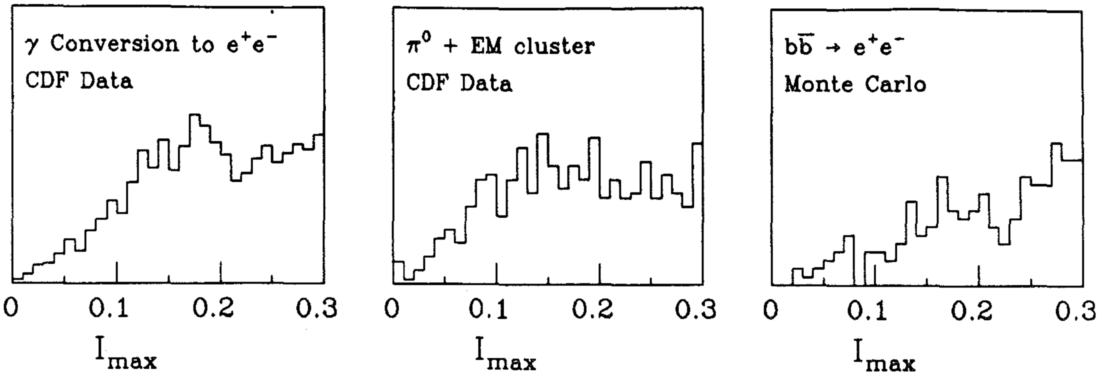

Figure 4.16: Distributions of maximum isolation, I_{max}, for identified photon conversions and π^0's from the CDF data and $b\bar{b}$ Monte Carlo events.

quality cuts except isolation is shown in Figure 4.17. (This plot is made without the ELECTRON_12 trigger requirement.) Three background estimates are made using the events in the regions marked $a \cdots e$ and Z. The region marked Z contains 257 events assumed to be Z^0's with a small amount of background. Regions d and e contain 14 and 3 events, respectively, which are assumed to be Drell–Yan events with background. Region b contains 24 events, and is assumed to be mostly background with a few real Z^0 events with I_{max} values which have fluctuated up. Regions a and c contain 10 and 4 events respectively, and are assumed to be pure background; there are too few Drell–Yan events in these mass regions to contribute through I_{max} fluctuations.

In the first of the three background estimation methods, the known isolation efficiency is used to estimate the number of real Z^0 fluctuations in region b. Assuming an average isolation efficiency of 0.98, the probability of one of the two electrons from a Z^0 decay having $I_{max} > 0.1$ is given by $P = 1.0 - (0.98)^2 = 0.04$. Assuming, for the moment, that the 257 events in the Z region are all good Z^0's, this implies that there are 10.6 good Z^0 events in the b region, and therefore 13.4 background events in region b. One can now use the

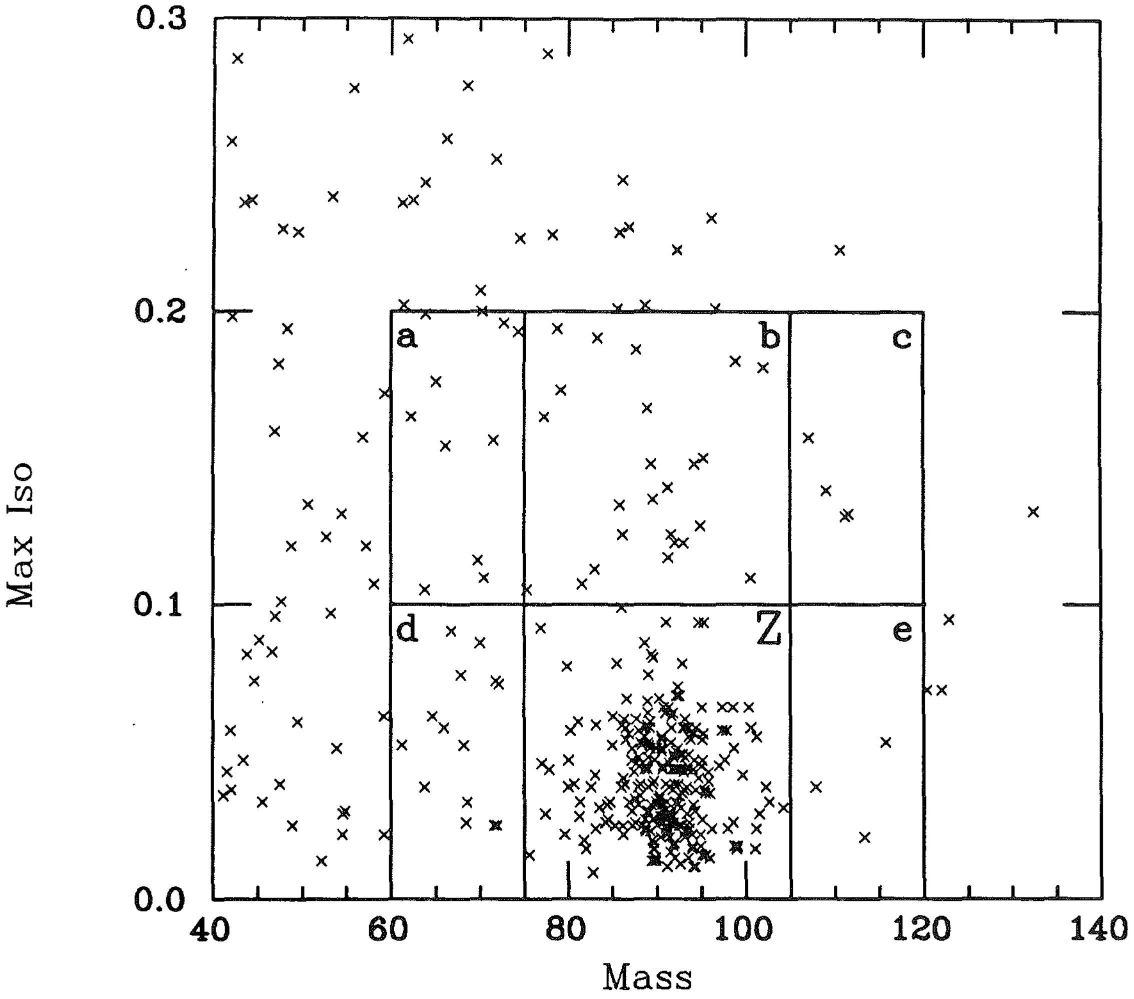

Figure 4.17: Maximum isolation, I_{max}, versus invariant mass for events with two electromagnetic clusters.

assumed behavior of the background in I_{max} to extrapolate the 13.4 background events in the b region back into the Z region. This extrapolation predicts 7 background events in the Z^0 sample.

In the second method, the background is assumed to fall linearly with invariant mass, and the 14 background events in in regions a and c are extrapolated to predict 14 background events in the b region. These 14 background events in region b are, in turn, extrapolated into the Z region using the assumed behavior of I_{max} to predict 7 background events in the Z^0 sample.

In the third method, the invariant mass spectrum for Drell–Yan plus Z^0 events is normalized to the number of events in the Z region, and then used to predict 6.5 and 4.3 Drell–Yan events in regions d and e, respectively. This implies that the remaining 6 events in regions d and e are background. These 6 background events are extrapolated using the linearly falling invariant mass spectrum to predict 6 background events in the Z^0 sample.

The three QCD background estimates agree well with one another. The background in the Z^0 sample due to QCD sources is taken to be 7 ± 3 events.

4.7.2 $W \rightarrow e\nu$ + jet Background

The background due to $W \rightarrow e\nu$ + jet where the jet fakes a second electron is interesting because the distribution of electrons from the W decay is itself asymmetric, and may have a significant effect on the observed Z^0 asymmetry. The background due to W + jet production is estimated using a combination of data studies and Monte Carlo simulation. The relative rates of Z^0 and W + jet production are measured from the data, as is the probability of a jet fragmenting to produce an electromagnetic energy cluster, while the kinematics are studied with a Monte Carlo.

The ratio of the W and Z^0 cross sections, $R = \sigma \cdot B(W \rightarrow e\nu)/\sigma \cdot B(Z \rightarrow e^+e^-)$, is measured to be 10.2 [28]. Using this ratio and the measured number of Z^0 events in the data sample, one estimates that there are approximately 2570 $W \rightarrow e\nu$ events in which the electron from the W decay would pass the CEM electron cuts listed in Table 4.1. Of these W events, 26.6% are produced with a jet having transverse energy greater than 15 GeV [29].

The probability of a jet faking an electron in the central detector is small due to the E/p requirement, and is estimated to be approximately 1/2000 [30]. The background from W + jet events in which the jet is in the central region of the detector is therefore expected to be negligible, and only events with jets located in the gas calorimeters are considered. The properties of jets in the gas calorimeters have been measured using a dijet sample in which one of the jets is required to be in the central region of the detector [31]. An upper limit on the number of jets which would pass the electron quality requirements can be estimated from the ratio of hadronic to electromagnetic transverse energies, HAD/EM, for jets in the gas calorimeters. It is estimated that 0.5% of the jets in the PEM would pass the 0.05 HAD/EM cut shown in Table 4.2, and that 2.2% of the jets in the FEM would pass the HAD/EM cut.

The PAPAGENO [32] Monte Carlo is used to produce W + jet events with the proper decay kinematics. The event vertex is smeared, and the electron and jet 4-vectors are extrapolated into the detector. Both the electron and the jet are required to have transverse energies greater than 15 GeV. The electron from the W decay is required to be in the central region, and the jet is required to be in one of the gas calorimeters; no requirement is made on the neutrino from the W decay. An "invariant mass" is constructed using the electron and jet 4-vectors; the invariant mass calculated in this way is required to be in the range 75 GeV $< M_{e-jet} <$ 105 GeV. Finally, the event is weighted by the probability that the jet would pass the HAD/EM quality cut. Of the events in which both electron and the jet have transverse energies greater than 15 GeV, fewer than 0.53% pass the kinematic and HAD/EM cuts. After combining the calculation of the total W event rate with the Monte Carlo results, it is estimated that there are fewer than 0.4 events in the Z^0 sample from W + jet events in which the jet fakes a second electron.

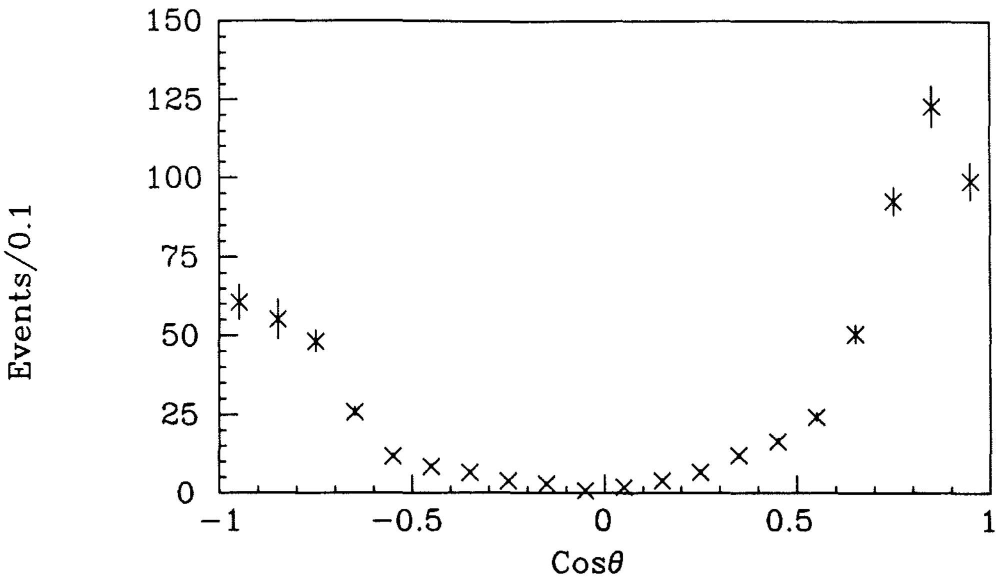

Figure 4.18: Angular distribution of W + jet events in which the jet fakes a second electron.

Although the angular distribution of electrons from W decays are very asymmetric, as shown in Section 2.1, the W in the event is not reconstructed properly; the electron and the jet are assumed to be the outgoing electrons from a Z^0 decay, and the resulting angular distribution is distorted. The $\cos\hat{\theta}$ distribution for events of this type is shown in Figure 4.18, where $\cos\hat{\theta}$ is calculated from Equation 2.30 using the electron and jet 4-vectors. There is a residual asymmetry of 36% due to the asymmetry in the electron distribution from the decay of the W.

4.7.3 $Z^0 \rightarrow \tau^+\tau^-$ Background

The background due to $Z^0 \rightarrow \tau^+\tau^-$ events in which both τ's decay to electrons is estimated using the ISAJET Monte Carlo. $Z^0 \rightarrow \tau^+\tau^- \rightarrow e^+\nu_e\bar{\nu}_\tau e^-\bar{\nu}_e\nu_\tau$ events are generated with ISAJET, and fiducial and electron E_t cuts are applied. The generated events are scaled to the 1988-1989 integrated luminosity, assuming $\sigma \cdot B(Z^0 \rightarrow \tau^+\tau^-) = 200\text{nb}$ and a $\tau \rightarrow$

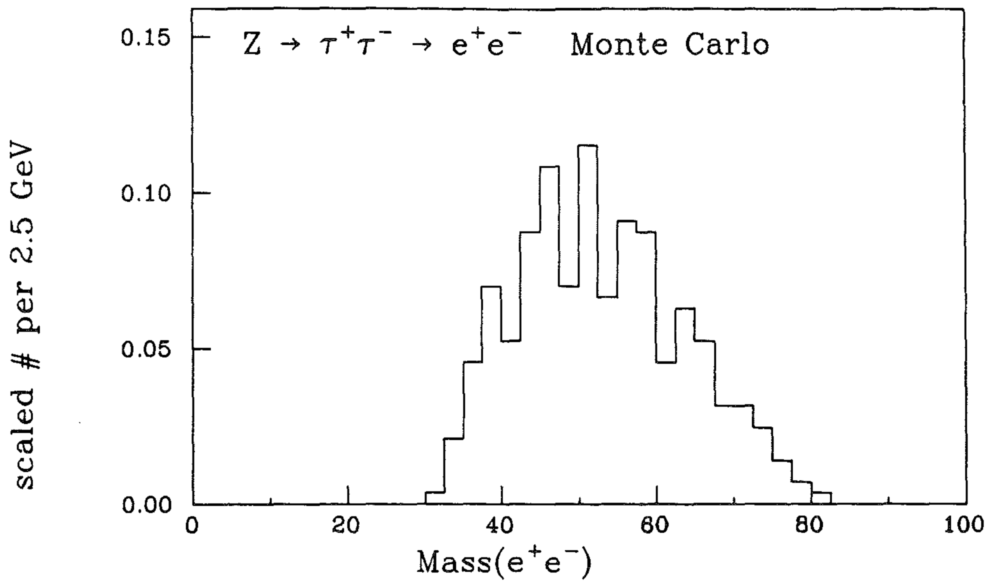

Figure 4.19: Invariant mass distribution of $Z^0 \rightarrow \tau^+\tau^- \rightarrow e^+\nu_e\bar{\nu}_\tau e^-\bar{\nu}_e\nu_\tau$ Monte Carlo events, after scaling to the integrated luminosity for the 1988-1989 run.

$e\nu_e\nu_\tau$ branching fraction of 0.18. The invariant mass spectrum of dielectrons is shown in Figure 4.19 after the luminosity scaling. One event passes the fiducial and E_t cuts, and 0.02 events are contained in the region $75 < M_{ee} < 105$ GeV. The $Z^0 \rightarrow \tau^+\tau^-$ background in the $Z^0 \rightarrow e^+e^-$ sample is negligible.

Chapter 5

Data Analysis

There are several different ways of extracting the forward–backward asymmetry from the angular distribution. This chapter discusses the methods used to measure both A_{FB} and $\sin^2\theta_W$, and presents an analysis of the systematic uncertainties on the measurement.

5.1 Determining A_{FB} and $\sin^2\theta_W$

Three methods are used to determine $\sin^2\theta_W$ and A_{FB} from the angular distribution; two different fits to a functional form, and a direct technique. Values for $\sin^2\theta_W$ are determined from the two fitting methods by fitting the data to the full lowest order cross section of Equation 2.29, and extracting $\sin^2\theta_W$ directly. Values for the asymmetry are determined by fitting to a simpler parabolic form,

$$\frac{d\hat{\sigma}}{d\cos\hat{\theta}} = (1+\cos^2\hat{\theta}) + \beta\cos\hat{\theta}; \tag{5.1}$$

the forward–backward asymmetry is given by

$$A_{\mathrm{FB}} = \frac{3}{8}\beta. \tag{5.2}$$

The MINUIT [33] function minimization package is used to minimize either a log–likelihood or a chi–square function for the fits. In the direct method, A_{FB} is measured directly from the acceptance corrected $1/\sigma \; d\sigma/d\cos\hat{\theta}$ distribution of Figure 4.14 using the definition of Equation 2.16. A value for $\sin^2\theta_W$ is then determined from this asymmetry value. Each of these three methods is described below, paying particular attention to acceptance effects.

To simplify equations presented below, the lowest order cross section of Equation 2.29 is represented by the simple form

$$\frac{d\hat{\sigma}}{d\cos\hat{\theta}} = A(1+\cos^2\hat{\theta}) + B\cos\hat{\theta} \tag{5.3}$$

where A and B are functions of $\sin^2\theta_W$ and include integrations over structure functions and kinematic variables. (The forward–backward asymmetry is given by $A_{\mathrm{FB}} = \frac{3}{8}\frac{B}{A}$.) It is also convenient to describe the detector acceptance by a function $\epsilon(\cos^2\hat{\theta})$, which is explicitly symmetric in $\cos\hat{\theta}$.

5.1.1 Negative log likelihood fit

The method of choice for measuring $\sin^2\theta_W$ is an unbinned, event by event negative log likelihood fit to the $d\mathrm{N}/d\cos\hat{\theta}$ distribution of Figure 4.8. A disadvantage of any log likelihood fit is that the value of the likelihood is not readily converted into a measure of the goodness of the fit. For the asymmetry analysis, however, a log likelihood fit has the advantage that the estimation of $\sin^2\theta_W$ and A_{FB} is independent of the acceptance if the acceptance is symmetric in $\cos\hat{\theta}$.

The log likelihood fit begins with a normalized probability distribution function derived from the simplified cross section of Equation 5.3:

$$P(\sin^2\theta_W, \cos\hat{\theta}) = \frac{3}{8}\left((1+\cos^2\hat{\theta}) + B/A\cos\hat{\theta}\right). \tag{5.4}$$

After the normalization, all the information about the forward–backward asymmetry and $\sin^2\theta_W$ is contained in the B/A term. The acceptance is incorporated into the analysis by defining a new normalized acceptance-corrected probability function P' which includes the acceptance function $\epsilon(\cos^2\hat{\theta})$:

$$P'(\sin^2\theta_W, \cos\hat{\theta}) = \frac{3}{8}N\epsilon(\cos^2\hat{\theta})\left((1+\cos^2\hat{\theta}) + B/A\cos\hat{\theta}\right), \tag{5.5}$$

where N is a normalization factor given by

$$\begin{aligned} N^{-1} &= \frac{3}{8}\int_{-1}^{1}\epsilon(\cos^2\hat{\theta})(1+\cos^2\hat{\theta})d\cos\hat{\theta}+\frac{3}{8}\int_{-1}^{1}\epsilon(\cos^2\hat{\theta})A/B\cos\hat{\theta}d\cos\hat{\theta} \\ &= \frac{3}{8}\int_{-1}^{1}\epsilon(\cos^2\hat{\theta})(1+\cos^2\hat{\theta})d\cos\hat{\theta}+\quad 0. \end{aligned} \tag{5.6}$$

The normalization factor N is determined by the components of the probability distribution P' which are even with respect to $\cos\hat{\theta}$; the odd components integrate to zero. N is independent of both $\sin^2\theta_W$ and the asymmetry. The acceptance–corrected probability distribution P' now describes the angular distribution measured with the CDF detector and electron quality cuts described in Section 4.4.1.

The likelihood, $\mathcal{L}$, and the negative log likelihood for a given data sample are defined by

$$\mathcal{L} = \prod_i N\epsilon_i(\cos^2\hat{\theta})P_i(\sin^2\theta_W,\cos\hat{\theta}) \tag{5.7}$$

$$-\ln\mathcal{L} = -\sum_i \ln(N\epsilon_i(\cos^2\hat{\theta})) - \sum_i \ln P_i(\sin^2\theta_W,\cos\hat{\theta}) \tag{5.8}$$

where P_i and ϵ_i are the probability and acceptance weight for the ith data event. The best estimate of $\sin^2\theta_W$ (or A_{FB}) for a given data sample is the value of $\sin^2\theta_W$ which maximizes the likelihood $\mathcal{L}$ or minimizes $-\ln\mathcal{L}$ for the sample. For a given data sample, the term $\sum_i \ln(N\epsilon_i(\cos^2\hat{\theta}))$ is a constant, independent of $\sin^2\theta_W$, and does not affect the minimization of $-\ln\mathcal{L}$ and the estimation of $\sin^2\theta_W$ or A_{FB}. For the negative log likelihood fit, then, the parameter estimation is independent of the acceptance if the acceptance is symmetric in $\cos\hat{\theta}$.

Plots of $-\ln\mathcal{L}$ versus β from Equation 5.1 and versus $\sin^2\theta_W$ for the uncorrected angular distribution of Figure 4.8 are shown in Figures 5.1 and 5.2, respectively. The log likelihood functions are smooth, and have minima at $\beta = 0.1333$ (which implies an asymmetry $A_{\mathrm{FB}} = 5.00\%$) and at $\sin^2\theta_W = 0.2314$ (using EHLQ 1 distribution functions). The 68.3% (1σ) confidence intervals for the fitted values of β or A_{FB} and $\sin^2\theta_W$ can be estimated from the $-\ln\mathcal{L}$ functions [34]. The 68.3% confidence interval corresponds to an

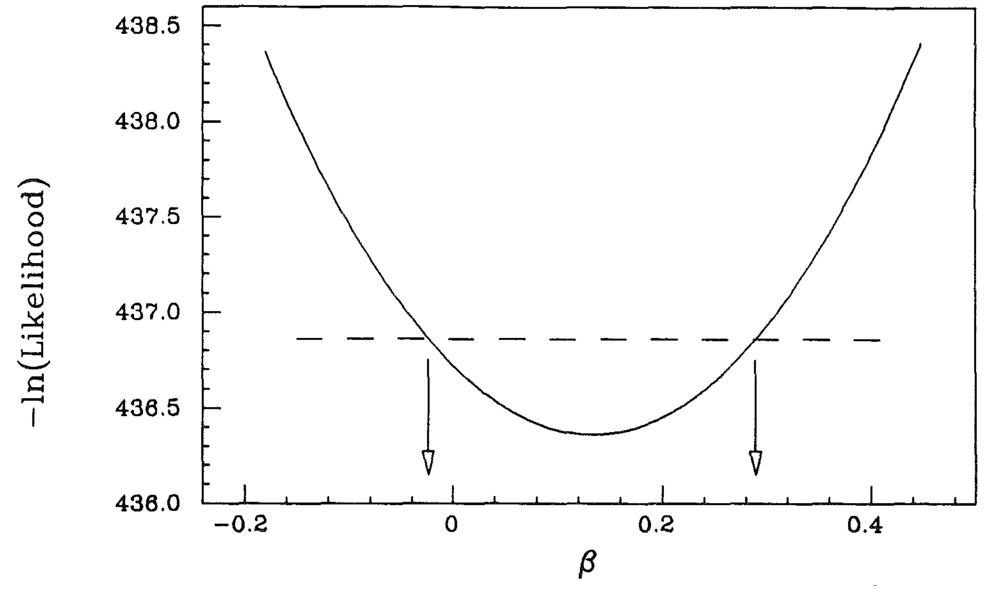

Figure 5.1: Negative log likelihood, $-\ln\mathcal{L}$, versus β. The 68.3% confidence interval is indicated by the arrows.

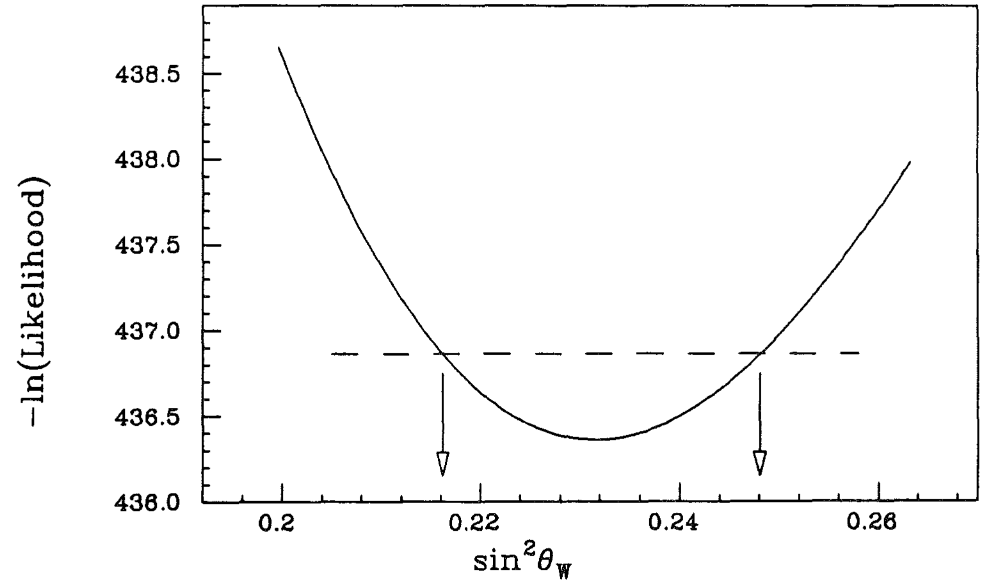

Figure 5.2: Negative log likelihood, $-\ln\mathcal{L}$, versus $\sin^2\theta_W$. The 68.3% confidence interval is indicated by the arrows.

increase of $\frac{1}{2}$ in the value of $-\ln\mathcal{L}$ above the minimum value. This increase is shown by the dashed lines in Figures 5.1 and 5.2, and the confidence intervals are indicated by the arrows. The $-\ln\mathcal{L}$ function for the β parameter is nearly symmetric about its minimum, and the confidence interval is also symmetric about the estimated value of β. The forward–backward asymmetry is determined from the $-\ln\mathcal{L}$ fit to be $A_{\mathrm{FB}} = (5.0 \pm 5.9\ (\mathrm{stat}))\%$. The $-\ln\mathcal{L}$ function for $\sin^2\theta_W$ is somewhat asymmetric about its minimum, and so the confidence interval is not symmetric about the estimated $\sin^2\theta_W$ value. The $-\ln\mathcal{L}$ fit of the angular distribution of Figure 4.8 to the lowest order cross section of Equation 2.29 gives $\sin^2\theta_W = 0.231^{+0.017}_{-0.015}$. While the forward–backward asymmetry and $\sin^2\theta_W$ are directly related, as shown in Figure 2.5, this relationship is not strictly linear. Due to the curvature of the asymmetry function in the region near $\sin^2\theta_W = 0.23$, a confidence interval symmetric about a fitted value of A_{FB} is not symmetric about the $\sin^2\theta_W$ value corresponding to the fitted value of A_{FB}.

5.1.2 Binned χ^2 fit

The second method for measuring $\sin^2\theta_W$ is a binned χ^2 fit to the acceptance corrected $(1/\sigma)d\sigma/d\cos\hat{\theta}$ distribution of Figure 4.14. In this fit, the χ^2 statistic is defined by

$$\chi^2 = \sum_i \frac{(y_i - y(x_i))^2}{\sigma_i^2}, \tag{5.9}$$

where y_i is the number of entries in the ith bin of the $(1/\sigma)d\sigma/d\cos\hat{\theta}$ distribution, $y(x_i)$ is the number of entries in the bin centered at x_i predicted by the angular distribution, and σ_i is the statistical uncertainty on the number of entries in the ith bin. The best estimate of $\sin^2\theta_W$ (or A_{FB}) is the value of $\sin^2\theta_W$ which minimizes the χ^2 statistic. An advantage of the χ^2 method is that the value of the χ^2 statistic gives some insight into the quality of the fit. This method, however, depends explicitly on the acceptance measured in Section 4.6, and is also sensitive to the relative normalizations of the predicted and measured angular distributions.

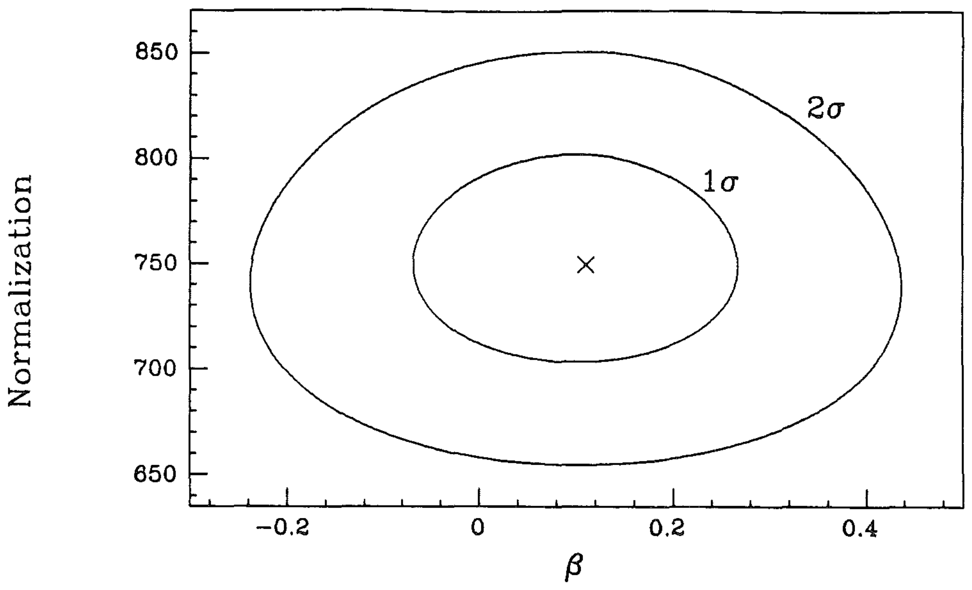

Figure 5.3: Contour plot of χ^2 as a function of β and a normalization factor. The location of the minimum and the 68.3% and 99.4% confidence contours are indicated.

To ensure that the measured angular distribution is suitably normalized, a normalization factor is allowed to vary along with $\sin^2\theta_W$ in the χ^2 fits. Furthermore, the acceptance corrections to the contents of the outermost bins of the angular distribution are relatively large, and so small fluctuations in the contents of these bins can have a large effect on the distribution after the corrections are applied. The two outermost bins are therefore excluded from the χ^2 fits.

A contour plot of χ^2 as a function of β from Equation 5.1 and a normalization factor is shown in Figure 5.3. Figure 5.4 shows a contour plot of χ^2 as a function of $\sin^2\theta_W$ and a normalization constant. The χ^2 contours are smooth, and have minima at $\beta = 0.1097$, implying $A_{\mathrm{FB}} = 4.11\%$, and at $\sin^2\theta_W = 0.2338$ (assuming EHLQ 1 distribution functions). The χ^2 value at each minimum is 5.6, which, for 16 degrees of freedom, implies a confidence level for the fits of 99.7%. As with the $\ln\mathcal{L}$ fits, confidence regions can be estimated from the χ^2 function. The 68.3% (1σ) and 95.4% (2σ) confidence regions, corresponding to

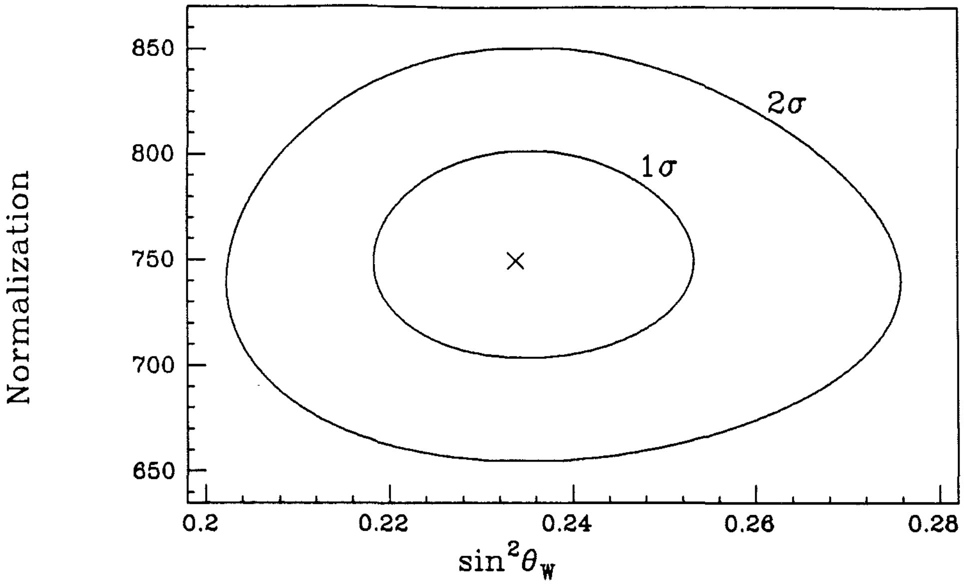

Figure 5.4: Contour plot of χ^2 as a function of $\sin^2\theta_W$ and a normalization factor. The location of the minimum and the 68.3% and 99.4% confidence contours are indicated.

increases of 1 and 4, respectively, in the value of χ^2 above the minimum value, are shown in Figures 5.3 and 5.4. The 1σ confidence region is approximately symmetric in β about the estimated value, and gives $A_{\mathrm{FB}} = (4.1 \pm 6.2\ (\mathrm{stat}))\%$. As in the $\ln\mathcal{L}$ case, the 1σ confidence region is asymmetric in $\sin^2\theta_W$, and gives $\sin^2\theta_W = 0.234^{+0.018}_{-0.016}$. Note that the semi-axes of the elliptical contours of constant χ^2 are aligned with the axes corresponding to the normalization constant and to β or $\sin^2\theta_W$. This implies that the normalization constant is uncorrelated with β or $\sin^2\theta_W$, and that the estimated values of β and $\sin^2\theta_W$ are independent of the estimated normalization factor.

5.1.3 Direct Measurement of A_{FB}

The third method is direct measurement of A_{FB} based on the definition of Equation 2.16:

$$A_{\mathrm{FB}} \;=\; \frac{\displaystyle\int_0^1 \frac{d\sigma}{d\cos\theta}\, d(\cos\theta) - \int_{-1}^0 \frac{d\sigma}{d\cos\theta}\, d(\cos\theta)}{\displaystyle\int_{-1}^1 \frac{d\sigma}{d\cos\theta}\, d(\cos\theta)}.$$

This method of determining the asymmetry is acceptance dependent, and the measurement is made using the acceptance corrected $(1/\sigma)d\sigma/d\cos\hat{\theta}$ distribution of Figure 4.14. The integrated cross sections are determined simply by summing the contents of the bins in the forward and backward regions of the $(1/\sigma)d\sigma/d\cos\hat{\theta}$ distribution. As with the binned χ^2 method, the bins nearest $|\cos\hat{\theta}| = 1.0$ are excluded and the measurement is corrected for this restricted $|\cos\hat{\theta}|$ range. After corrections, the direct method gives the result $A_{\mathrm{FB}} = (5.4 \pm 6.8 \text{ (stat)})\%$. The value of $\sin^2\theta_W$ is determined by comparing the acceptance–corrected measured value of A_{FB} with the values predicted by the lowest order cross section with EHLQ 1 distribution functions to give $\sin^2\theta_W = 0.230^{+0.019}_{-0.018}$ (stat).

5.1.4 Background Subtraction and Summary

There are an estimated 7 ± 3 background events in the Z^0 sample, which are assumed to have an angular distribution symmetric in $\cos\hat{\theta}$. If the background in the data sample is small and symmetric in $\cos\hat{\theta}$, the observed asymmetry is described by the simple relation

$$A_{\mathrm{FB}}|_{observed} = A_{\mathrm{FB}}|_{true} \cdot (1 - x), \tag{5.10}$$

where x is the fraction of background events in the sample. Using this relation and the estimate of 7 non-dielectron background events from Section 4.7, the results are corrected for background by increasing the observed forward–backward asymmetry by a relative 2.8% and by decreasing the $\sin^2\theta_W$ values by approximately 0.0004. The uncertainty on the background measurement is treated as a systematic uncertainty, and is discussed in Section 5.2.2.

Sumary of Fit Results			
Method	$\sin^2\theta_W$	A_{FB}	χ^2/d.o.f.
Log likelihood	$0.231^{+0.017}_{-0.015}$	$5.0 \pm 5.9\%$	
Binned χ^2	$0.234^{+0.018}_{-0.016}$	$4.1 \pm 6.2\%$	5.6/16
Direct count	$0.230^{+0.019}_{-0.018}$	$5.4 \pm 6.8\%$	

Table 5.1: Results of the various parameter determinations after background corrections

The Z^0 sample is estimated to have fewer than 0.4 background events due to $W \rightarrow e\nu +$ jet, where the jet fakes a second electron. This background is small, but has an asymmetry of 36% as shown in Figure 4.18. For a small asymmetric background, the change in the measured asymmetry is given by

$$\Delta A_{\mathrm{FB}} = x \cdot A_{\mathrm{FB}}|_{background}, \tag{5.11}$$

where x is the fraction of background events in the sample and $A_{\mathrm{FB}}|_{background}$ is the inherent asymmetry of the background events. For the background due to W + jet, the change in the asymmetry is less than 0.06%, and is considered to be negligible.

The results of the three methods after background corrections are given in Table 5.1. The various values of A_{FB} and $\sin^2\theta_W$ show good agreement, as do the statistical uncertainties. The negative log likelihood is the preferred method for determining $\sin^2\theta_W$ because it is independent of the acceptance measurement and has the smallest statistical uncertainty. It is the log likelihood value which will be quoted as a final result.

5.2 Systematic Uncertainties

There are several potential sources of systematic uncertainty on the asymmetry measurement, arising from both physics effects and detector effects. Below we discuss each in turn and estimate the size of these systematic effects.

Method	$\sin^2\theta_W$		A_{FB} (%)	
	μ	σ	μ	σ
Log likelihood	0.2315 ± 0.0008	0.0170 ± 0.0006	4.97 ± 0.26	6.35 ± 0.21
Binned χ^2	0.2305 ± 0.0009	0.0206 ± 0.0007	5.35 ± 0.34	7.62 ± 0.25
Direct count	0.2316 ± 0.0009	0.0198 ± 0.0006	4.95 ± 0.33	7.27 ± 0.24

Table 5.2: Mean and sigma of fits to multiple toy Monte Carlo data samples

5.2.1 Fitting Uncertainties

Possible biases in the fitting procedures are investigated using a toy Monte Carlo. 500 data samples are generated according to the distribution

$$\frac{d\hat{\sigma}}{d\cos\hat{\theta}} = (1+\cos^2\hat{\theta}) + 0.1350\cos\hat{\theta}; \tag{5.12}$$

this corresponds to a forward–backward asymmetry of 5.06% and the value $\sin^2\theta_W = 0.2313$. Each Monte Carlo data sample contains 252 "events" which have been "accepted" based on the $\cos\hat{\theta}$ acceptance shown in Figure 4.13. The toy Monte Carlo data samples, then, have the same characteristics as the real Z^0 sample. Each sample is analyzed using all three methods, and a distribution of the results of each method is made. Each distribution is fitted to Gaussian form, and the mean and sigma of the Gaussian is determined for each of the distributions. The means of the distributions of extracted values should agree with the input of the toy Monte Carlo, and the sigmas of the distributions should agree with the statistical uncertainties on the real Z^0 sample. The results of these studies are given in Table 5.2. The means agree within their statistical uncertainties with the toy Monte Carlo input parameters. The sigmas are comparable to the statistical uncertainties derived from the MINUIT fits to the the Z^0 sample and shown in Table 5.1. The log likelihood method is seen to have the smallest statistical uncertainty of the three methods.

All unbiased parameter estimators should give the same results when applied to the an infinitely large data sample. With a finite number of events, however, there can be statistical fluctuations in the results of multiple estimation methods, and the results of two different

Fitter pair	$\sin^2\theta_W$		A_{FB} (%)	
	μ	σ	μ	σ
$\ln\mathcal{L}-\chi^2$	0.0010 ± 0.0004	0.0093 ± 0.0003	-0.38 ± 0.16	3.48 ± 0.11
$\ln\mathcal{L}$ - Direct	0.0000 ± 0.0004	0.0098 ± 0.0003	0.01 ± 0.16	3.67 ± 0.12
χ^2 - Direct	-0.0011 ± 0.0005	0.0118 ± 0.0004	0.40 ± 0.20	4.42 ± 0.14

Table 5.3: Mean and sigma of the distribution of the differences between fits to the toy Monte Carlo data samples.

estimators cannot be expected to agree perfectly. The size of these statistical fluctuations is investigated using the toy Monte Carlo samples discussed above. Values for each of the 500 samples are determined with all three methods, and the differences between each of the methods is taken for each sample. The mean of the distribution of differences should be 0 for two unbiased estimation methods, and the sigma is a measure of the statistical scatter expected between the two different methods when applied to the same data sample. The results are given in Table 5.3. The log likelihood and direct methods give consistent results, but the χ^2 estimation seems systematically shifted. The scatter of values determined from the Z^0 sample and given in Table 5.1 are all well within the expected limits.

The three methods of measuring A_{FB} and $\sin^2\theta_W$ are found to agree within statistical uncertainties; no systematic bias is evident in the Z^0 sample itself. Both the log likelihood and the direct methods are unbiased. The χ^2 method, however, seems to give results which are systematically shifted by approximately 0.4% in A_{FB} and 0.001 in $\sin^2\theta_W$. The systematic uncertainty on the log likelihood fit is taken to be the statistical uncertainty on the mean of the distribution of log likelihood fits to the toy Monte Carlo samples; any systematic effect smaller than this uncertainty is unmeasurable with the current Monte Carlo statistics. The systematic uncertainty on A_{FB} is taken to be 0.26% and on $\sin^2\theta_W$ is 0.0008.

5.2.2 Uncertainty in the Background Estimation

The asymmetry and $\sin^2\theta_W$ values reported in Table 5.1 have been corrected for a small background contribution. The size of the background contribution is itself uncertain, and so there is an uncertainty on the size of the background correction. The background uncertainty of 3 events and the relation of Equation 5.10 implies an uncertainty of 0.0002 on $\sin^2\theta_W$ and a relative 1.2% on the asymmetry.

5.2.3 Calorimeter Energy Scale

The calorimeter energy scale affects the measured angular distribution by affecting the boost into the rest frame of the electron pair. A global energy scale change has no effect, but differences in the energy scales between calorimeter elements can change the measured $\cos\hat{\theta}$ values.

Energy scale effects are investigated using data generated with the ISAJET [27] Monte Carlo. 50 data samples of 700 $p\bar{p} \rightarrow e^+e^-$ events each are generated. Values for $\cos\hat{\theta}$ are determined using the generated electron 4–vectors, and values for $A_{\rm FB}$ and $\sin^2\theta_W$ are extracted for each data sample. The electrons are then extrapolated to the calorimeter faces, and the 4–vectors scaled by detector–dependent scale factors to simulate energy scale differences. New $\cos\hat{\theta}$ values are calculated for each event, and new $A_{\rm FB}$ and $\sin^2\theta_W$ values are extracted for each data sample. The distribution of differences between the first and second sets of $A_{\rm FB}$ and $\sin^2\theta_W$ values is a measure of the systematic effect of energy scale changes.

Raising the PEM and FEM energy scales by 5%, a typical size for the energy corrections discussed in Section 4.3, has little effect. The mean of the distribution of differences of $\sin^2\theta_W$ values is -0.00002 ± 0.00001. Raising the energy scale of all the calorimeter elements in the West half of the detector by 5% has a slightly larger effect. The mean of the distribution of differences of $\sin^2\theta_W$ values is 0.00008 ± 0.00007. The systematic uncertainty due to energy scale effects is taken to be 0.00008 on $\sin^2\theta_W$ and 0.03% on $A_{\rm FB}$.

5.2.4 Asymmetry in $\cos\hat{\theta}$ Acceptance

All the results presented so far assume that the detector acceptance is symmetric in $\cos\hat{\theta}$. An asymmetric acceptance, however, can enhance or reduce the observed asymmetry. It is important, therefore, to measure (or set limits on) any asymmetry in the acceptance.

The acceptance is symmetric in $\cos\hat{\theta}$ if the acceptance of the physical detector is symmetric in η or if the detector acceptance is independent of the charge of the electrons. This is illustrated in Figures 5.5a-c. Figure 5.5a shows an R-z view of a random Z^0 decay in the CDF detector. Figure 5.5b shows the same event, but with the z components of the electron and positron 4–vectors reversed; this changes η to $-\eta$ for each lepton and changes the sign of $\cos\hat{\theta}$. If the detector acceptance is symmetric in η (even if it is charge dependent), then the acceptance will be the same for the event configurations shown in Figures 5.5a and 5.5b, independent of the sign of $\cos\hat{\theta}$. Since the acceptance is independent of the sign of $\cos\hat{\theta}$, it must be symmetric in $\cos\hat{\theta}$. If the detector acceptance is symmetric in η, then it is also symmetric in $\cos\hat{\theta}$. Figure 5.5c shows the event of Figure 5.5a, but with the identities of the electron and positron exchanged; the event topology in Figures 5.5a and 5.5c is the same, but the sign of $\cos\hat{\theta}$ is different. If the acceptance is independent of the signs of the electron and positron (even if it is η dependent), then the acceptance is the same for the events in Figures 5.5a and 5.5c, independent of the sign of $\cos\hat{\theta}$. Again, since the acceptance is independent of the sign of $\cos\hat{\theta}$, it must be symmetric in $\cos\hat{\theta}$. The acceptance is symmetric in $\cos\hat{\theta}$ if the detector acceptance is charge independent. An asymmetry in the $\cos\hat{\theta}$ acceptance, then, must be due to a detector effect which is both charge dependent and η dependent. No obvious effect of this type has been seen in the CDF detector, and there are no obvious charge related biases in the $W \rightarrow e\nu$ and $\mathrm{Z}^0 \rightarrow e^+e^-$ data samples.

An asymmetry in the $\cos\hat{\theta}$ acceptance can be described as a charge dependent, η dependent inefficiency; events are lost or rejected in a biased fashion. Limits on the size of any

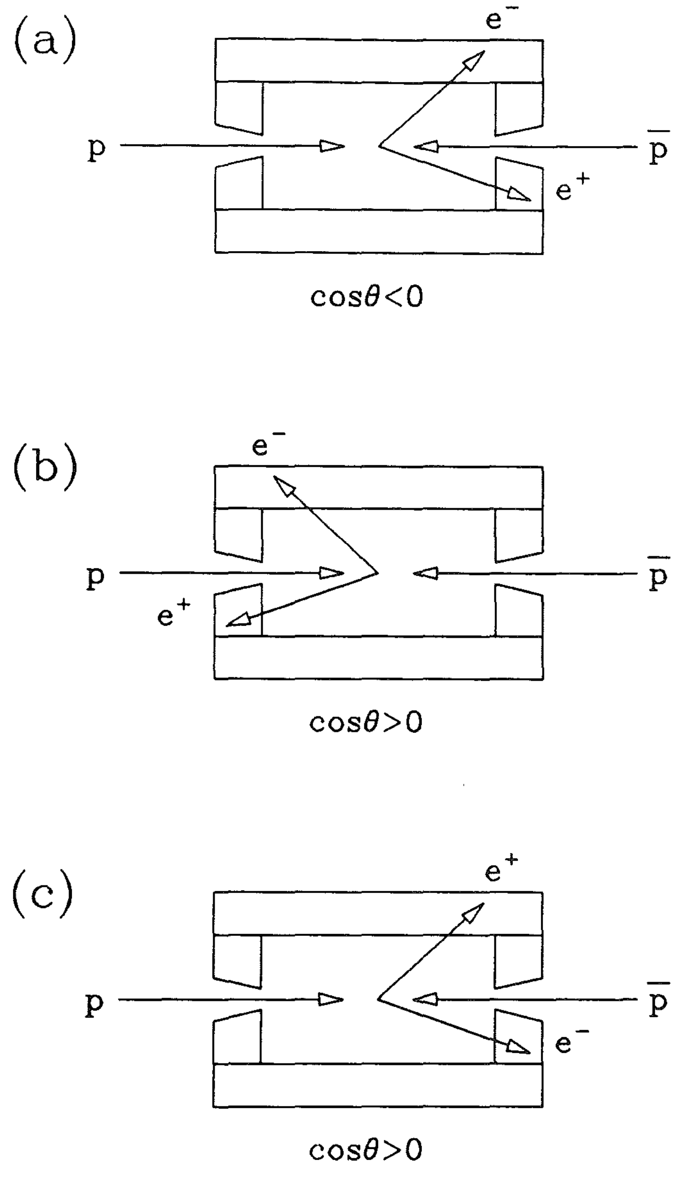

Figure 5.5: Event topologies and the sign of $\cos\hat{\theta}$. The acceptance is symmetric in $\cos\hat{\theta}$ if the detector acceptance is symmetric in η or charge independent.

potential asymmetry in the acceptance can therefore be set by examining the efficiencies of the charge dependent parameters which determine the $\cos\hat{\theta}$ acceptance. If an efficiency is very high, then its potential bias is low. In the analysis which follows, the calorimeter response is assumed to be charge independent, and therefore incapable of producing an asymmetry in the acceptance. The analysis concentrates on track related efficiencies in the central detector region.

Trigger Bias

The Level 2 ELECTRON_12 trigger requires a track from a hardware fast track processor, and is therefore potentially biased. The trigger efficiency is measured to be 97.3% efficient, however, and so any bias must be in the 2.7% of the events which fail the trigger. If all of the events which fail the ELECTRON_12 trigger have $\cos\hat{\theta}$ values with the same sign, then the forward–backward asymmetry is changed by 1.65% and $\sin^2\theta_W$ is changed by 0.0043. In fact, though, the situation is very much better than this. Any bias in $\cos\hat{\theta}$ comes from an η dependent (and charge dependent) bias in the central detector; the η dependence implies that the acceptance depends on the physical position of an electron within the central detector. For any given central electron, though, the sign of $\cos\hat{\theta}$ can change depending on the second electron in the event. This is shown in Figures 5.6a and 5.6b. The position of the central electron in each figure is the same, but the sign of $\cos\hat{\theta}$ depends on the second electron, and is different for Figures 5.6a and 5.6b. Any bias in $\cos\hat{\theta}$ due to the central electron, then, is washed out by the second electron.

A reliable estimate of the possible bias due to the trigger (or any other) efficiency requires a Monte Carlo simulation. The trigger efficiency is simulated with a linear function of charge and η given by

$$\epsilon_{Trigger} = 0.973 + (1.000 - 0.973)(Q \times \eta), \tag{5.13}$$

where Q and η are the charge and pseudorapidity of a CEM electron in a Z^0 event. This efficiency function is 100% at $Q \times \eta = 1.0$, the limit of the central fiducial region, and

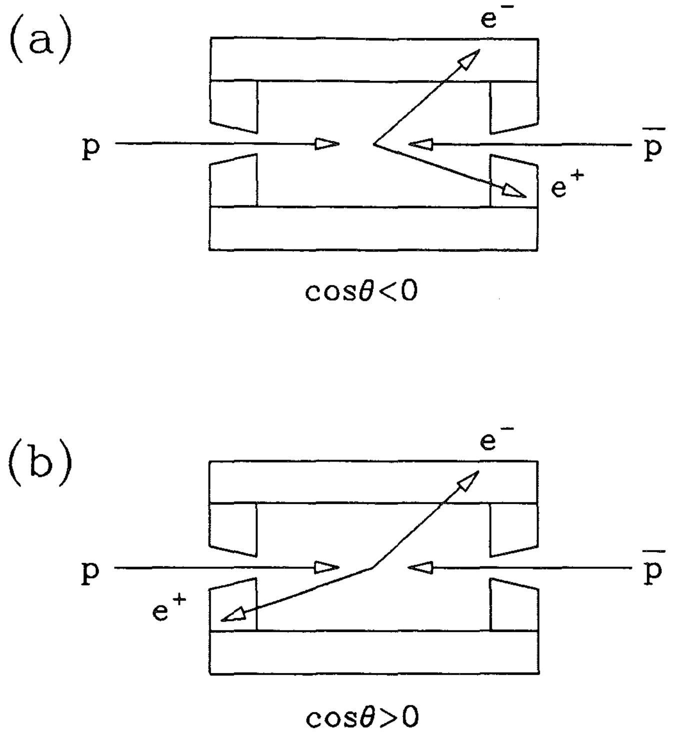

Figure 5.6: Asymmetries in the $\cos\hat{\theta}$ acceptance due to event topology and detector bias. Charge and η dependent biases on central electrons are washed out by the second electron.

the overall efficiency is constrained to be 97.3%, as measured. ISAJET is used to generate 650 Monte Carlo event samples of 252 events each. A trigger simulation is applied twice to each event sample; once to produce a subsample of events selected with an unbiased trigger efficiency of 97.3%, and once to produce a subsample of events selected with the biased trigger efficiency of Equation 5.13. Values for A_{FB} and $\sin^2\theta_W$ are extracted for the biased and unbiased subsamples, and compared. The trigger bias is given by the systematic difference in the A_{FB} and $\sin^2\theta_W$ values determined from the biased and unbiased event samples. The distribution of the differences in A_{FB} values for biased and unbiased event samples has the mean $-0.18 \pm 0.02\%$, and the distribution of the differences in $\sin^2\theta_W$ values has the mean 0.00049 ± 0.00007. There is a measurable difference between the biased and unbiased event samples. The systematic uncertainty on A_{FB} due to potential trigger bias is assigned to be 0.18%, and the uncertainty on $\sin^2\theta_W$ is taken to be 0.0005.

Track Reconstruction

The track reconstruction efficiency for the isolated, high p_t tracks associated with electrons in W and Z^0 decays is estimated to be $99 \pm 1\%$ [35]. (For a sample of cosmic rays, the track reconstruction efficiency is measured to be 99.86%.) Assuming a reconstruction efficiency of 99% linear in $Q \times \eta$, as shown in Equation 5.13 and applying the Monte Carlo analysis described above, the systematic uncertainty on A_{FB} is found to be 0.14% and the uncertainty on $\sin^2\theta_W$ is 0.0004.

Electron Quality Requirements

The electron quality requirements can introduce an asymmetry in the $\cos\hat{\theta}$ acceptance as well. The PEM and FEM calorimeter based quality requirements are assumed to be charge independent, and therefore symmetric in $\cos\hat{\theta}$. The VTPC occupancy requirement is insensitive to the curvature of particles in the solenoidal magnetic field and is assumed to be charge independent.

Potential biases in the CEM electron quality requirements are investigated using a high statistics electron sample from $W^{\pm}$ decays and a Kolmogorov–Smirnov test. The W's are selected by requiring each event to have one isolated CEM electron with E_t greater than 15 GeV satisfying fiducial volume cuts and the tight CEM electron quality requirements of Table 4.1. The W events are further required to have $\not{E}_t$ greater than 20 GeV, $\not{E}_t$ significance greater than 2.5, no jet greater than 10 GeV opposite in ϕ to the electron, and transverse mass greater than 50 GeV, where the transverse mass M_t is defined by

$$M_t = \sqrt{2E_t\not{E}_t(1 - \cos(\phi_e - \phi_{\not{E}_t}))}, \tag{5.14}$$

where ϕ_e and $\phi_{\not{E}_t}$ are the azimuthal angles of the electron and the $\not{E}_t$ vector, respectively. The electrons from the W events must satisfy the same electron requirements as the Z^0 electrons. If there are biases in the electron requirements, the W and Z^0 electrons will be affected in the same way, and any potential bias will be more easily observed with the higher statistics of the W sample.

The Kolmogorov–Smirnov (or K–S) test is used to compare two sample distributions, and gives a measure of the probability that both sample distributions are drawn from the same parent probability distribution. The K–S test is valid for unbinned distributions of a single variable, and is based on cumulative (or integrated) probability distribution functions. If one defines a range of interest from x_{min} to x_{max} containing N events with values $x_i, i = 1, \ldots, N$, then the cumulative probability distribution function $S_N(x)$ gives the fraction of the data points which lie in the range of interest but have values less than x. $S_N(x)$, then, has the value 0 at $x = x_{min}$ and 1 at $x = x_{max}$, and increases in steps of $1/N$ at each x_i. For two cumulative distribution functions $S_N(x)$ and $S'_N(x)$, the K–S statistic D is defined as the absolute value of the maximum difference between $S_N(x)$ and $S'_N(x)$ over the interval from x_{min} to x_{max}, *i.e.*

$$D = max|S_N(x) - S'_N(x)|. \tag{5.15}$$

If the two samples have nearly the same cumulative probability distribution, then the difference D will be small.

The K–S test is a hypothesis test; it attempts to disprove (at some confidence level) the hypothesis that the two sample distributions are drawn from the same parent distribution. The distribution of the K–S statistic D is known for two sample distributions which are drawn from the same parent distribution. One can therefore calculate for a given value of D the probability that the two sample distributions are drawn from the same parent distribution. While one can never prove that two samples come from the same parent distribution, one can use the D distribution to prove that, at some confidence level, the two samples are not drawn from the same distribution.

The K–S test is used to find charge and η dependent differences in the distributions of the CEM electron quality parameters. If, according to the K–S test, a parameter distribution is significantly different for electrons and positrons, then the parameter is charge dependent. Similarly, if the K–S test indicates that a parameter's distributions are different for electrons in the East and West halves of the detector, then the parameter is η dependent. If one of the quality parameters is both charge and η dependent, then it is assumed to be biased, and its effect on the asymmetry is measured with the Monte Carlo technique described above.

The K–S tests indicate that, at the 95% confidence level, there are significant differences in the E/p and Δz distributions for electrons in the East and West halves of the detector, and in the Δx distribution for positrons and electrons. Differences are also seen in the other distributions for these three quality parameters, and so these three parameters are assumed to be biased. The cumulative probability distributions for positrons and electrons and for electrons in the East and West halves of the detector are shown in Figure 5.7 for these three quality parameters. The East–West and positron–electron distributions are consistent, at this confidence level, for the LSHR, χ^2_{strip}, and isolation parameters. The LSHR, χ^2_{strip} and isolation parameters depend only on calorimeter information, and are believed to be unbiased.

The efficiency of the Δz cut is measured to be 98.5% from the studies of Z^0 electrons as

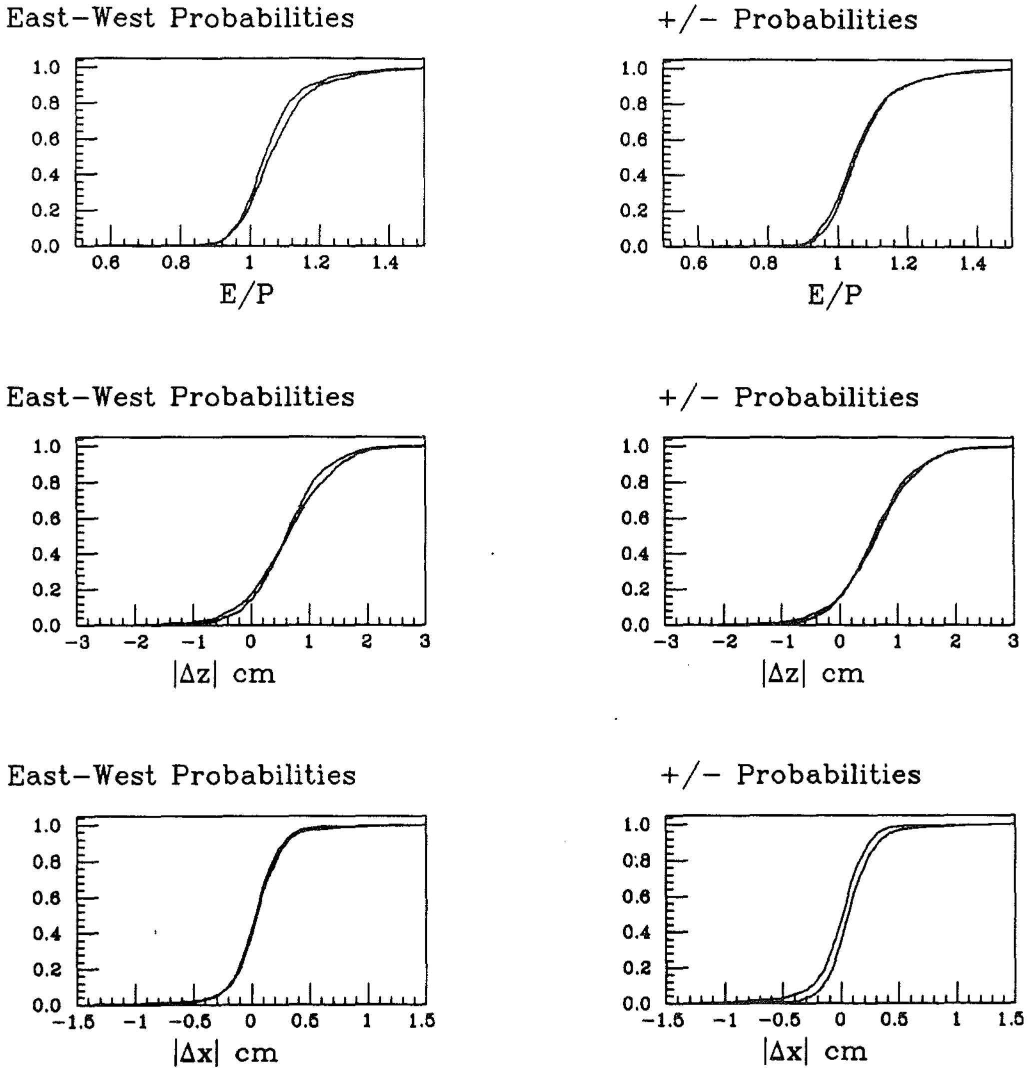

Figure 5.7: Cumulative probability distributions for the E/p, $|\Delta x|$, and $|\Delta z|$ quality parameters for positrons and electrons and for electrons in the East and West halves of the CDF detector.

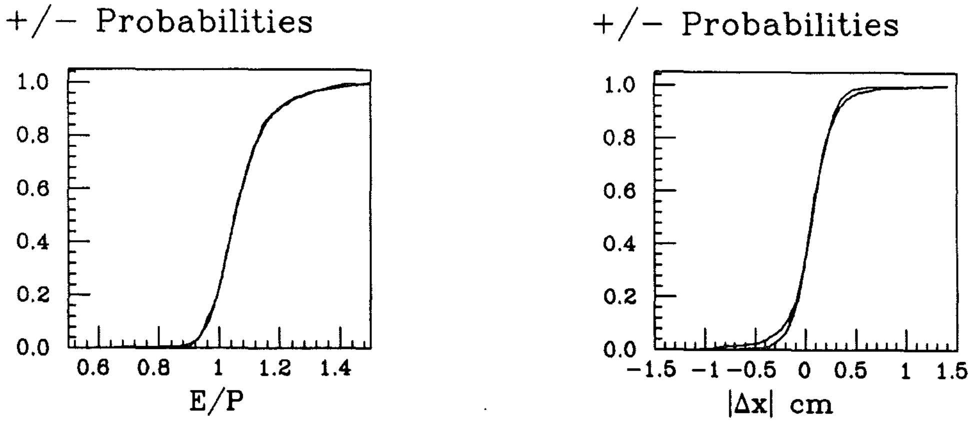

Figure 5.8: Cumulative probability distributions for the E/p and $|\Delta x|$ quality parameters for positrons and electrons after shifting the positron distributions.

described in Section 4.5. Inserting this efficiency into Equation 5.13 and using the Monte Carlo to estimate the size of the bias, the systematic uncertainty on on A_{FB} is found to be 0.06%, and the uncertainty on $\sin^2\theta_W$ is 0.0002.

The efficiencies of the E/p and Δx cuts are smaller than that of the Δz cut; 91.2% for E/p and 96.3% for Δx. Measuring the bias directly from these efficiencies would overestimate their effect. Instead, the potential bias is measured from the difference in the efficiencies for positrons and electrons. The E/p and Δx distributions are shifted for positrons and electrons, as can be seen in Figure 5.7. This is consistent with a charge–dependent error on the track reconstruction. By shifting the positron and electron distributions by some small amount, one can restore the charge independence of these two cuts. Figures 5.8a and 5.8b show the E/p and Δx distributions for positrons and electrons after shifts of 0.0101 in E/p and 0.0543 cm in Δx. The cumulative probability distributions agree well after the shifts.

The actual electron selection cuts are made on the unshifted distributions, however, and so there are relative differences in the efficiencies for positrons and electrons. The efficiency of the E/p cut for positrons is measured to be 99.92% of the efficiency of the E/p cut for electrons. Similarly, the efficiency of the Δx cut for positrons is measured to be 99.92% of the efficiency of the Δx cut for electrons. These relative efficiencies are inserted into the Monte Carlo, and estimates of the potential bias are derived. The Monte Carlo studies are statistics limited for these two parameters, and indicate uncertainties of 0.006% on A_{FB} and 0.00002 on $\sin^2\theta_W$ for both the E/p and Δx requirements.

The individual systematic uncertainties for the Δz, Δx, and E/p cuts are added in quadrature to arrive at an overall systematic uncertainty for the electron quality requirements. The overall uncertainty is assigned to be 0.06% on A_{FB} and 0.0002 on $\sin^2\theta_W$.

5.2.5 Quark Distribution Functions

The relationship between the observed forward–backward asymmetry and $\sin^2\theta_W$ depends on the relative contributions of u–type and d–type valence and sea quark production. The values derived for $\sin^2\theta_W$ therefore have an implicit dependence on the momentum distribution functions for the quarks inside the proton. There are uncertainties in the distribution function parametrizations, particularly at small x where the proton structure functions are not experimentally well–measured. The systematic uncertainty on $\sin^2\theta_W$ due to distribution function uncertainties is estimated by fitting the data using several different distribution function parametrizations[16, 36, 37, 38]. The results of log likelihood fits to the Z^0 data are shown in Table 5.4 for several distribution functions, along with the ratio of u–type to d–type contributions and the ratio of sea–sea to valence contributions for each parametrization. The systematic uncertainty on $\sin^2\theta_W$ due to uncertainty in the distribution functions is taken to be 0.00035, half the spread in the fitted $\sin^2\theta_W$ values. The uncertainty in the distribution functions does not imply an uncertainty on the measured asymmetry; the distribution functions are used only in relating the observed forward–backward asymmetry to

Log–Likelihood Fit Results 1988–1989 Data CDF PRELIMINARY				
Parametrization	$\sin^2\theta_W$	Uncertainty	u/d Ratio	Sea/Valence
EHLQ 1 [16]	0.2314	0.0158	2.34	0.23
EHLQ 2 [16]	0.2314	0.0158	2.29	0.24
DO 1 [36]	0.2315	0.0163	1.58	0.30
DO 2 [36]	0.2309	0.0167	1.58	0.30
DFLM 1 [37]	0.2316	0.0158	2.09	0.24
DFLM 2 [37]	0.2315	0.0159	2.09	0.25
DFLM 3 [37]	0.2311	0.0158	2.16	0.25
MRSE [38]	0.2315	0.0162	1.79	0.28
MRSB [38]	0.2313	0.0162	1.96	0.27

Table 5.4: Log likelihood fit results for various parton distribution function parametrizations

	A_{FB}	$\sin^2\theta_W$
$\ln\mathcal{L}$ fitter	0.26%	0.0008
QCD Background	0.06%	0.0002
Energy Scale	0.03%	0.0001
Electron Trigger	0.18%	0.0005
Track Reconstruction	0.14%	0.0004
Electron Selection	0.06%	0.0002
Parton Distribution	-	0.0004
Add in Quadrature	0.36%	0.0011

Table 5.5: Systematic uncertainties on A_{FB} and $\sin^2\theta_W$.

$\sin^2\theta_W$.

5.2.6 Summary of Systematic Uncertainties

The systematic uncertainties on the measurement of the forward–backward asymmetry and $\sin^2\theta_W$ are summarized in Table 5.2.6. The uncertainty in the momentum distribution functions affects only the determination of $\sin^2\theta_W$ from the measured asymmetry, not the asymmetry measurement itself. In all cases, the systematic uncertainties are very much smaller than the statistical uncertainty on the measurement. When the individual uncertainties are added in quadrature, the overall uncertainty on A_{FB} is 0.35% and on $\sin^2\theta_W$ is 0.0011.

Chapter 6

Radiative Corrections

There are many higher order diagrams which contribute to inclusive dielectron production in $\bar{p}p$ collisions. The QCD diagrams shown in Figure 6.1 produce dielectrons with non-zero transverse (to the beam direction) momentum, p_t^Z. The order α^3 electroweak contributions to $q\bar{q} \rightarrow e^+e^-(\gamma)$ shown in Figure 6.2 [39] are also a source of dielectron events. These higher order processes have a significant effect on the angular distribution of the dielectrons. Initial state QCD radiation smears the $\cos\hat{\theta}$ values reconstructed from the electron 4-vectors, as discussed in Section 2.2, while higher order QED processes contribute directly to the forward–backward asymmetry. The physics processes which produce the (measured) forward–backward asymmetry includes all of these higher order contributions. The $\sin^2\theta_W$ values, however, are extracted from the measured asymmetry using only the lowest order

Figure 6.1: Next order QCD contributions to Z^0 production.

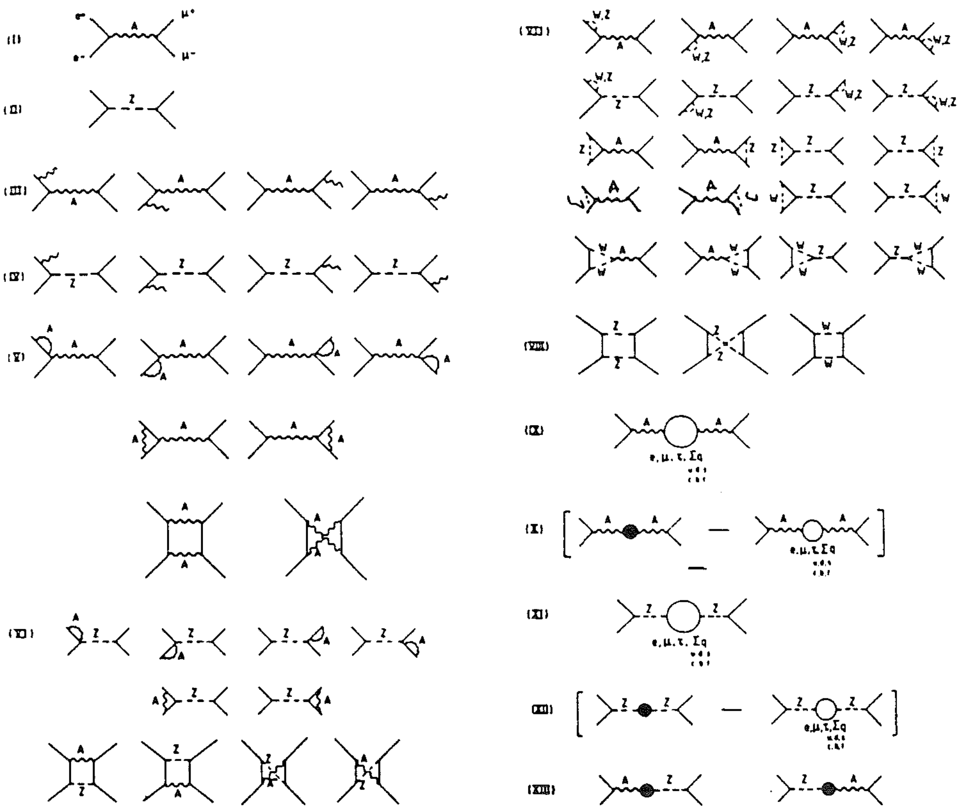

Figure 6.2: Order (α^3) QED and weak diagrams contributing to $q\bar{q} \rightarrow e^+e^-$. Taken from Reference [39].

cross section. The extracted $\sin^2\theta_W$ values must therefore be corrected to account for the higher order contributions to the forward–backward asymmetry. Furthermore, when higher order weak corrections are included, the values of $\sin^2\theta_W$ determined from different physical processes require very different corrections, and care must be taken in comparing different measurements of $\sin^2\theta_W$.

The higher order corrections divide themselves naturally into QCD, QED, and weak corrections. The QCD corrections are independent of the electroweak corrections and can be treated separately. The electroweak corrections are more complex, and must be treated within the framework of a renormalization scheme. The on–shell renormalization scheme first proposed by Ross and Taylor [40] and described in Reference [41] uses the fermion masses, α, M_Z, M_W, and M_{Higgs} as input parameters, and has the property that the QED diagrams are separable as a class. In this renormalization scheme, the QED sector is separately renormalizable, and QED quantities can be calculated independent of the remaining weak corrections. In the on–shell renormalization scheme, $\sin^2\theta_W$ is not an independent parameter, but is most naturally defined in terms of the W and Z^0 masses by

$$\sin^2\theta_W|_{Sirlin} \equiv 1 - \frac{M_W^2}{M_Z^2}. \tag{6.1}$$

This is the so-called Marciano–Sirlin [42] definition of $\sin^2\theta_W$.

In the subsequent sections, the effects of each of the different categories of higher order corrections on the forward–backward asymmetry and the interpretation of $\sin^2\theta_W$ are examined. The object of these correction procedures is first to account for higher order contributions to the measured asymmetry, and then to derive a value for a commonly accepted definition of $\sin^2\theta_W$ based on the corrected asymmetry. Explicit formulas and equations used in the analysis of the higher order contributions are given in Appendix A.

6.1 QCD Corrections to the Asymmetry

The scattering angle $\hat{\theta}$ is defined to be the angle between the outgoing electron and incoming quark (or outgoing positron and incoming antiquark) in the rest frame of the electron pair. The initial quark directions, however, are not always well–defined in $p\bar{p}$ collisions. Due to the higher order QCD processes shown in Figure 6.1, Z^0's are produced with varying amounts of transverse momentum, p_t^Z. When a Z^0 is produced with non–zero p_t^Z, the proton and antiproton directions are not collinear in the rest frame of the dielectrons, and so the quark directions can not be completely determined: the quarks can only be said to be travelling in approximately the direction of the proton or antiproton, and the approximation gets worse as p_t^Z increases. Since the initial quark directions are ill–defined, $\cos\hat{\theta}$ can no longer be precisely measured.

In practice, a new $\hat{z}$ axis is defined in the dielectron rest frame to take the place of the quark direction when making angular measurements. The definition used in this analysis is that of Collins and Soper [19], in which the $\hat{z}$ axis is taken to be the bisectrix of the proton and minus the antiproton directions, as shown in Figure 2.6. As described in Section 2.2, the Collins–Soper definition divides the p_t^Z contribution equally between the quark and antiquark, and has the property that $\hat{z}$ reduces to the quark direction in the limit $p_t^Z \rightarrow 0$.

The Collins-Soper definition of $\cos\hat{\theta}$ is an approximation which begins to break down at high values of p_t^Z. The $\cos\hat{\theta}$ distribution will therefore be smeared somewhat by the high p_t^Z events, and the measured asymmetry will be smaller than the true asymmetry due to this smearing of $\cos\hat{\theta}$ measurements. The size of this effect can be determined from the QCD corrected angular distribution.

There are several calculations of the differential cross section for Z^0 production and decay which include the diagrams of Figure 6.1, and incorporate the Collins–Soper definition of $\cos\hat{\theta}_{CS}$ explicitly [18, 19, 43]. Reference [43] gives the result [1] (for the Z^0 contribution to

---

[1] The cross section also depends on $\hat{\phi}$, where $\hat{\phi}$ is the azimuthal angle of the outgoing electron defined with

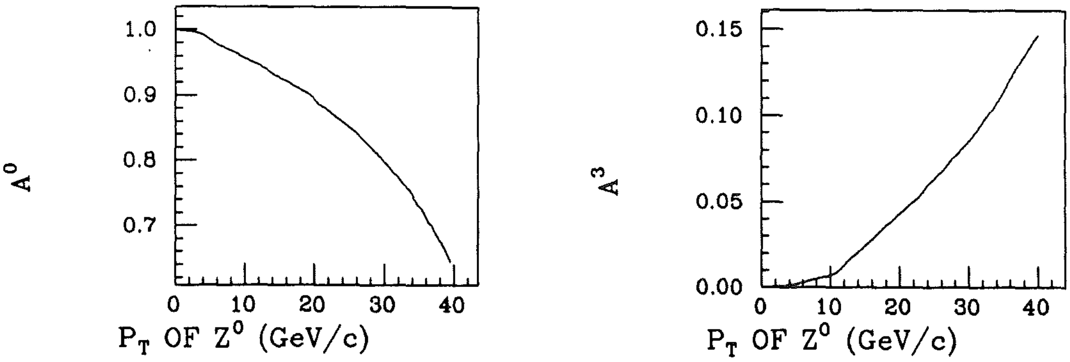

Figure 6.3: Plots of the p_t^Z dependent QCD correction factors A^0 and A^3. Taken from Reference [43].

the cross section only)

$$\begin{aligned}\frac{d\sigma}{d\cos\theta_{CS}\;dp_t^Z} &= \frac{d\sigma}{dp_t^Z}\Big\{[((g_V^e)^2+(g_A^e)^2)((g_V^q)^2+(g_A^q)^2)] \\ &\quad\times[(1+\cos^2\theta_{CS}+\tfrac{1}{2}A_0(1-3\cos^2\theta_{CS}))] \\ &\quad+8g_V^e g_A^e g_V^q g_A^q(1-A_3)\cos\theta_{CS}\Big\} \qquad (6.2)\end{aligned}$$

where $\frac{d\sigma}{dp_t^Z}$ is the measured Z^0 p_t^Z spectrum. A_0 and A_3 are functions of p_t^Z and reduce to 0 as $p_t^Z \rightarrow 0$. Plots of A_0 and A_3, taken from Reference [43], are shown in Figure 6.3. Equation 6.3 predicts the measured angular distribution, including the effects of p_t^Z smearing of $\cos\hat{\theta}$ values, in the Collins–Soper frame. From this angular distribution a $\sin^2\theta_W$ independent, p_t^Z dependent multiplicative correction factor for the asymmetry can be derived.

---

respect to the plane containing the proton and antiproton in the rest frame of the electron pair. Equation 6.3 has been integrated over $\hat{\phi}$ to remove this dependence.

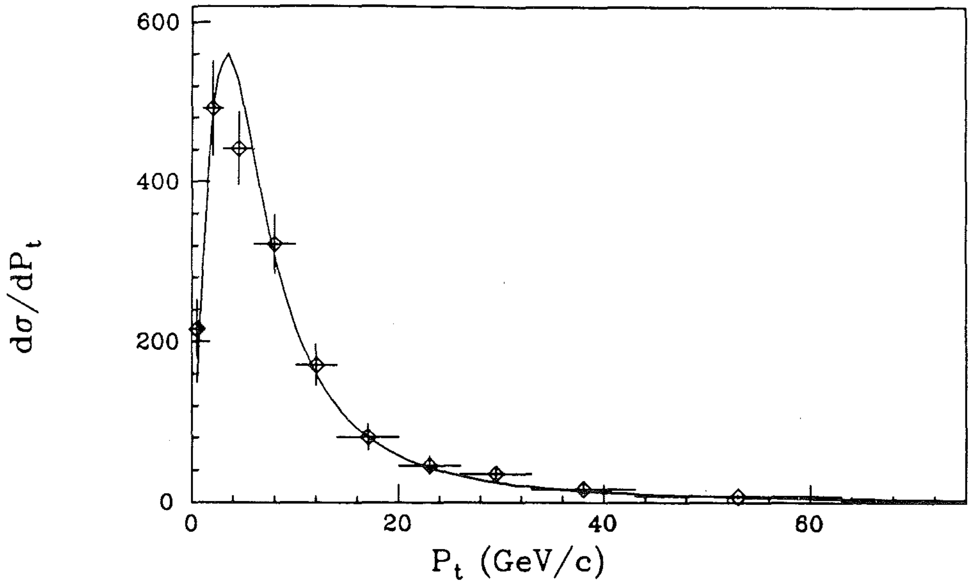

Figure 6.4: Transverse momentum of Z^0's after corrections to remove resolution smearing. The points show the CDF data and the line shows an ISAJET based parametrization.

Integrating Equation 6.2 over $\cos\hat{\theta}$ to find the measured asymmetry, one derives

$$A_{\mathrm{FB}}|_{Measured} = A_{\mathrm{FB}}|_{p_t^Z=0} \int \frac{d\sigma}{dp_t^Z} \, (1 - A_3) \; dp_t^Z, \tag{6.3}$$

where $A_{\mathrm{FB}}|_{p_t^Z=0}$ is the forward–backward asymmetry at $p_t^Z = 0$. The p_t^Z dependent changes to the full angular distribution of Equation 2.29 are made by substituting $(1 + \cos^2\theta_{CS} + \frac{1}{2}A_0(1 - 3\cos^2\theta_{CS}))$ for $(1 + \cos^2\hat{\theta})$ and $(1 - A_3)\cos\theta_{CS}$ for $\cos\hat{\theta}$. The result of Equation 6.3 applies as well for the full cross section.

The measured Z^0 p_t^Z spectrum can be parametrized by a modified form of the p_t^Z spectrum used in the ISAJET [27] Monte Carlo. After correcting the data for smearing due to the finite resolution of the energy measurements, the Z^0 p_t^Z spectrum is well described by the parametrization [44]

$$\frac{d\sigma}{dp_t^Z} = 70535.(p_t^Z)((p_t^Z)^2 + 26.00)^{-1.666.} \tag{6.4}$$

The data and the parametrization are shown in Figure 6.4 [44]. Convolving this measured p_t^Z spectrum with $(1 - A_3)$ as shown in Equation 6.3, the QCD corrections are found to reduce the measured asymmetry by a relative 1.2% with respect to the lowest order asymmetry at $p_t^Z = 0$. This implies that the value of $\sin^2\theta_W$ extracted from the lowest order cross section must be increased by 0.0002.

6.2 QED Contributions to the Asymmetry

The order α^3 QED contributions to $q\bar{q} \rightarrow e^+e^-(\gamma)$ are shown in groups III, IV, V, and VI of Figure 6.2. They consist of all the graphs having an additional real or virtual photon. Note that the fermion loop correction to the photon propagator, shown in group IX of Figure 6.2 is excluded from the current discussion of QED corrections, but will be included with the Z^0 and γ-Z^0 propagator corrections in the weak corrections. To order α^3, the cross section has contributions from (1) the lowest order diagrams (which are of order α^2), (2) the interference between the lowest order diagrams and the diagrams having an additional virtual photon (virtual diagrams), and (3) the diagrams having a real photon emitted from the initial or final fermions (bremsstrahlung diagrams). The bremsstrahlung diagrams have a 3–body final state, in contrast to the two–body final state of lowest order and virtual diagrams. The total cross section for $q\bar{q} \rightarrow e^+e^-(\gamma)$, then, is given by the sum of the two–body and three–body cross sections. Both the 2–body and 3–body cross sections are infrared divergent. These divergences cancel when the two cross sections are added, and so the total cross section is infrared–finite.

The bremsstrahlung contribution can be divided into a "soft" part and a "hard" part by an infrared cutoff k_0 in the fraction of a fermion's energy carried off by a bremsstrahlung photon. The soft photons having energy fractions less than k_0 are not resolved by the detector, and appear as part of the electron shower in the calorimeter. This soft bremsstrahlung contribution is indistinguishable from a 2–body final state, and so it can be calculated analytically and added to the virtual cross section. The sum of the virtual and soft bremsstrahlung contributions is infrared finite, as is the remaining hard bremsstrahlung cross section.

The hard bremsstrahlung photons are potentially very energetic, and can be produced at large angles to their parent fermions. The hard photons, then, can interact independently with the detector. Furthermore, the higher order soft contributions change the dielectron angular distribution in a non-trivial way, and thus the QED corrections to the asymmetry will depend on the detector geometry and acceptance. Because of these inherent detector dependences, the QED corrections are best studied with a Monte Carlo event generator which includes both hard and soft corrections, and a detector simulation.

6.2.1 Soft QED Contributions

The soft portion of the order α^3 QED cross section is calculated by many authors for $e^+e^- \to f\bar{f}(\gamma)$ at LEP and SLC, but is largely ignored for $q\bar{q} \to f\bar{f}(\gamma)$. This being the case, the LEP/SLC results are time-reversed to get predictions for $q\bar{q} \to e^+e^-(\gamma)$. The matrix elements for the virtual diagrams are invariant under time reversal, and so the published results can be used without change. The soft bremsstrahlung contributions differentiate between initial and final state radiation, and require a little more care.

The soft corrections used in the current analysis are taken from Reference [14]. The authors include all the diagrams in groups III, IV, V, and VI of Figure 6.2, and include the contribution of soft photons to all orders in α by exponentiation of the leading logarithms of the soft bremsstrahlung terms as described in Reference [45].

In the LEP calculations, the soft initial state bremsstrahlung corrections incorporate terms of the form

$$\frac{1}{M^2 - (s - 4E\Delta E)} \tag{6.5}$$

where $M^2 = M_Z^2 - iM_Z\Gamma_Z$, E is the energy of the electron beams in the LEP accelerator, $\Delta E = k_0 E$ is the maximum energy of a photon from initial state bremsstrahlung, and

$s = 4E^2$ is the square of the center of mass energy of the machine. The term $(s - 4E\Delta E)$ is interpreted as the square of the effective center of mass collision energy of the interaction after initial state bremsstrahlung. Terms of this form enter the cross section in multiplicative scale factors and in a correction to the phase of the Z^0 resonance. The "prescription" for converting these terms to a form usable for $q\bar{q} \rightarrow e^+e^-$ interactions is to interpret E as the energy of the outgoing electrons in the center of mass frame, ΔE as the energy of a photon from final state bremsstrahlung, and s as the square of the dielectron invariant mass. The square of the effective center of mass collision energy of the interaction before final state bremsstrahlung is then $(s + 4E\Delta E)$. To convert the LEP calculations to $p\bar{p}$ calculations, one must change the sign of the ΔE term in the bremsstrahlung coefficients, and to change the interpretation of s.

The forward–backward asymmetry is corrected in different ways by each of the types of QED diagrams. The virtual vertex corrections can be absorbed into a renormalization of the photon and Z^0 couplings to fermions. This is an s dependent correction which affects both the symmetric and antisymmetric parts of the cross section and leaves the asymmetry unchanged.

The soft initial state bremsstrahlung correction is an s dependent, multiplicative correction to the cross section which has no effect on the asymmetry. The soft final state bremsstrahlung contribution has a multiplicative part which does not change the asymmetry, but it also has a part which affects the phase angle of the Z^0 resonance, which does affect the asymmetry. In the presence of soft final state bremsstrahlung, the Z^0 line shape grows a "shoulder" on the low mass side of the resonance, as shown in Figure 6.5. The shoulder is due to events produced on resonance which then radiate a photon as they decay; the reconstructed dielectron invariant mass of these events is decreased by the photon radiation. The asymmetry of the events in the shoulder region is characteristic of resonance production, however, and is larger than expected. This can be seen in Figure 6.6, where the the forward–backward asymmetry is plotted as a function of M_{ee}. The size of this effect

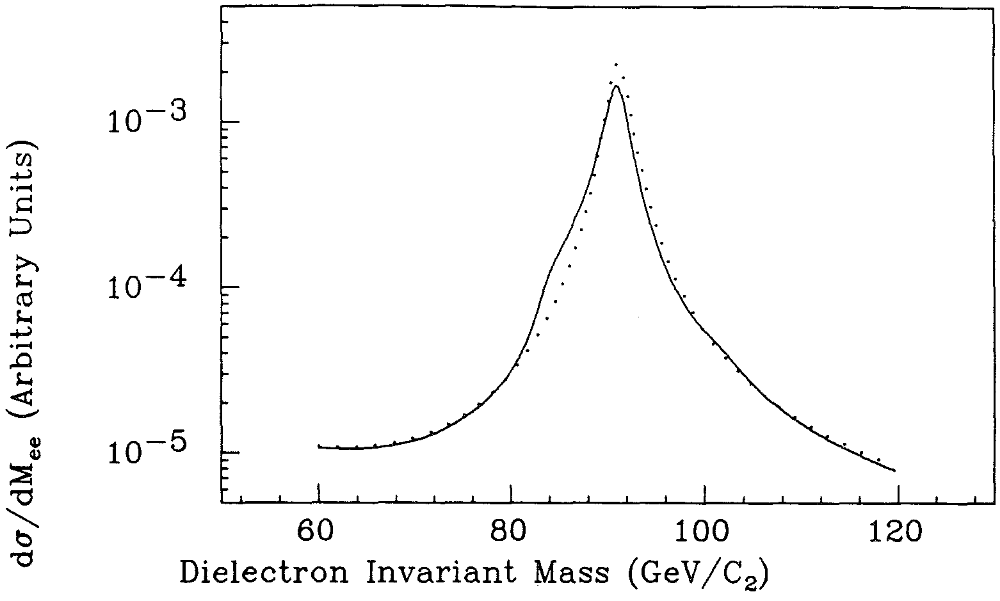

Figure 6.5: Dielectron cross section as a function of center of mass collision energy, with (solid) and without (dotted) Order (α^3) QED contributions.

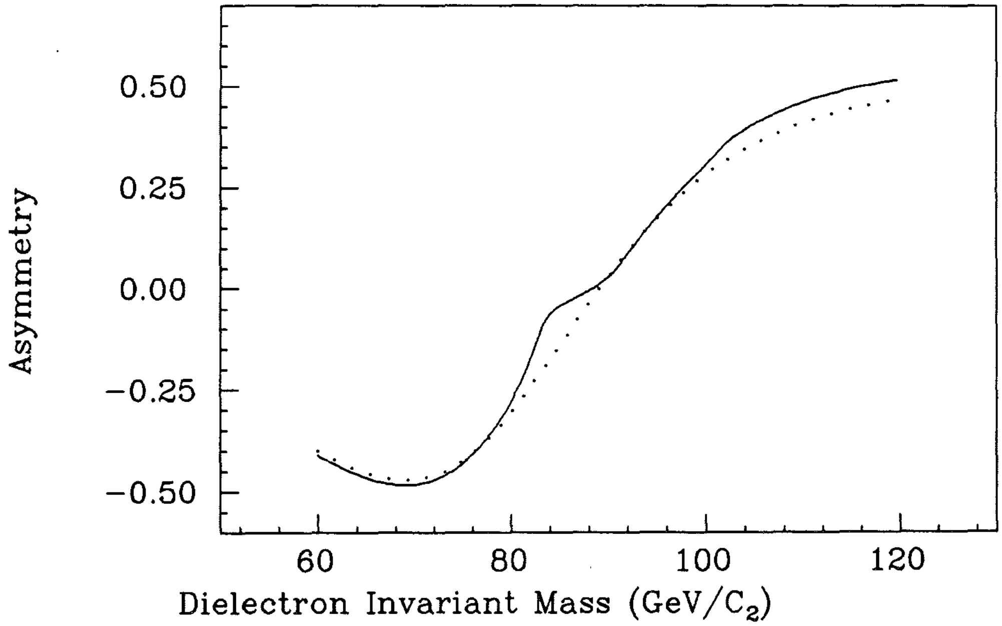

Figure 6.6: Forward–backward asymmetry as a function of center of mass collision energy, with (solid) and without (dotted) order (α^3) QED contributions.

increases as the cutoff k_0 increases.

The initial and final state bremsstrahlung diagrams have different charge conjugation parities [46], and so the interference between these diagrams will contribute to the charge asymmetry, as discussed in Section 2.1. The size of the correction to the asymmetry from the radiative Z^0 diagrams is found to vary strongly with the cutoff k_0 [47]; it is small for large values of k_0 ($\delta A_{\mathrm{FB}} \simeq -0.07\%$ at $k_0 = 0.1$) and increases as k_0 increases ($\delta A_{\mathrm{FB}} \simeq -0.80\%$ at $k_0 = 5 \times 10^{-4}$).

The QED box diagrams have an additional virtual photon propagator, and therefore have different charge conjugation parities from the lowest order diagrams with which they interfere. The box diagrams, then, also contribute to the observed charge asymmetry. The contribution is small ($\delta A_{\mathrm{FB}} \simeq 0.08\%$) and is independent of both $\sin^2\theta_W$ and k_0.

It is convenient to show the QED corrections as a function of the charge asymmetry, A_C, where the charge asymmetry is defined by

$$A_C \equiv \frac{\left.\frac{d\sigma}{d\cos\hat{\theta}}\right|_{+\cos\hat{\theta}} - \left.\frac{d\sigma}{d\cos\hat{\theta}}\right|_{-\cos\hat{\theta}}}{\left.\frac{d\sigma}{d\cos\hat{\theta}}\right|_{+\cos\hat{\theta}} + \left.\frac{d\sigma}{d\cos\hat{\theta}}\right|_{-\cos\hat{\theta}}}. \tag{6.6}$$

The corrected and uncorrected charge asymmetries on resonance for $\mathrm{u\bar{u}} \rightarrow e^+e^-$, $\mathrm{d\bar{d}} \rightarrow e^+e^-$, and $\mu\bar{\mu} \rightarrow e^+e^-$ are shown in Figure 6.7. The dashed lines show tree level calculations, while the solid lines include all the soft QED corrections evaluated at $k_0 = 0.01$. The size of the QED corrections depends on the sign and magnitude of the initial fermion's charge.

6.2.2 Hard Contributions and the Radiative Monte Carlo

Hard photon emission smears the measured dielectron quantities; initial state bremsstrahlung can disturb the reconstruction of $\cos\hat{\theta}$ by adding a small amount of transverse momentum, and final state bremsstrahlung can directly affect the energy and direction of outgoing electrons. Unlike the soft corrections, which can either increase or decrease the asymmetry depending on the charges of the fermions in the interaction, the hard corrections always

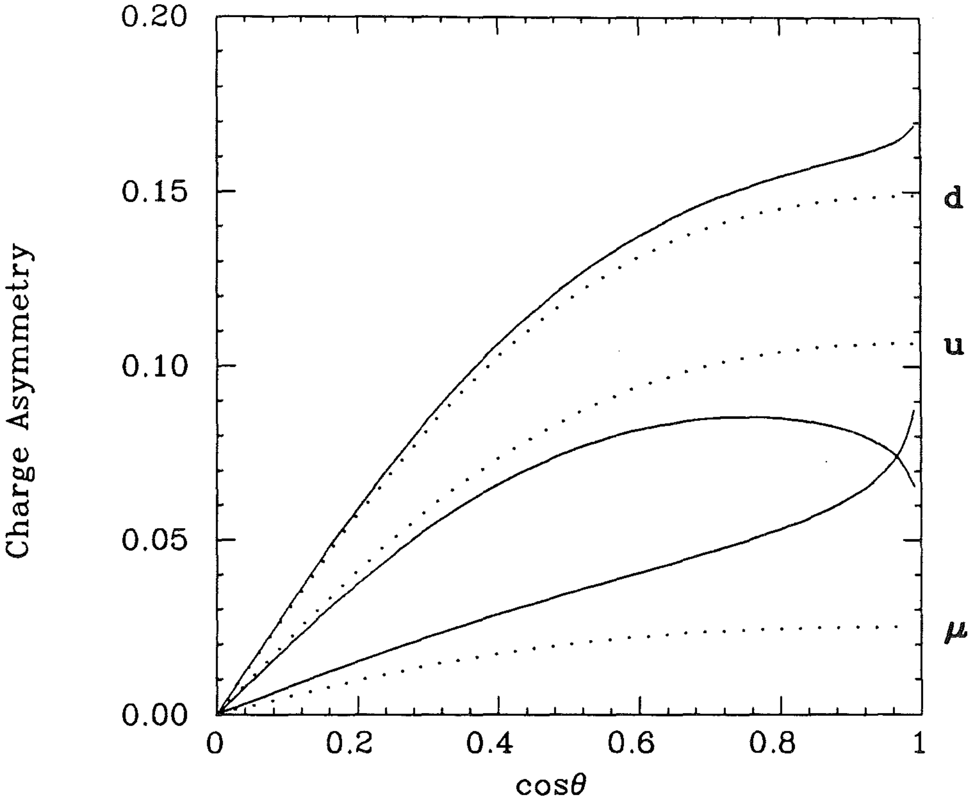

Figure 6.7: Charge asymmetries for $f\bar{f} \to e^+e^-$ with (dotted) and without (solid) order (α^3) contributions.

decrease the measured asymmetry by smearing the $\cos\hat{\theta}$ distribution. Since hard photons emitted in the process $f\bar{f} \rightarrow e^{+}e^{-}\gamma$ can interact in the detector and affect the measurement of electron quantities and $\hat{\theta}$, a proper treatment of the hard photon contribution requires a Monte Carlo event generator and a detector simulation.

The Monte Carlo generator used in this analysis is a modified version of the generator developed for the CDF Z^0 mass analysis [48]. It is based on the hard bremsstrahlung calculations of Reference [49] and includes the soft corrections of Reference [14]. The hard bremsstrahlung calculation includes only final state radiation; hard initial state radiation has little effect on Z^0 production in hadronic collisions. Collinear photons from initial state radiation generally escape undetected down the beampipe. Large angle radiation from the quarks can produce transverse momentum p_t^Z, which can affect the reconstruction of the final state in the manner described above for the QCD corrections. This effect is very small for photons, and is ignored in this analysis.

The Monte Carlo generates the proper 2 and 3 body angular distributions using a rejection method, and then weights each event by the convolution of the cross section with quark distribution functions. Since the angular part of the cross section is generated separately, the weight needs only account for the $\hat{s}$ dependence of the cross section. For the 2–body state, the cross section used in the weight is the soft QED cross section evaluated at $\cos\hat{\theta} = 0$. For the 3–body state, the cross section used is the lowest order cross section evaluated at $\cos\hat{\theta} = 0$ multiplied by $\delta_Q^h(k_0)$, where $\delta_Q^h(k_0)$ is the probability of producing a photon with energy fraction greater than k_0, and is derived by integrating the photon energy spectrum from k_0 to 1. Forms for the photon spectrum and $\delta_Q^h(k_0)$ are given in Reference [49] and in the Appendix.

The Monte Carlo event generation proceeds as follows:

1. Values for x_1 and x_2, the fractional momenta of the quarks, are generated, and the resulting invariant mass is checked against the desired mass limits.

2. The event is assigned, with equal probability, to one of 4 possible production processes: (a) u quark from the proton, $\bar{u}$ quark from the antiproton, (b) d quark from the proton, $\bar{d}$ quark from the antiproton, (c) $\bar{u}$ quark from the proton, u quark from the antiproton, and (d) $\bar{d}$ quark from the proton, d quark from the antiproton. A weight is then calculated based on the parton distribution functions for u or d quarks and the fractional momenta calculated previously.

3. The event is chosen, with equal probability, to have a 2–body or 3–body final state.

4. The angular distribution of the outgoing particles is generated with a rejection procedure . For 2–body final states, the angular distribution of Reference [14] is used, while 3–body final states are generated according to the distribution of Reference [49].

5. A weight for the event is calculated from the cross section as a function of $\hat{s}$, as described above.

6. The overall weight for the event is calculated from the product of the the weight from the quark distribution functions and the weight from the cross section.

The final state 4–vectors and the event weight are the input for the detector simulation. The detector simulation must include the geometric features of the detector and the resolutions of the various detector elements, and must also be able to simulate the effects of the bremsstrahlung photons. Moreover, it must be fast; the QED corrections require several million events to be simulated in order to achieve the desired statistical accuracy.

The detector simulation used in this analysis is a modified form of the simulation used to determine the acceptance and described in Section 4.6. The 2–body final states are simulated the same manner as the events used in the acceptance calculations. For the 3–body final states, the photon showers in the calorimeter and the effect of the photon on the electron measurement becomes important. For photons emitted at very small angles to the electron, the electron and photon showers are indistinguishable. The "electron" will be accepted by the analysis cuts, and the total energy measured by the calorimeter is the sum of the electron and photon energies. For photons with small energies, the effect of the photon on the electron measurement is small. The electron will pass the analysis cuts, and the photon will have little effect on the electron's energy or direction. For photons having an intermediate energy emitted at a moderate angle with respect to the electron, the effect of the photon is less clear. Electrons with energetic photons very near by may fail a shower shape cut like the strip χ^2 in the CEM or the 3×3 χ^2 in the PEM. Events with separated electron and photon showers may fail the isolation cut.

These electron acceptance effects are studied using a sample of 20000 radiative Monte Carlo events which are simulated with the full CDF detector simulation program. The simulated events are then passed through the electron selection cuts used in this analysis. Using these simulated events, the photon angles and energies which still allow the electrons to pass the selection cuts can be identified. The available photon phase space can be parametrized, and the parametrization used quickly to accept or reject events. Figure 6.8 shows a plot of the photon–electron angle versus the fractional energy of the photon for electrons in the PEM which pass all of the selection cuts. Photons emitted at angles larger than 0.4 radians are outside the $R = 0.4$ isolation cone and have no effect on the electron measurement. Photons emitted at angles less than 0.4 radians, but having energies less than 10% of the electron's energy will also pass the isolation cut. Photons having energies larger than 10% of the electron energy must be emitted closely enough to the electron that the clustering routine will see only one electromagnetic cluster. Furthermore, the photon's energy must be low enough or its angle small enough that it pass the shower shape cuts. In general, as the photon's energy increases, the angle must decrease in order for the electron to pass the electron quality cuts. In the central region, the electron must also pass an E/p cut of 1.5. The photon energy, then, can never be greater than half of the electron's energy. The forbidden regions for photon emission in energy–angle space are shown in Figure 6.8. Only a few (less than 6% for $k_0 = 0.01$) of the 3–body events are excluded by the photon

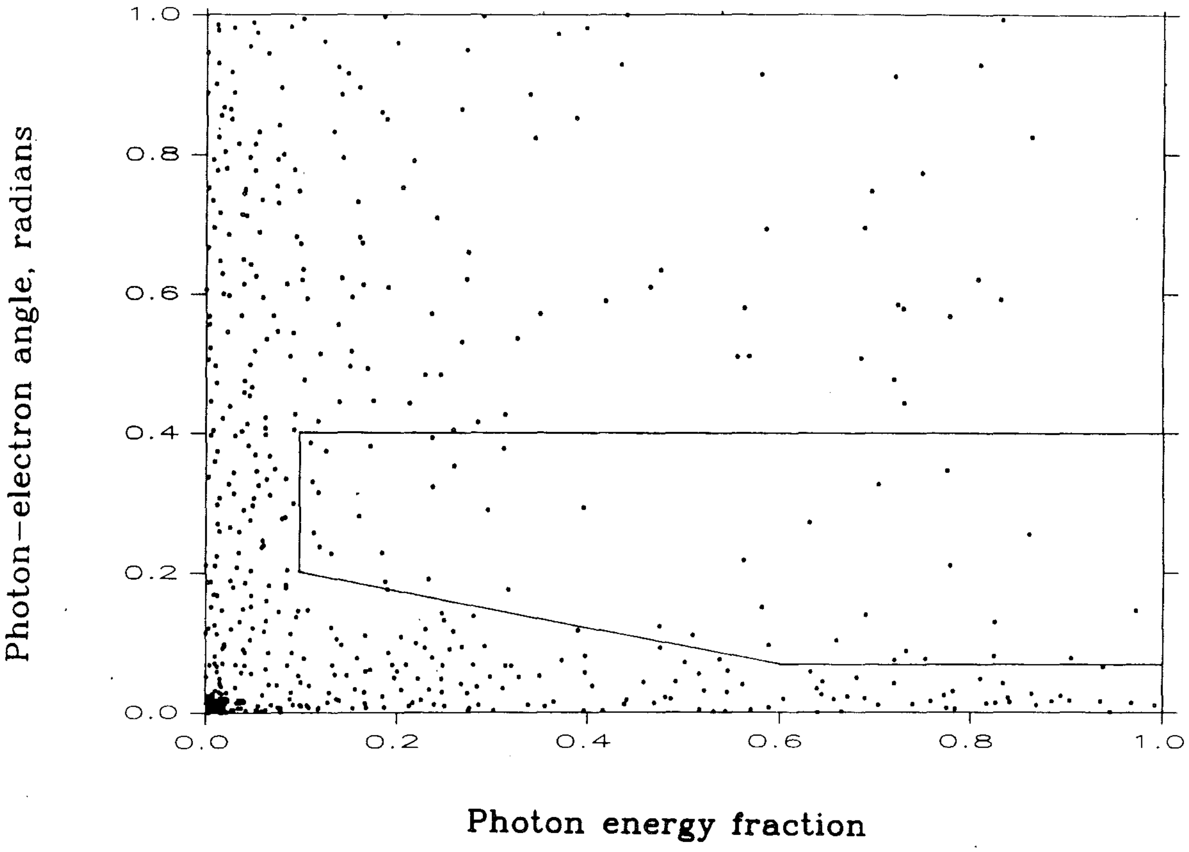

Figure 6.8: Photon angle versus fractional momentum of the photon for simulated electrons which satisfy the electron quality requirements.

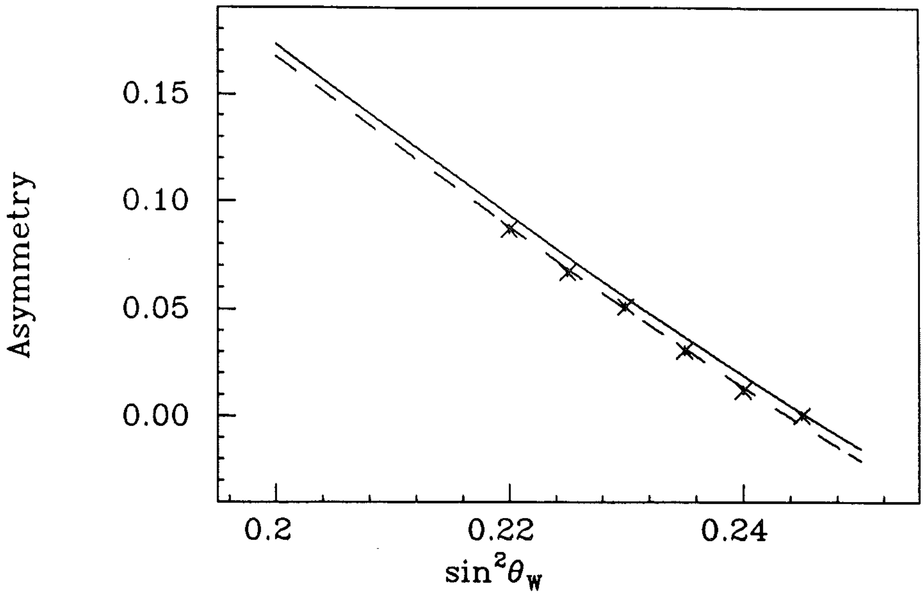

Figure 6.9: Asymmetry as a function of $\sin^2\theta_W$ after QED corrections.

simulation cuts.

The fast simulation of 3–body decays proceeds in the same fashion as the 2–body simulation, but with two extra steps: (1) if the photon is in the forbidden region of energy–angle space, the event is rejected, and (2) if the photon is within ±1 calorimeter η segment of the electron in the CEM calorimeter, and within ±1 calorimeter η segment and ±1 calorimeter ϕ segment of the electron in the gas calorimeters, the photon and electron 4–vectors are summed to simulate the measured "electron" 4–vector.

6.2.3 QED Results

The radiative Monte Carlo is used to calculate the forward–backward asymmetry for various values of $\sin^2\theta_W$, assuming $k_0 = 0.01$. The results of these calculations are shown in Figure 6.9. The solid line shows the lowest order prediction for the asymmetry, assuming EHLQ 1 distribution functions, and the data points are the result of the QED Monte Carlo.

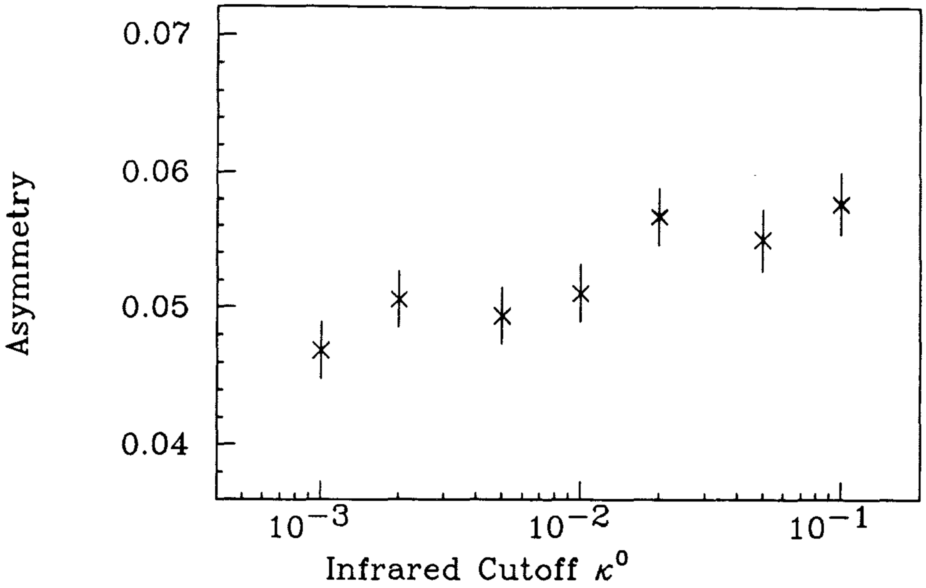

Figure 6.10: Forward–backward asymmetry as a function of the infrared cutoff, k_0.

The effect of the higher order QED diagrams is to reduce the observed asymmetry by a small amount, independent of $\sin^2\theta_W$. A fit to the Monte Carlo data yields the result

$$A_{\mathrm{FB}}|_{Measured} = A_{\mathrm{FB}}|_{Born} - 0.50\%. \tag{6.7}$$

The fit is indicated by the dashed curve in Figure 6.9. After removing the QED contribution to the asymmetry from the measured asymmetry, one arrives at the QED corrected results $A_{\mathrm{FB}}|_{Born} = 5.7\%$ and $\sin^2\theta_W = 0.230$.

The size of the QED corrections depends on the value of k_0, as discussed above. The value chosen for k_0, 0.01, is representative of the resolution of the detector and of various threshold cuts in the data collection and analysis procedures, but there is considerable latitude in the choice of k_0. The theoretical uncertainty on the QED contribution to the asymmetry associated with k_0 is estimated using the radiative Monte Carlo. The forward–backward asymmetry is calculated at $\sin^2\theta_W = 0.230$ using various values of k_0. Figure 6.10 shows the calculated asymmetry versus k_0. The theoretical uncertainty is chosen to be half the total spread in A_{FB}. This gives an uncertainty of 0.0054 for the QED contribution to A_{FB} and 0.0014 for the correction to $\sin^2\theta_W$.

6.3 Weak Corrections

The order α^3 weak corrections to $q\bar{q} \rightarrow e^+e^-$ are shown in groups VII, VIII, IX, XI and XIII of Figure 6.2. These include the box and vertex diagrams having additional weak bosons as well as the loop corrections to the photon and Z^0 propagators. To order α^3, the weak corrected cross section has contributions from the lowest order diagrams and from the interference between the lowest order diagrams and the diagrams including an extra weak boson or a propagator loop. The effect of the loop corrections to the propagators can be absorbed into a renormalization of the photon and Z^0 couplings to fermions which leaves the asymmetry unchanged. The weak vertex corrections have both vector and axial vector components, and, along with the box diagrams, contribute to the measured asymmetry. Unlike the QED corrections, though, the renormalization of the Z^0 couplings is of more interest than the (small) changes in the asymmetry from the additional vertex and box contributions. A renormalization of the Z^0 couplings to fermions implies a renormalization of $\sin^2\theta_W$, in which case both the value of $\sin^2\theta_W$ and its precise definition may change.

In order to perform meaningful calculations of the weak corrections, one must choose a renormalization scheme and a definition for $\sin^2\theta_W$. For the asymmetry analysis, the on–shell renormalization scheme first proposed by Ross and Taylor [40] and documented in Reference [41] is used. In this renormalization scheme $\sin^2\theta_W$ is not an independent parameter, but is most naturally defined, to all orders in perturbation theory, by the Marciano–Sirlin [42] definition of Equation 6.1:

$$\sin^2\theta_W|_{Sirlin} \equiv 1 - \frac{M_W^2}{M_Z^2}.$$

This is not the most convenient definition of $\sin^2\theta_W$ for an analysis of most Z^0 data. The W mass has a rather strong (quadratic) dependence on the mass of the top quark, due to

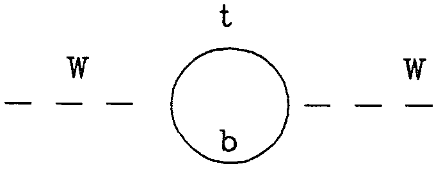

Figure 6.11: Top quark–bottom quark loop contribution to the W self energy.

the top quark–bottom quark loop contribution to the W self energy shown in Figure 6.11, while the Z^0 mass (and other Z^0 observables) depend only weakly on the top mass. When determining $\sin^2\theta_W|_{Sirlin}$ from one of the Z^0 observables, one must incorporate the top quark mass dependence of M_W into the calculation. As a result, $\sin^2\theta_W|_{Sirlin}$ determined from Z^0 observables will have a quadratic dependence on the top quark mass.

Many of the previous experimental measurements of $\sin^2\theta_W$ have been analyzed using the Marciano–Sirlin definition $\sin^2\theta_W|_{Sirlin}$ [17], so for purposes of comparison with these results the Marciano–Sirlin form of $\sin^2\theta_W$ is calculated from the measured forward–backward asymmetry. This is particularly convenient for comparison with the recent direct measurements of $1 - M_W^2/M_Z^2$ made by the CDF and UA2 collaborations.

The electroweak calculations of Reference [41] assume a minimal Higgs structure, with standard couplings and two Higgs doublet fields. The loop corrections to the propagators have a weak (logarithmic) dependence on the mass of the Higgs boson in addition to their dependence on the top quark mass. All calculations, unless otherwise stated, assume a Higgs mass of 100 GeV. The dependence of the final result on the mass of the Higgs boson is shown explicitly below.

The order α^3 weak cross section is calculated in Reference [41] for $e^+e^- \rightarrow f\bar{f}$. As with the virtual QED diagrams, the matrix elements for the weak diagrams are invariant under time reversal, and so the results of [41] can be used directly to calculate the weak corrected cross section for $q\bar{q} \rightarrow e^+e^-$. The electroweak calculations of Reference [41] use the Marciano–Sirlin definition of $\sin^2\theta_W$; unless otherwise noted, the Marciano–Sirlin definition of $\sin^2\theta_W$ is assumed in all the equations given below.

It is difficult to calculate the weak corrections to the asymmetry independent of the renormalization effects of the propagator loops. An iterative procedure is used to calculate the value of $\sin^2\theta_W|_{Sirlin}$ as a function of the mass of the top quark, including both the renormalization effects of the propagator loops and the contributions to the asymmetry from the vertex and box diagrams. For each value of the top quark mass, values for $\sin^2\theta_W|_{Sirlin}$ are selected and the order α^3 weak cross section is integrated to find the asymmetry as a function of $\sin^2\theta_W|_{Sirlin}$. The value of $\sin^2\theta_W|_{Sirlin}$ which reproduces the measured asymmetry, after QCD and QED corrections, is found numerically. A plot of $\sin^2\theta_W|_{Sirlin}$ including all weak corrections is shown as a function of the top quark mass in Figure 6.12. The quadratic dependence on the mass of the top quark is evident.

The relative effects of the vertex, box, and propagator contributions to the cross section can be determined by removing the vertex and box contributions and repeating the iterative calculation of $\sin^2\theta_W|_{Sirlin}$. The result of this propagator-only calculation is shown by the solid line in Figure 6.13. For comparison, the result of the full calculation is shown by the dashed line in Figure 6.13. Removing the vertex and box contributions increases the extracted values of $\sin^2\theta_W$ by 0.0012, independent of the top quark mass. The effect of the vertex and box contributions is to increase the asymmetry by approximately 0.29%, independent of the mass of the top quark.

The weak corrections also depend logarithmically on the mass of the Higgs boson. Figure 6.14 shows a plot of $\sin^2\theta_W|_{Sirlin}$ as a function of the top quark mass for Higgs boson masses of 10, 100, and 1000 GeV. The Higgs mass dependence is much smaller than the

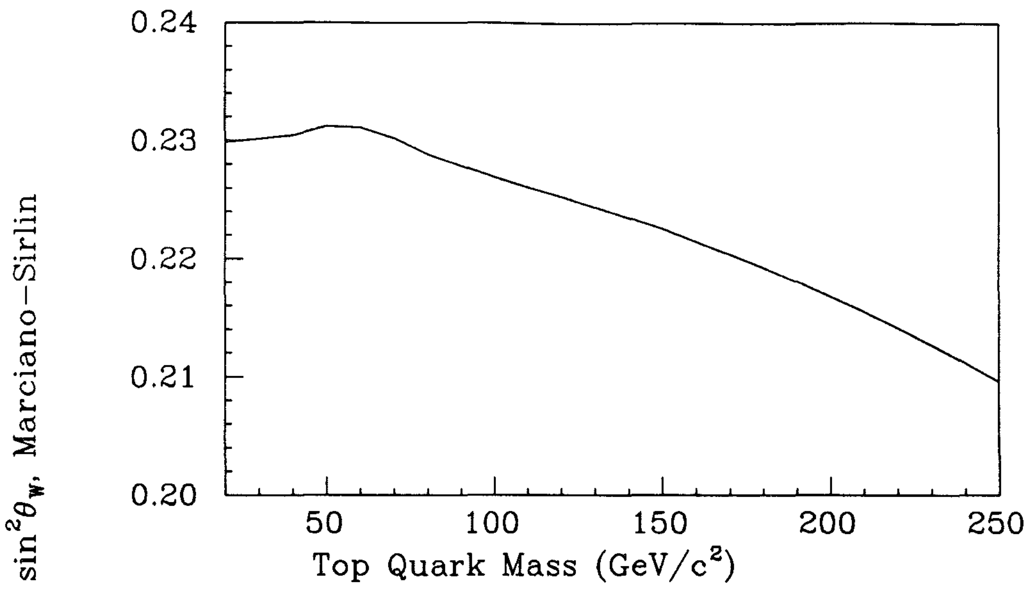

Figure 6.12: $\sin^2\theta_W|_{Sirlin}$ derived from the asymmetry and iterative integrations of the order (α^3) weak cross section.

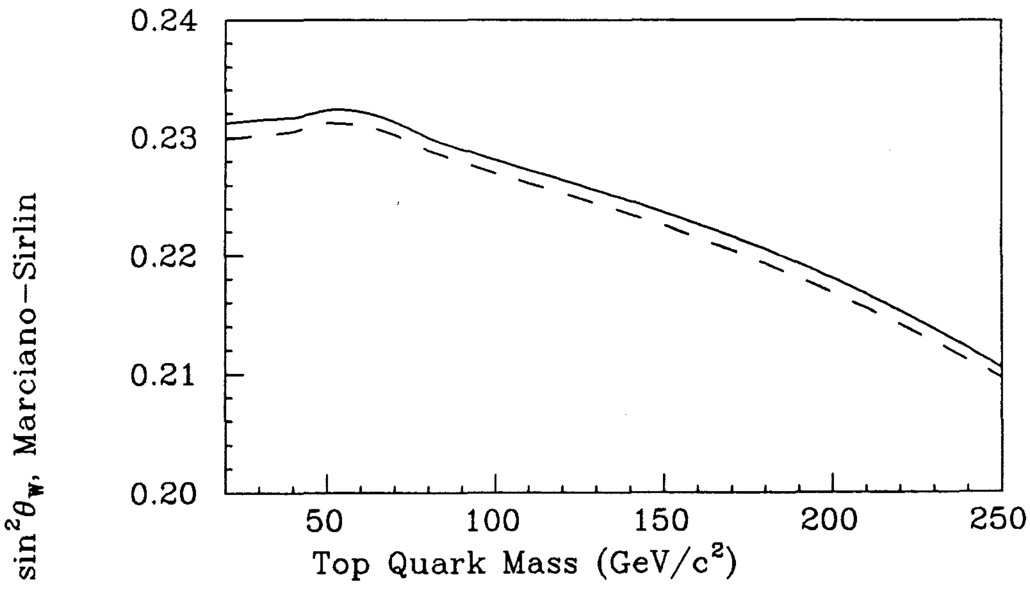

Figure 6.13: $\sin^2\theta_W|_{Sirlin}$ derived from iterative integrations of the order (α^3) weak cross section without (solid) and with (dashed) weak vertex and box contributions.

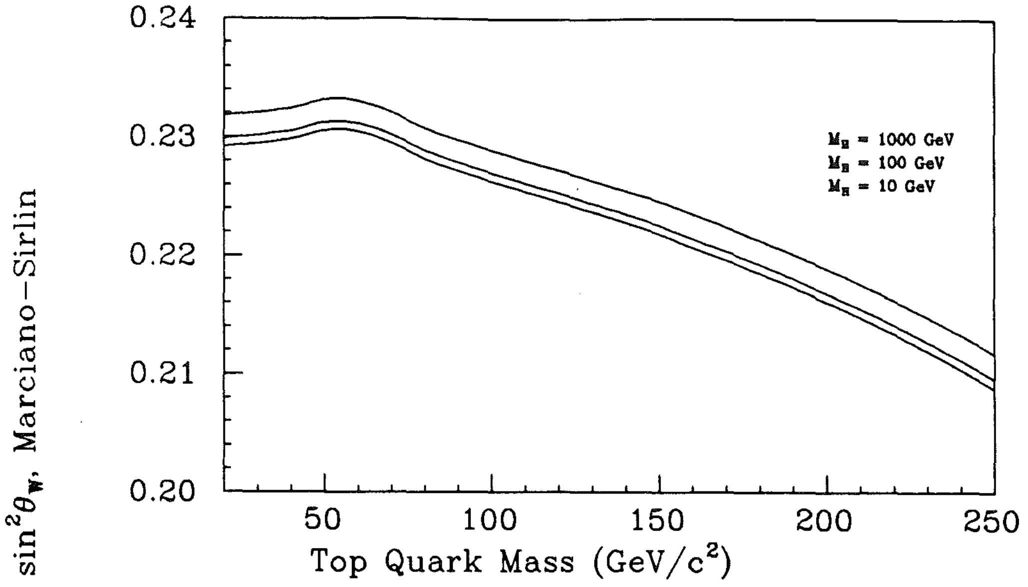

Figure 6.14: $\sin^2\theta_W|_{Sirlin}$ derived from the asymmetry as a function of top quark mass for three different values of Higgs boson mass.

dependence on the top quark mass.

While the Marciano–Sirlin definition of $\sin^2\theta_W$ is useful for comparison with measurements of the W and Z^0 masses, there is a second definition of $\sin^2\theta_W$, based on an effective order α^3 neutral current which is more appropriate for the asymmetry measurement. The mixing angle θ_W describes the mixing of the $SU(2)_L$ and $U(1)_Y$ sectors of the Standard Model, and in particular describes the mixing of the weak isospin and electromagnetic components in the lowest order weak neutral current of Equation 2.12. At higher order, however, other mixing occurs which affects the neutral current. The diagrams in group XIII of Figure 6.2 show photon–Z^0 mixing in the one loop weak radiative corrections. This photon–Z^0 mixing changes the relative contributions of the weak isospin and electromagnetic current couplings to fermions. The effects of the photon–Z^0 mixing terms can be absorbed into an effective neutral current with a suitable redefinition of $\sin^2\theta_W$.

At order α^3 the weak neutral current has contributions from the diagrams shown in

Figure 6.15: Diagrams contributing to the weak neutral current at order α^3.

Figure 6.15. The total neutral current coupling is the sum of the contributions of the diagrams in Figure 6.15, and is given by [41, 50]

$$\begin{aligned} J^{NC} &= \bar{\psi}\gamma^\mu(g_V^f - g_A^f\gamma^5)\psi \;+\; \bar{\psi}\gamma^\mu Q_f\frac{\Pi_{\gamma Z}(s)}{1+\Pi_{\gamma\gamma}(s)}\psi \qquad (6.8) \\ &= \frac{1}{2\cos\theta_W\sin\theta_W}\bar{\psi}\{\gamma^\mu[I_f^3 - 2Q_f\sin^2\theta_W - I_f^3\gamma^\mu\gamma^5\}\psi \\ &\quad + \bar{\psi}\gamma^\mu Q_f\frac{\Pi_{\gamma Z}(s)}{1+\Pi_{\gamma\gamma}(s)}\psi \qquad (6.9) \\ &= \frac{1}{2\cos\theta_W\sin\theta_W}\bar{\psi}\{\gamma^\mu[I_f^3 - 2Q_f(\sin^2\theta_W - \cos\theta_W\sin\theta_W\frac{\Pi_{\gamma Z}(s)}{1+\Pi_{\gamma\gamma}(s)})] \\ &\quad - I_f^3\gamma^\mu\gamma^5\}\psi, \qquad (6.10) \end{aligned}$$

where $\Pi_{\gamma Z}$ and $\Pi_{\gamma\gamma}$ are the renormalized γ-Z and photon self energies, respectively, and the Marciano- Sirlin definition is used for θ_W. Comparing Equations 6.10 and 2.12, one sees that the structure of the lowest order neutral current can be recovered by defining a new mixing angle, $\bar{\theta}_W$, with the relation

$$\begin{aligned} \sin^2\bar{\theta}_W &= \sin^2\theta_W - \cos\theta_W\sin\theta_W\mathrm{Re}\left(\frac{\Pi_{\gamma Z}(s)}{1+\Pi_{\gamma\gamma}(s)}\right) \qquad (6.11) \\ &= \sin^2\theta_W(1-\Delta r'). \qquad (6.12) \end{aligned}$$

The factor $\Delta r'$ incorporates the top quark and Higgs mass dependence of the propagator corrections. Plots of $\Delta r'$ versus top quark mass are shown in Figure 6.16 for Higgs boson

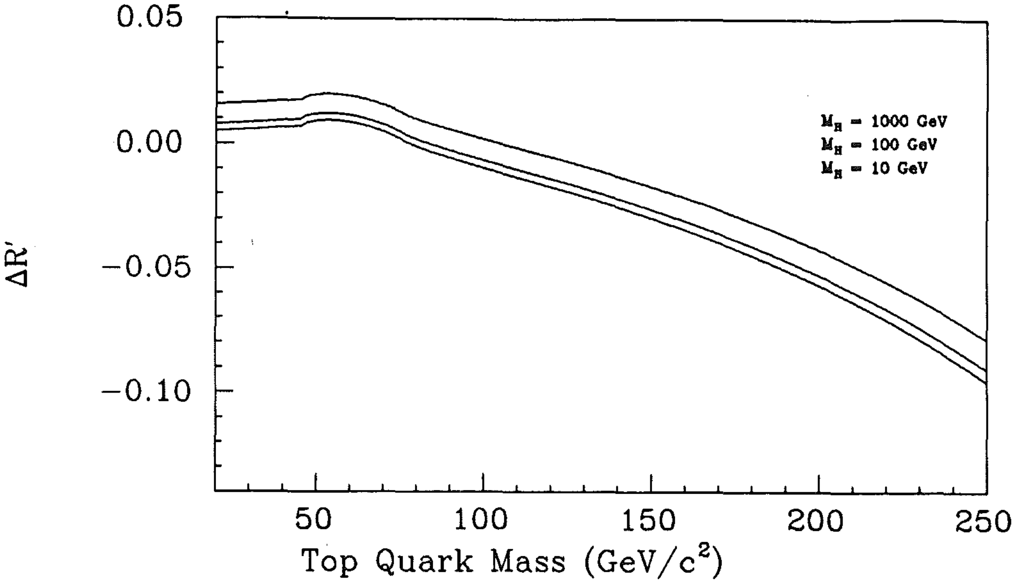

Figure 6.16: The correction factor $\Delta r'$ as a function of top quark mass for three different values of Higgs boson mass.

masses of 10, 100, and 1000 GeV; the top quark and Higgs mass dependence of $\Delta r'$ is similar to that of $\sin^2\theta_W|_{Sirlin}$. Note that the $\sin^2\bar{\theta}_W$ defined by the effective neutral current is equivalent to the $\sin^2\theta_W^*$ defined for effective 4–fermion processes by Kennedy and Lynn [51].

As discussed in Section 2.1, the forward–backward asymmetry is directly related to the spin structure of the weak neutral current. It follows, then, that the $\sin^2\bar{\theta}_W$ defined by the order α^3 effective neutral current is the most natural definition of $\sin^2\theta_W$ for the asymmetry measurement. The value of $\sin^2\theta_W$ extracted from the asymmetry, after correction for QCD, QED, and weak contributions to the asymmetry, is a direct measurement of $\sin^2\bar{\theta}_W$ and yields $\sin^2\bar{\theta}_W = 0.228$. The top quark and Higgs mass dependence of $\sin^2\bar{\theta}_W$ can be investigated using the relation of Equation 6.12, the values of $\sin^2\theta_W|_{Sirlin}$ shown in Figure 6.14, and the calculated values of $\Delta r'$ shown in Figure 6.16. Figure 6.17 shows values for $\sin^2\bar{\theta}_W$ calculated using Equation 6.12 as a function of the top quark mass for 3

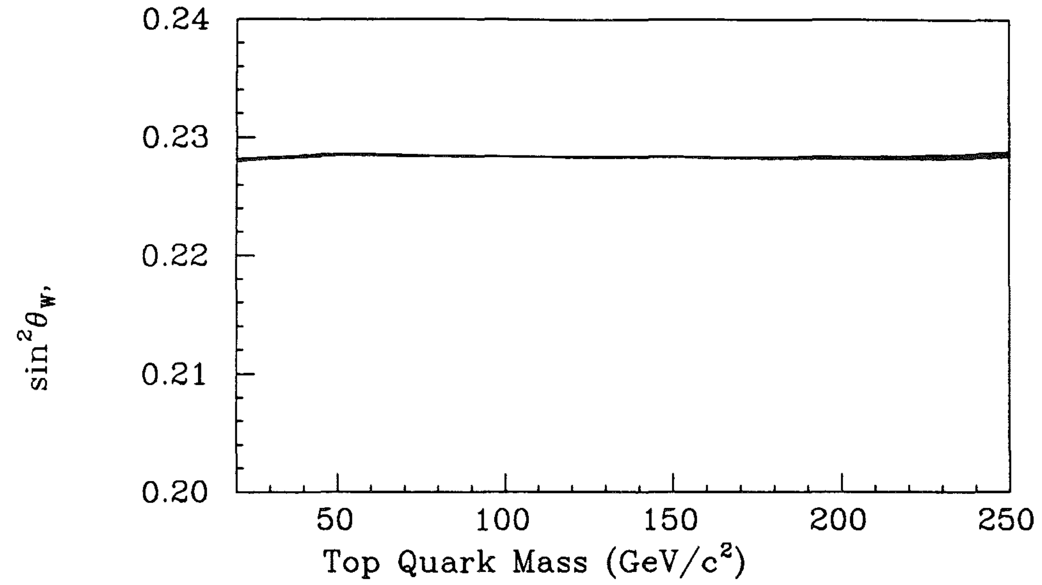

Figure 6.17: $\sin^2\bar{\theta}_W$ derived from the asymmetry as a function of top quark mass for three different values of Higgs boson mass.

different values of the Higgs boson mass. The value of $\sin^2\bar{\theta}_W$ extracted from the asymmetry is nearly independent of the masses of the top quark and the Higgs boson.

Chapter 7

Summary of Results

The forward–backward asymmetry in $p\bar{p} \rightarrow Z^0 \rightarrow e^+e^-$ events is measured to be $(5.2 \pm 5.9\,(\mathrm{stat}) \pm 0.4\,(\mathrm{sys}))\%$, after correcting for a small background contribution and for smearing due to QCD effects. The value $\sin^2 \bar{\theta}_W = 0.228^{+0.017}_{-0.015}\,(\mathrm{stat}) \pm 0.002\,(\mathrm{sys})$ is extracted from the measured asymmetry, and includes QCD, QED and weak radiative corrections. The quoted systematic uncertainty on $\sin^2 \bar{\theta}_W$ includes a theoretical uncertainty from the QED corrections as well as systematic uncertainties related to the asymmetry measurement. This measurement of $\sin^2 \bar{\theta}_W$ is in good agreement with the values $\sin^2 \bar{\theta}_W = 0.2291 \pm 0.0040$ [52] and $\sin^2 \bar{\theta}_W = 0.230 \pm 0.006$ [53] measured from the mass and partial width of the Z^0 by the ALEPH and L3 collaborations, respectively, and with the value $\sin^2 \theta_W = 0.24^{+0.05}_{-0.04}$ measured from the asymmetry in 33 selected dilepton events by the UA1 collaboration [54].

For comparison with other experimental results, the Marciano–Sirlin definition of $\sin^2 \theta_W$ is adopted, where

$$\sin^2 \theta_W|_{Sirlin} = 1 - \frac{M_W^2}{M_Z^2}. \tag{7.1}$$

Figure 7.1 shows $\sin^2 \theta_W|_{Sirlin}$ as derived from the asymmetry measurement as a function of the top quark mass (assuming the mass of the Higgs boson is 100 GeV). The dashed lines show the combined statistical and systematic uncertainties on the measurement. Also shown in Figure 7.1 are the values $1 - M_W^2/M_Z^2 = 0.232 \pm 0.006(\mathrm{stat}) \pm 0.005(\mathrm{sys})$ measured

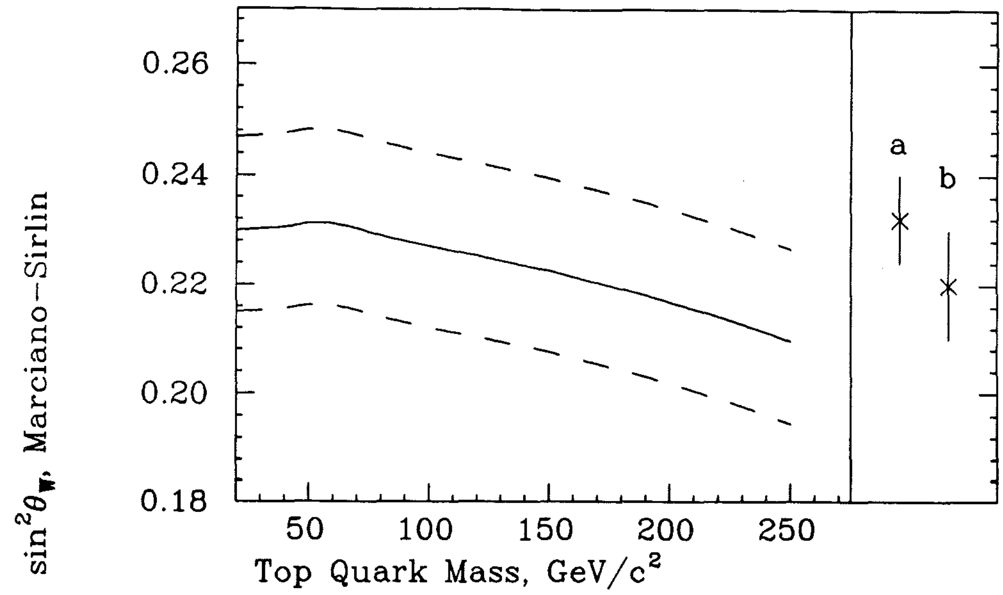

Figure 7.1: Central value and uncertainties on $\sin^2\theta_W|_{Sirlin}$ derived from the asymmetry. At right are values for $1 - M_W^2/M_Z^2$ from CDF (a) and UA2 (b).

directly from the $W^\pm$ mass measured by CDF [55] and the average LEP Z^0 mass [25], and $1 - M_W^2/M_Z^2 = 0.220 \pm 0.009(\text{stat}) \pm 0.005(\text{sys})$ measured by the UA2 collaboration [56]. Figure 7.2 shows the allowed regions (at the 90% confidence level) in the $\sin^2\theta_W|_{Sirlin}$–top quark mass plane from a comprehensive analysis of previous weak neutral current measurements [17]. The $\sin^2\theta_W|_{Sirlin}$ values extracted from the forward–backward asymmetry and shown in Figure 7.1 are consistent with current measurements of $1 - M_W^2/M_Z^2$ and with previous neutral current measurements over a broad range of top quark masses.

The total uncertainty on the asymmetry measurements is dominated by the statistical uncertainty. In the next five years, CDF is expected to increase its total integrated luminosity by a factor of 25 or more. This will be a sufficient amount of data to determine $\sin^2\theta_W$ within a statistical uncertainty of 0.003. This will provide a measurement of $\sin^2\theta_W$ competitive with that derived from the W and Z^0 masses, which has a larger systematic uncertainty than the asymmetry measurement. If the top quark is not discovered in the next

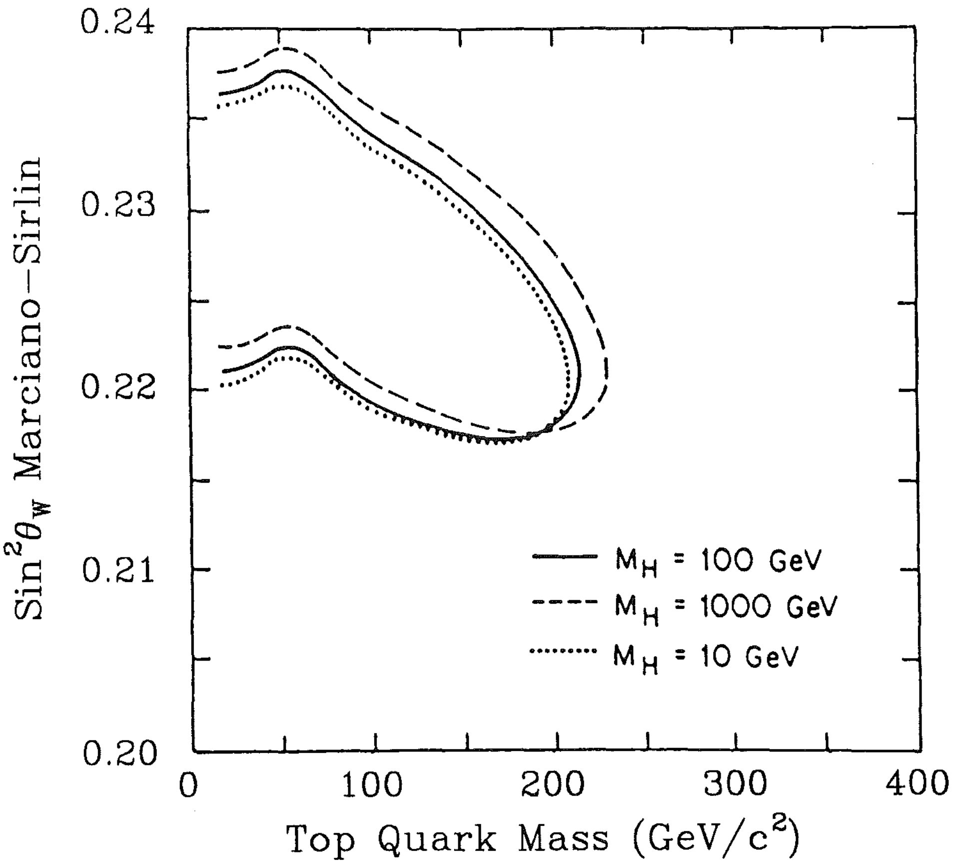

Figure 7.2: Allowed regions (90% confidence level) in the $\sin^2\theta_W|_{Sirlin}$–m_t plane. From the comprehensive analysis of neutral current measurements in Reference [17].

five years, then precision electroweak measurements performed at CDF and other experiments should provide an indirect measurement of the mass of the top quark by measuring its effect on higher order contributions.

Appendix A

Explicit Formulas for the Radiative Corrections

This appendix collects all the formulas used in the radiative corrections to the process $q\bar{q} \rightarrow e^+e^-(\gamma)$. These results and equations have been culled from several theoretical papers, and represent a distillation of the work of many other authors.

The on-shell renormalization scheme first proposed by Ross and Taylor [40] is used. This renormalization scheme uses the fermion masses, α, M_W, M_Z, and M_{Higgs} as input parameters, and assumes a standard Higgs sector with two complex Higgs doublet fields. As mentioned in Chapter 6, $\sin^2\theta_W$ is not an independent parameter in this renormalization scheme, but is most naturally defined in terms of the W and Z^0 masses by

$$\sin^2\theta_W|_{Sirlin} \equiv 1 - \frac{M_W^2}{M_Z^2}.$$

Unless noted otherwise, this Marciano–Sirlin [42] definition of $\sin^2\theta_W$ is assumed in all the equations given below.

One of the advantages of the on–shell renormalization scheme is that the QED contributions to $q\bar{q} \rightarrow e^+e^-(\gamma)$ can be separated from the weak contributions and treated separately. At order α^3, then, the cross section for $q\bar{q} \rightarrow e^+e^-(\gamma)$ can be described as the sum of the lowest order cross section and the QED and weak corrections to the cross section:

$$\frac{d\sigma}{d\Omega} = \frac{d\sigma^0}{d\Omega} + \frac{d\sigma^{QED}}{d\Omega} + \frac{d\sigma^{Weak}}{d\Omega}. \tag{A.1}$$

Below are given explicit formulas for the QED and weak corrections to the cross section.

A.1 QED Contributions to the Cross Section

The order α^3 QED contributions to $q\bar{q} \rightarrow e^+e^-(\gamma)$ are shown in groups III, IV, V, VI, and IX of Figure 6.2. They consist of all the graphs having an additional virtual or real photon. The fermion loop correction to the photon propagator is excluded from the QED corrections, and is included with the contributions of the other boson propagators. As discussed in Chapter 6, the QED corrections to the cross section include the interference between the lowest order and virtual diagrams and the contributions from the bremsstrahlung diagrams. The bremsstrahlung contributions can be divided into a "soft" part and a "hard" part by an infrared cutoff k_0 in the fraction of a fermion's energy carried off by a bremsstrahlung photon. The soft bremsstrahlung contribution is calculated analytically and added to the virtual QED corrections, while the hard bremsstrahlung contribution to the cross section is calculated using a Monte Carlo technique.

The virtual and soft bremsstrahlung corrections are taken from the calculations of Reference [14], unless otherwise noted. The calculations in Reference [14] are for the process $e^+e^- \rightarrow f\bar{f}(\gamma)$ at LEP and SLC. The results of these calculations are time reversed to get predictions for $q\bar{q} \rightarrow e^+e^-(\gamma)$. The matrix elements for the virtual diagrams are invariant under time reversal, and so the results in Reference [14] can be applied directly. The soft bremsstrahlung diagrams differentiate between initial and final state radiation, however, and are not invariant under time reversal. The soft initial state bremsstrahlung corrections for $e^+e^- \rightarrow f\bar{f}(\gamma)$ at LEP and SLC include terms of the form given in Equation 6.5:

$$\frac{1}{M^2 - (s - 4E\Delta E)},$$

where $M^2 = M_Z^2 - iM_Z\Gamma_Z$, E is the energy of the electron beams in the accelerator, ΔE is the energy of a photon from initial state bremsstrahlung, and s is the square of the center of mass energy of the machine. The term $(s - 4E\Delta E)$ is interpreted as the square of the effective center of mass collision energy of the interaction after initial state bremsstrahlung. As explained in Chapter 6, the "prescription" for converting these terms to a form usable for $q\bar{q} \to e^+e^-(\gamma)$ interactions is to interpret E as the energy of the outgoing electrons in the center of mass frame, ΔE as the energy of a photon from final state bremsstrahlung, and s as the square of the dielectron invariant mass. The square of the effective center of mass collision energy of the interaction before final state bremsstrahlung is then $(s + 4E\Delta E)$. To convert the $e^+e^- \to f\bar{f}(\gamma)$ calculations to forms which are applicable to $p\bar{p}$ interactions, one must change the sign of the ΔE term in the bremsstrahlung coefficients and change the interpretation of s.

The cross section for $q\bar{q} \to e^+e^-(\gamma)$, including the lowest order, virtual, and soft bremsstrahlung QED corrections is given by

$$\frac{d\sigma}{d\Omega} = \frac{\alpha^2}{4s}(\sigma^\gamma + \sigma^{\gamma Z} + \sigma^Z), \tag{A.2}$$

where the QED corrected photon, interference, and Z^0 cross sections σ^γ, $\sigma^{\gamma Z}$, and σ^Z are given by

$$\sigma^\gamma = \sigma_0^\gamma C_{IR}^\gamma \left[1 + C_s + \frac{\alpha}{\pi} Q_e Q_f \left(X + V_1^\gamma + A_1^\gamma \frac{2\cos\hat{\theta}}{1 + \cos^2\hat{\theta}}\right)\right] \tag{A.3}$$

$$\sigma^{\gamma Z} = \sigma_0^{\gamma Z} C_{IR}^{\gamma Z} \left[1 + C_s + \frac{\alpha}{\pi} Q_e Q_f \left(X + \frac{V_1^\gamma + V_1^{\gamma Z}}{2} + \frac{A_1^\gamma + A_1^{\gamma Z}}{2} \frac{\sigma_5^{\gamma Z}}{\sigma_0^{\gamma Z}}\right)\right] \tag{A.4}$$

$$\begin{aligned} \sigma^Z = {} & \sigma_0^Z C_{IR}^Z \Bigg\{ 1 + C_s - \frac{\alpha}{\pi} Q_e Q_f \left(X + V_1^{\gamma Z} + A_1^{\gamma Z} \frac{\sigma_5^Z}{\sigma_0^Z}\right) \\ & - \alpha Q_e Q_f \frac{M_Z \Gamma_Z}{s - M_Z^2} \left[(V_2^\gamma - V_2^{\gamma Z}) \frac{\sigma_0^{\gamma Z}}{\sigma_0^Z} + (A_2^\gamma - A_2^{\gamma Z}) \frac{\sigma_5^{\gamma Z}}{\sigma_0^Z}\right] \Bigg\}. \end{aligned} \tag{A.5}$$

The lowest order cross sections σ_0^γ, $\sigma_0^{\gamma Z}$, and σ_0^Z are given by

$$\begin{aligned}
\sigma_0^\gamma &= Q_e^2 Q_f^2 (1+\cos^2\hat{\theta}) && \text{(A.6)}\\
\sigma_0^{\gamma Z} &= 2Q_e Q_f \mathrm{Re}\chi_Z [g_V^e g_V^f (1+\cos^2\hat{\theta}) + 2g_A^e g_A^f \cos\hat{\theta}] && \text{(A.7)}\\
\sigma_0^Z &= |\chi_Z|^2 [((g_V^e)^2 + (g_A^e)^2)((g_V^f)^2 + (g_A^f)^2)(1+\cos^2\hat{\theta}) + 8 g_V^e g_A^e g_V^f g_A^f \cos\hat{\theta}], && \text{(A.8)}
\end{aligned}$$

where the propagator χ_Z is given by

$$\chi_Z = \frac{s}{s - M_Z^2 + iM_Z\Gamma_Z}. \tag{A.9}$$

The cross sections σ_5^γ, $\sigma_5^{\gamma Z}$, and σ_5^Z are given by the lowest order cross sections with the $(1+\cos^2\hat{\theta})$ and $2\cos\hat{\theta}$ terms interchanged, *i.e.*

$$\sigma_5^{\gamma,\gamma Z,Z} = \sigma_0^{\gamma,\gamma Z,Z}((1+\cos^2\hat{\theta}) \leftrightarrow 2\cos\hat{\theta}). \tag{A.10}$$

The terms C_{IR}^γ, $C_{IR}^{\gamma Z}$, and C_{IR}^Z are bremsstrahlung terms. These terms account for multiphoton emission by exponentiating leading logarithms as described in Reference [45]. These bremsstrahlung terms are given by

$$C_{IR}^\gamma = \left(\frac{\Delta E}{E}\right)^{(2\alpha/\pi)(Q_e^2\beta_e + Q_e Q_f \beta_{int} + Q_f^2 \beta_f)} \tag{A.11}$$

$$\begin{aligned}
C_{IR}^{\gamma Z} &= \mathrm{Re}\left\{\left(1 + i\frac{M_Z\Gamma_Z}{M_Z^2 - s}\right)\left(\frac{\Delta E}{E}\frac{1}{1 + s(\Delta E/E)/(s-M^2)}\right)^{(2\alpha/\pi)Q_e^2\beta_e}\right.\\
&\quad \times \left.\left(\frac{\Delta E}{E}\frac{1}{M^2/s - 1 - (\Delta E/E)}\right)^{(\alpha/\pi)Q_e Q_f \beta_{int}}\right\}\left(\frac{\Delta E}{E}\right)^{(\alpha/\pi)(2Q_f^2\beta_f + Q_e Q_f \beta_{int})} && \text{(A.12)}
\end{aligned}$$

$$\begin{aligned}
C_{IR}^Z &= \left|\frac{\Delta E}{E}\frac{1}{1 + s(\Delta E/E)/(s-M^2)}\right|^{(2\alpha/\pi)Q_e^2\beta_e}\left|\frac{\Delta E}{E}\frac{1}{1 + (\Delta E/E) - M^2/s}\right|^{(2\alpha/\pi)Q_e Q_f \beta_{int}}\\
&\quad \times \left(\frac{\Delta E}{E}\right)^{(2\alpha/\pi)Q_f^2\beta_f}\left[1 + \frac{2\alpha}{\pi}\beta_e\frac{s - M_Z^2}{M_Z\Gamma_Z}(\Phi - \Phi_Z)\right], && \text{(A.13)}
\end{aligned}$$

where the complex Z^0 mass M^2 is

$$M^2 = M_Z^2 - iM_Z\Gamma_Z. \tag{A.14}$$

The β coefficients are defined as follows:

$$\beta_e = \ln(s/m_e^2) - 1 \tag{A.15}$$

$$\beta_f = \ln(s/m_f^2) - 1 \tag{A.16}$$

$$\beta_{int} = 2\ln(t/u), \tag{A.17}$$

where m_e and m_f are the masses of the outgoing electron and incoming fermion, respectively, and t and u are the Mandelstam variables

$$t = -\frac{s}{2}(1 - \cos\hat{\theta}), \qquad u = -\frac{s}{2}(1 + \cos\hat{\theta}).$$

The Breit-Wigner phases Φ_Z and Φ are given by

$$\Phi_Z = \arctan\left(\frac{M_Z^2 - s}{M_Z\Gamma_Z}\right) \tag{A.18}$$

$$\Phi = \arctan\left(\frac{M_Z^2 - s - s(\Delta E/E)}{M_Z\Gamma_Z}\right). \tag{A.19}$$

These phase angles are responsible for the radiative tail below the Z^0 resonance shown in Figures 6.5 and 6.6. The term C_s collects together vertex correction factors and is

$$C_s = \frac{3\alpha}{2\pi}(Q_e^2\beta_e + Q_f^2\beta_f) + \frac{\alpha}{\pi}(Q_e^2 + Q_f^2)(\tfrac{1}{3}\pi^2 - \tfrac{1}{2}). \tag{A.20}$$

The X term comes from the interference of the soft initial state and final state bremsstrahlung diagrams, and has the form

$$X = \ln^2\left(-\frac{t}{s}\right) - \ln^2\left(-\frac{u}{s}\right) - 2\mathrm{Li}_2\left(-\frac{t}{s}\right) + 2\mathrm{Li}_2\left(-\frac{u}{s}\right). \tag{A.21}$$

where the dilogarithm Li_2 is defined by the integral

$$\mathrm{Li}_2(z) = -\int_0^1 dx \frac{\ln(1 - xz)}{x}, \tag{A.22}$$

and can be quickly calculated using the following series expansion [57]:

$$\mathrm{Li}_2(z) = \sum_{n=0}^{\infty} B_n \frac{-\ln^{n+1}(1 - z)}{(n + 1)!}, \tag{A.23}$$

where the coefficients B_n are the so-called Bernoulli numbers. Summing the first 18 coefficients of the series gives sufficient numerical accuracy for almost any application. The $V^{\gamma,\gamma Z}$ and $A^{\gamma,\gamma Z}$ terms come from the two photon and photon Z^0 box diagrams. The two photon box contributions are

$$\begin{aligned}
V_1^{\gamma} &= (1+c)^{-1}\ln\frac{1-c}{2} - (1-c)^{-1}\ln\frac{1+c}{2} \\
&\quad -c(1+c)^{-2}\ln^2\frac{1-c}{2} - c(1-c)^{-2}\ln^2\frac{1+c}{2} && \text{(A.24)} \\
V_2^{\gamma} &= -\frac{c}{(1-c^2)} + \ln\frac{1-c}{1+c} - c(1+c)^{-2}\ln\frac{1-c}{2} \\
&\quad -c(1-c)^{-2}\ln\frac{1+c}{2} && \text{(A.25)} \\
A_1^{\gamma} &= (1+c)^{-1}\ln\frac{1-c}{2} + (1-c)^{-1}\ln\frac{1+c}{2} \\
&\quad -c(1+c)^{-2}\ln^2\frac{1-c}{2} + c(1-c)^{-2}\ln^2\frac{1+c}{2} && \text{(A.26)} \\
A_2^{\gamma} &= (1-c^2)^{-1} - c(1+c)^{-2}\ln\frac{1-c}{2} + c(1-c)^{-2}\ln\frac{1+c}{2}, && \text{(A.27)}
\end{aligned}$$

where $c = \cos\hat{\theta}$. The photon Z^0 box contributions have a compact form taken from Reference [41],

$$\begin{aligned}
V^{\gamma Z} &= V_1^{\gamma Z} + 2\pi i V_2^{\gamma Z} && \text{(A.28)} \\
A^{\gamma Z} &= A_1^{\gamma Z} + 2\pi i A_2^{\gamma Z}, && \text{(A.29)}
\end{aligned}$$

with

$$\begin{aligned}
V^{\gamma Z} &= V(s,t) - V(s,u) && \text{(A.30)} \\
A^{\gamma Z} &= A(s,t) + A(s,u) && \text{(A.31)}
\end{aligned}$$

where

$$\begin{aligned}
A(s,t) &= \frac{s-M^2}{s+t}\left\{\ln\frac{t}{s-M^2} + \frac{M^2}{s}\ln\left(1-\frac{s}{M^2}\right)\right. \\
&\quad \left. + \frac{s+2t+M^2}{s+t}\left[\ln -\frac{t}{M^2}\ln\frac{M^2-s}{M^2+t} + \mathrm{Li}_2\left(\frac{s}{M^2}\right) - \mathrm{Li}_2\left(-\frac{t}{M^2}\right)\right]\right\} && \text{(A.32)} \\
V(s,t) &= A(s,t) + 2\mathrm{Li}_2\left(1+\frac{M^2}{t}\right) && \text{(A.33)}
\end{aligned}$$

where the definition $M^2 = M_Z^2 - iM_Z\Gamma_Z$ is used for the complex Z^0 mass.

The bremsstrahlung cross section for $q(p_-)\bar{q}(p_+) \to e^+(q_+)e^-(q_-)\gamma(k)$, exact up to order $(m_e/E)^2$ and $(m_q/E)^2$ terms, is given by [58]

$$\frac{d^5\sigma}{d\Omega_{ee}dq_+^0dq_-^0d\phi_\gamma} = \frac{\alpha^3}{2\pi^2 s}Y \tag{A.34}$$

where

$$\begin{aligned} Y = & -\frac{m_q^2Q_q^2}{2s'^2}\left[A(s')\left(\frac{t^2}{\kappa_-^2}+\frac{t'^2}{k_+^2}\right)+B(s')\left(\frac{u^2}{\kappa_-^2}+\frac{u'^2}{k_+^2}\right)\right] \\ & +\frac{Q_q^2}{4s'\kappa_+\kappa_-}[A(s')(t^2+t'^2)+B(s')(u^2+u'^2)] \\ & -\frac{m_e^2Q_e^2}{2s^2}\left[A(s)\left(\frac{t^2}{\kappa_-'^2}+\frac{t'^2}{\kappa_+'^2}\right)+B(s)\left(\frac{u'^2}{\kappa_-'^2}+\frac{u^2}{\kappa_+'^2}\right)\right] \\ & +\frac{Q_e^2}{4s\kappa_+'\kappa_-'}[A(s)(t^2+t'^2)+B(s)(u^2+u'^2)] \\ & +\frac{Q_qQ_e}{4ss'}\left[\frac{u}{\kappa_+\kappa_-'}+\frac{u'}{\kappa_-\kappa_+'}-\frac{t}{\kappa_+\kappa_+'}-\frac{t'}{\kappa_-\kappa_-'}\right] \\ & \times[C(s,s')(t^2+t'^2)+(D(s,s')(u^2+u'^2)] \\ & +\frac{(s-s')M\Gamma Q_qQ_e}{2\kappa_+\kappa_-\kappa_+'\kappa_-'}\varepsilon_{\mu\nu\rho\sigma}p_+^\mu p_-^\nu q_+^\rho q_-^\sigma \\ & \times[E(s,s')(t^2-t'^2)+(F(s,s')(u^2-u'^2)] \end{aligned} \tag{A.35}$$

where ε is the antisymmetric tensor with $\varepsilon_{0123} = 1$, and the kinematic terms are given by

$$s = (p_+ + p_-)^2 \tag{A.36}$$

$$t = (p_+ - q_+)^2 \tag{A.37}$$

$$u = (p_+ - q_-)^2 \tag{A.38}$$

$$s' = (q_+ + q_-)^2 \tag{A.39}$$

$$t' = (p_- - q_-)^2 \tag{A.40}$$

$$u' = (p_- - q_+)^2 \tag{A.41}$$

$$\kappa_\pm = p_\pm \cdot k \tag{A.42}$$

$$\kappa_\pm' = q_\pm \cdot k\ . \tag{A.43}$$

The coefficients in the bremsstrahlung cross section are given by

$$\begin{aligned}
A(s) &= 1 + 2\mathrm{Re}\chi_Z(s)(g_V^e g_V^q - g_A^e g_A^q) \\
&\quad + |\chi_Z(s)|^2[((g_V^e)^2 + (g_A^e)^2)((g_V^q)^2 + (g_A^q)^2) - 4g_V^e g_A^e g_V^q g_A^q] \qquad \text{(A.44)} \\
B(s) &= 1 + 2\mathrm{Re}\chi_Z(s)(g_V^e g_V^q + g_A^e g_A^q) \\
&\quad + |\chi_Z(s)|^2[((g_V^e)^2 + (g_A^e)^2)((g_V^q)^2 + (g_A^q)^2) + 4g_V^e g_A^e g_V^q g_A^q] \qquad \text{(A.45)} \\
C(s,s') &= 1 + \Big[\mathrm{Re}\chi_Z(s) + \mathrm{Re}\chi_Z(s')\Big](g_V^e g_V^q - g_A^e g_A^q) \\
&\quad + \mathrm{Re}(\chi_Z(s)\chi_Z(s'))[((g_V^e)^2 + (g_A^e)^2)((g_V^q)^2 + (g_A^q)^2) - 4g_V^e g_A^e g_V^q g_A^q] \text{(A.46)} \\
D(s,s') &= 1 + \Big[\mathrm{Re}\chi_Z(s) + \mathrm{Re}\chi_Z(s')\Big](g_V^e g_V^q + g_A^e g_A^q) \\
&\quad + \mathrm{Re}(\chi_Z(s)\chi_Z(s'))[((g_V^e)^2 + (g_A^e)^2)((g_V^q)^2 + (g_A^q)^2) + 4g_V^e g_A^e g_V^q g_A^q] \text{(A.47)} \\
E(s,s') &= \frac{g_V^e g_V^q - g_A^e g_A^q}{2ss'}\left[\frac{|\chi_Z(s')|^2}{s'} - \frac{|\chi_Z(s)|^2}{s}\right]|\chi_Z(s)|^2|\chi_Z(s')|^2(s-s') \\
&\quad \frac{((g_V^e)^2 + (g_A^e)^2)g_V^q g_A^q - ((g_V^q)^2 + (g_A^q)^2)g_V^e g_A^e}{s^2 s'^2} \qquad \text{(A.48)} \\
F(s,s') &= \frac{g_V^e g_V^q + g_A^e g_A^q}{2ss'}\left[\frac{|\chi_Z(s')|^2}{s'} - \frac{|\chi_Z(s)|^2}{s}\right]|\chi_Z(s)|^2|\chi_Z(s')|^2(s-s') \\
&\quad \frac{((g_V^e)^2 + (g_A^e)^2)g_V^q g_A^q + ((g_V^q)^2 + (g_A^q)^2)g_V^e g_A^e}{s^2 s'^2} \qquad \text{(A.49)}
\end{aligned}$$

The first two terms in Equation A.35 correspond to initial state bremsstrahlung, and the second two terms correspond to bremsstrahlung from the final state. The last two terms in Equation A.35 come from the interference between the initial state and final state bremsstrahlung diagrams.

The energy spectrum for bremsstrahlung photons is obtained by integrating Equation A.35, and is naturally divided into initial state, final state, and interference terms,

$$\frac{d\sigma}{dk} = \frac{d\sigma^q}{dk} + \frac{d\sigma^e}{dk} + \frac{d\sigma^i}{dk} \qquad \text{(A.50)}$$

where

$$\begin{aligned}
\frac{d\sigma^q}{dk} &= \sigma_0(s')\frac{\alpha}{\pi}\left(\ln\frac{s}{m_q^2} - 1\right)\left[1 + \left(\frac{s'}{s}\right)^2\right]\frac{1}{k} \qquad \text{(A.51)} \\
\frac{d\sigma^e}{dk} &= \sigma_0(s)\frac{\alpha}{\pi}\left(\ln\frac{s}{m_e^2} - 1 + \ln\frac{s'}{s}\right)\left[1 + \left(\frac{s'}{s}\right)^2\right]\frac{1}{k} \qquad \text{(A.52)}
\end{aligned}$$

$$\frac{d\sigma^i}{dk} = \frac{2\alpha^3}{s}[C(s,s') - D(s,s')]\frac{2E-k}{k} \ . \tag{A.53}$$

The lowest order cross section $\sigma_0(s)$ used in Equations A.51 and A.52 is the differential cross section integrated over Ω:

$$\begin{aligned} \sigma_0(s) &= \int \frac{d\sigma}{d\Omega} d\Omega \\ &= \frac{\alpha^2}{4s}\int (\sigma_0^\gamma + \sigma_0^{\gamma Z} + \sigma_0^Z) \\ &= \frac{4\alpha^2}{3s}(Q_e^2 Q_f^2 + 2Q_e Q_f g_V^e g_V^f \mathrm{Re}\chi_Z \\ &\quad +((g_V^e)^2 + (g_A^e)^2)((g_V^f)^2 + (g_A^f)^2)|\chi_Z|^2) \ . \end{aligned} \tag{A.54}$$

As discussed in Section 6.2.2, the radiative Monte Carlo used for the asymmetry analysis calculates only the contribution of hard final state bremsstrahlung (the third and fourth terms of Equation A.35) to the 3-body cross section. The fraction of events which have a hard final state photon with energy fraction greater than k_0 is determined by integrating the bremsstrahlung photon energy spectrum of Equation A.52 from the cutoff $k = k_0 E$ upward. The fraction of events with a photon with energy fraction larger than k_0 is given by [49]

$$\begin{aligned} \delta_Q^h(k_0) &= \frac{2\alpha}{\pi}\left[\left(\ln\frac{s}{m_e^2} - 1\right)\right. \\ &\quad \times\left(\ln\frac{1}{k_0} - \tfrac{1}{4}(1-k_0)(3-k_0)\right) - \frac{\pi^2}{6} \\ &\quad +\mathrm{Li}_2(k_0) - \tfrac{1}{4}(1-k_0)(3-k_0)\ln(1-k_0) \\ &\quad \left. +\tfrac{1}{8}(1-k_0)(5-k_0)\right] \ . \end{aligned} \tag{A.55}$$

A.2 Weak Contributions to the Cross Section

The cross section for $q\bar{q} \to e^+e^-$, including the lowest order contributions and the weak corrections is given by

$$\frac{d\sigma}{d\Omega} = \frac{\alpha^2}{4s}G_1(s,t)(1+\cos^2\hat{\theta}) + G_3(s,t)\cos\hat{\theta}, \tag{A.56}$$

j	V_j^e	A_j^e	V_j^f	A_j^f	χ_j
1	Q_e	0	Q_f	0	$\chi_1 = \chi_\gamma$
2	g_V^e	g_A^e	g_V^f	g_A^f	$\chi_2 = \chi_Z$
3	Q_e	0	g_V^f	g_A^f	$\chi_3 = \chi_{\gamma Z}$
4	g_V^e	g_A^e	Q_f	0	$\chi_4 = \chi_{\gamma Z}$
5	$F_V^{\gamma e}(s)$	$F_A^{\gamma e}(s)$	Q_f	0	$\chi_5 = \chi_\gamma$
6	Q_e	0	$F_V^{\gamma f}(s)$	$F_A^{\gamma f}(s)$	$\chi_6 = \chi_\gamma$
7	$F_V^{Ze}(s)$	$F_A^{Ze}(s)$	g_V^f	g_A^f	$\chi_7 = \chi_Z$
8	g_V^e	g_A^e	$F_V^{Zf}(s)$	$F_A^{Zf}(s)$	$\chi_8 = \chi_Z$
9	$((g_V^e)^2 + (g_A^e)^2)$	$2g_V^e g_A^e$	$((g_V^f)^2 + (g_A^f)^2)$	$2g_V^f g_A^f$	χ_9
10	$2g_V^e g_A^e$	$((g_V^e)^2 + (g_A^e)^2)$	$2g_V^f g_A^f$	$((g_V^f)^2 + (g_A^f)^2)$	χ_{10}
11	$\frac{1}{2\sin^2\theta_W}$	$\frac{1}{2\sin^2\theta_W}$	$\frac{1}{2\sin^2\theta_W}$	$\frac{1}{2\sin^2\theta_W}$	χ_{11}

Table A.1: Vector and axial vector components and corrected propagators used in the weak corrections to $q\bar{q} \to e^+e^-$.

where

$$G_1(s,t) = \mathrm{Re} \sum_{j,k=1}^{11} (V_j^e V_k^{e*} + A_j^e A_k^{e*})(V_j^f V_k^{f*} + A_j^f A_k^{f*})\chi_j \chi_k^* \tag{A.57}$$

$$G_3(s,t) = \mathrm{Re} \sum_{j,k=1}^{11} (V_j^e A_k^{e*} + A_j^e V_k^{e*})(V_j^f A_k^{f*} + A_j^f V_k^{f*})\chi_j \chi_k^*. \tag{A.58}$$

The vector and axial vector components $V_j^{e,f}$ and $A_j^{e,f}$, and the propagators χ_j are taken from Reference [41] and shown in Table A.1. The electromagnetic vertex factors $F_{V,A}^{\gamma e,\gamma f}$ are given (for charged fermions) by

$$F_V^{\gamma f} = \frac{\alpha}{4\pi}[Q_f((g_V^f)^2 + (g_A^f)^2)\Lambda_2(s, M_Z) + G_L^f] \tag{A.59}$$

$$F_A^{\gamma f} = \frac{\alpha}{4\pi}[Q_f 2 g_V^f g_A^f \Lambda_2(s, M_Z) + G_L^f] \tag{A.60}$$

with

$$G_L^l = -\frac{3}{4s_W^2}\Lambda_3(s, M_W) \tag{A.61}$$

$$G_L^u = -\frac{1}{12s_W^2}\Lambda_2(s, M_W) + \frac{3}{4s_W^2}\Lambda_3(s, M_W) \tag{A.62}$$

$$G_L^d = \frac{1}{6s_W^2}\Lambda_2(s, M_W) - \frac{3}{4s_W^2}\Lambda_3(s, M_W), \tag{A.63}$$

where G_L^l, G_L^u, and G_L^d are for leptons, u-type quarks, and d-type quarks, respectively. The abbreviated notation

$$s_W = \sin\theta_W \qquad c_W = \cos\theta_W \tag{A.64}$$

is used to make the equations more compact. The functions Λ_2 and Λ_3 have the form

$$\begin{aligned}\Lambda_2(s, M) = {} & -\frac{7}{2} - 2w - (2w+3)\ln(w) \\ & +2(1+w)^2\left[\ln(w)\ln\left(\frac{1+w}{w}\right) - \mathrm{Li}_2\left(-\frac{1}{w}\right)\right] \\ & -i\pi\left[3 + 2w - 2(w+1)^2\ln\left(\frac{1+w}{w}\right)\right]\end{aligned} \tag{A.65}$$

$$\begin{aligned}\Lambda_3(s, M) = {} & \frac{5}{6} - \frac{2w}{3} + \frac{2}{3}(2w+1)\sqrt{4w-1}\arctan\frac{1}{\sqrt{4w-1}} \\ & -\frac{8}{3}w(w+2)\left(\arctan\frac{1}{\sqrt{4w-1}}\right)^2\end{aligned} \tag{A.66}$$

where $w = M^2/s$, with $M = M_Z$ or M_W, and $0 < s < 4M_W^2$. The weak neutral current vertex factors $F_{V,A}^{Ze,Zf}$ are given (for charged fermions) by

$$F_V^{Zf} = \frac{\alpha}{4\pi}[g_V^f((g_V^f)^2 + 3(g_A^f)^2)\Lambda_2(s, M_Z) + F_L^f] \tag{A.67}$$

$$F_A^{Zf} = \frac{\alpha}{4\pi}[g_A^f(3(g_V^f)^2 + (g_A^f)^2)\Lambda_2(s, M_Z) + F_L^f] \tag{A.68}$$

with

$$F_L^l = \frac{1}{8s_W^3 c_W}\Lambda_2(s, M_W) - \frac{3c_W}{4s_W^3}\Lambda_3(s, M_W) \tag{A.69}$$

$$F_L^u = -\frac{1-\frac{2}{3}s_W^2}{8s_W^3 c_W}\Lambda_2(s,M_W) + \frac{3c_W}{4s_W^3}\Lambda_3(s,M_W) \tag{A.70}$$

$$F_L^u = -\frac{1-\frac{4}{3}s_W^2}{8s_W^3 c_W}\Lambda_2(s,M_W) - \frac{3c_W}{4s_W^3}\Lambda_3(s,M_W). \tag{A.71}$$

The χ propagators from Table A.1 are defined by

$$\chi_\gamma = \frac{s}{s+\hat{\Sigma}^\gamma(s) - \frac{\hat{\Sigma}^{\gamma z}(s)^2}{s-M_Z^2+\hat{\Sigma}^Z(s)}} \tag{A.72}$$

$$\chi_Z = \frac{s}{s-M_Z^2+\hat{\Sigma}^Z(s) - \frac{\hat{\Sigma}^{\gamma z}(s)^2}{s+\hat{\Sigma}^\gamma(s)}} \tag{A.73}$$

$$\chi_{\gamma Z} = \frac{s\hat{\Sigma}^{\gamma Z}(s)}{[s+\hat{\Sigma}^\gamma(s)][s-M_Z^2+\hat{\Sigma}^Z(s)] - \hat{\Sigma}^{\gamma Z}(s)^2} \tag{A.74}$$

$$\chi_9 = \frac{\alpha}{2\pi}[I(s,t,M_Z) - I(s,u,M_Z)] \tag{A.75}$$

$$\chi_{10} = \frac{\alpha}{2\pi}[I_5(s,t,M_Z) + I_5(s,u,M_Z)] \tag{A.76}$$

$$\chi_{11} = \frac{\alpha}{2\pi}\begin{cases} [I(s,t,M_W) + I_5(s,t,M_W)] & \text{for } I_3^f = -\frac{1}{2} \text{ fermions} \\ [-I(s,u,M_W) + I_5(s,u,M_W)] & \text{for } I_3^f = +\frac{1}{2} \text{ fermions} \end{cases} \tag{A.77}$$

The functions I and I_5 are

$$\begin{aligned} I_5(s,t,M) = \frac{s}{s+t}\Bigg\{ & \frac{s+2t+2M^2}{2(s+t)}\left[\mathrm{Li}_2\left(1+\frac{t}{M^2}\right) - \frac{\pi^2}{6} - \ln^2\left(-\frac{y_1}{y_2}\right)\right] \\ & +\frac{1}{2}\ln\left(-\frac{t}{M^2}\right) + \frac{y_2-y_1}{2}\ln\left(-\frac{y_1}{y_2}\right) \\ & +\frac{s+2t-4M^2t/s+2M^4/t-2M^4/s}{2(s+t)(x_2-x_1)}\cdot J(s,t,M)\Bigg\} \end{aligned} \tag{A.78}$$

$$I(s,t,M) = I_5(s,t,M) + 2\ln^2\left(-\frac{y_1}{y_2}\right) + \frac{2}{x_1 - x_2} \cdot J(s,t,M) \tag{A.79}$$

with

$$J(s,t,M) = \mathrm{Li}_2\frac{x_1}{x_1 - y_1} + \mathrm{Li}_2\frac{x_1}{x_1 - y_2} - \mathrm{Li}_2\frac{x_2}{x_2 - y_1} - \mathrm{Li}_2\frac{x_2}{x_2 - y_2} \tag{A.80}$$

$$x_{1,2} = \frac{1}{2}\left(1 \pm \sqrt{1 - \frac{4M^2}{s}\left(1 + \frac{M^2}{t}\right)}\right) \tag{A.81}$$

$$y_{1,2} = \frac{1}{2}\left(1 \pm \sqrt{1 - \frac{4M^2}{s}}\right) \tag{A.82}$$

The renormalized vector boson self energies are given by

$$\hat{\Sigma}^{\gamma}(s) = \Sigma^{\gamma}(s) + s\delta Z_2^{\gamma} \tag{A.83}$$

$$\hat{\Sigma}^{\gamma Z}(s) = \Sigma^{\gamma Z}(s) - \Sigma^{\gamma Z}(0) + s\left\{2\frac{\Sigma^{\gamma Z}(0)}{M_Z^2} - \frac{c_W}{s_W}\left(\frac{\delta M_Z^2}{M_Z^2} - \frac{\delta M_W^2}{M_W^2}\right)\right\} \tag{A.84}$$

$$\hat{\Sigma}^{Z}(s) = \Sigma^{Z}(s) - \delta M_Z^2 + \delta Z_2^Z(s - M_Z^2) \tag{A.85}$$

$$\hat{\Sigma}^{W}(s) = \Sigma^{W}(s) - \delta M_W^2 + \delta Z_2^W(s - M_W^2). \tag{A.86}$$

The renormalization constants are

$$\delta Z_2^{\gamma} = -\Pi^{\gamma}(0) \equiv \frac{\partial \Sigma^{\gamma}}{\partial s}(0) \tag{A.87}$$

$$\delta Z_2^{Z} = -\Pi^{\gamma}(0) - 2\frac{c_W^2 - s_W^2}{s_W^2 c_W^2}\frac{\Sigma^{\gamma Z}(0)}{M_Z^2} + \frac{c_W^2 - s_W^2}{s_W^2}\left(\frac{\delta M_Z^2}{M_Z^2} - \frac{\delta M_W^2}{M_W^2}\right) \tag{A.88}$$

$$\delta Z_2^{W} = -\Pi^{\gamma}(0) - 2\frac{c_W}{s_W}\frac{\Sigma^{\gamma Z}(0)}{M_Z^2} + \frac{c_W^2}{s_W^2}\left(\frac{\delta M_Z^2}{M_Z^2} - \frac{\delta M_W^2}{M_W^2}\right) \tag{A.89}$$

and

$$\delta M_W^2 = \mathrm{Re}\Sigma^{W}(M_W^2) \tag{A.90}$$

$$\delta M_Z^2 = \mathrm{Re}\Sigma^{Z}(M_Z^2). \tag{A.91}$$

Note, too, that

$$\Pi^{\gamma,\gamma Z,Z,W}(s) = \frac{1}{s}\mathrm{Re}\Sigma^{\gamma,\gamma Z,Z,W}(s) \tag{A.92}$$

$$\hat{\Pi}^{\gamma,\gamma Z,Z,W}(s) = \frac{1}{s}\mathrm{Re}\hat{\Sigma}^{\gamma,\gamma Z,Z,W}(s). \tag{A.93}$$

The unrenormalized vector boson self energies $\Sigma^{\gamma,\gamma Z,Z,W}$ contain terms of the form

$$\Delta_j = \frac{2}{4-D} - \gamma + \ln 4\pi - \ln\left(\frac{m_j^2}{\mu^2}\right), \tag{A.94}$$

where D is the number of dimensions used in the dimensional regularization, γ is the Euler constant, μ is a mass scale, and m_j is a particle mass. In the renormalized self energies, the singular and constant terms of Equation A.94 cancel, but the mass dependent terms remain. To simplify the calculations, the Δ_j terms in the unrenormalized self energies are replaced by terms of the form

$$\Delta'_f = -\ln m_f^2 \tag{A.95}$$

in which the singular and constant terms of Equation A.94 are removed and the (arbitrary) mass scale μ is set to 1. The abbreviated notation

$$z = M_Z^2, \qquad w = M_W^2, \qquad h = M_H^2 \tag{A.96}$$

is used to make the equations more compact. With these substitutions and abbreviations, the unrenormalized vector boson self energies are given by

$$\begin{aligned}
\Sigma^{\gamma}(s) \;=\; & \frac{\alpha}{4\pi}\Bigg\{\frac{4}{3}\sum_f N_f^C Q_f^2\left[s\Delta'_f + (s+2m_f^2)F(s,m_f,m_f) - \frac{s}{3}\right] \\
& -3\Delta'_W - (3s+4w)F(s,M_W,M_W)\Bigg\}
\end{aligned} \tag{A.97}$$

$$\begin{aligned}
\Sigma^{\gamma Z}(s) \;=\; & \frac{\alpha}{4\pi}\Bigg\{-\frac{4}{3}\sum_f N_f^C Q_f g_V^f\left[s\Delta'_f + (s+2m_f^2)F(s,m_f,m_f) - \frac{s}{3}\right] \\
& +\frac{1}{c_W s_W}\left[\left(3c_W^2 + \frac{1}{6}\right)s + 2w\right]\Delta'_W \\
& +\frac{1}{c_W s_W}\left[\left(3c_W^2 + \frac{1}{6}\right)s + \left(4c_W^2 + \frac{4}{3}\right)w\right]F(s,M_W,M_W) + \frac{s}{9c_W s_W}\Bigg\}
\end{aligned} \tag{A.98}$$

$$\begin{aligned}
\Sigma^{Z}(s) \;=\; & \frac{\alpha}{4\pi}\Bigg\{\frac{4}{3}\sum_{l=e,\mu,\tau} 2(g_A^l)^2 s\left(\Delta'_l + \frac{5}{3} - \ln(-\frac{s}{m_l^2} - i\epsilon)\right) \\
& \frac{4}{3}\sum_{f\neq\nu} N_f^C\Bigg[((g_V^f)^2 + (g_A^f)^2)\left(s\Delta'_f + (s+2m_f^2)F(s,m_f,m_f) - \frac{s}{3}\right) \\
& -\frac{3}{8c_W^2 s_W^2} m_f^2(\Delta'_f + F(s,m_f,m_f))\Bigg] \\
& \left[\left(3 - \frac{19}{6s_W^2} + \frac{1}{6c_W^2}\right)s + \left(4 + \frac{1}{c_W^2} - \frac{1}{s_W^2}\right)M_Z^2\right]\Delta'_W
\end{aligned} \tag{A.99}$$

$$
\begin{aligned}
&+\Big[\Big(-c_W^4(40s+80w)+(c_W^2-s_W^2)^2(8w+s)+12w\Big)F(s,M_W,M_W)\\
&\left(10z-2h+s+\frac{(h-z)^2}{s}\right)F(s,M_H,M_Z)-2h\ln\frac{h}{w}-2z\ln\frac{z}{w}\\
&+(10z-2h+s)\left(1-\frac{h+z}{h-z}\ln\frac{M_H}{M_Z}-\ln\frac{M_HM_Z}{w}\right)\\
&+\frac{2}{3}s\Big(1+(c_W^2-s_W^2)^2-4c_W^2\Big)\Big]\frac{1}{12c_W^2s_W^2}\Big\}
\end{aligned}
$$

$$
\begin{aligned}
\Sigma^W(s) \;=\;& \frac{\alpha}{4\pi}\frac{1}{s_W^2}\Bigg\{\frac{1}{3}\sum_{l=e,\mu,\tau}\Big[(s-\frac{3}{2}m_l^2)\Delta_l' \qquad\qquad (A.100)\\
&+\left(s-\frac{m_l^2}{2}-\frac{m_l^4}{2s}\right)F(s,0,m_l)+\frac{2}{3}s-\frac{m_l^2}{2}\Big]\\
&+\frac{1}{3}\sum_{q-doublets}\Big[\frac{\Delta_+'}{2}\left(s-\frac{5}{2}m_+^2-\frac{m_-^2}{2}\right)+\frac{\Delta_-'}{2}\left(s-\frac{5}{2}m_-^2-\frac{m_+^2}{2}\right)\\
&+\left(s-\frac{m_+^2+m_-^2}{2}-\frac{(m_+^2-m_-^2)^2}{2s}\right)F(s,m_+,m_-)\\
&+\left(s-\frac{m_+^2+m_-^2}{2}\right)\left(1-\frac{m_+^2+m_-^2}{m_+^2-m_-^2}\ln\frac{m_+}{m_-}\right)-\frac{s}{3}\Big]\\
&\left[\frac{19}{2}s+3w\left(1-\frac{s_W^2}{c_W^2}\right)\right]\Delta_W'\\
&\Big[s_W^4z-\frac{c_W^2}{3}\left(7z+7w+10s-2\frac{(z-w)^2}{s}\right)\\
&-\frac{1}{6}\left(w+z-\frac{s}{2}-\frac{(z-w)^2}{2s}\right)\Big]F(s,M_Z,M_W)\\
&+\frac{s_W^2}{3}\left(-4w-10s+\frac{2w^2}{s}\right)F(s,0,M_W)\\
&+\frac{1}{6}\left(5w-h+\frac{s}{2}+\frac{(h-w)^2}{2s}\right)F(s,M_H,M_W)\\
&\left[\frac{c_W^2}{3}(7z+7w+10s-4(z-w))-s_W^4z+\frac{1}{6}\left(2w-\frac{s}{2}\right)\right]\frac{z}{z-w}\ln\frac{z}{w}\\
&-\left(\frac{2}{3}w+\frac{s}{12}\right)\frac{h}{h-w}\ln\frac{h}{w}-\frac{c_W^2}{3}\left(7z+7w+\frac{32}{3}s\right)\\
&+s_W^4z+\frac{1}{6}\left(\frac{5}{3}s+4w-z-h\right)-\frac{s_W^2}{3}\left(4w+\frac{32}{3}s\right)\Bigg\}
\end{aligned}
$$

The function $F(s,m_1,m_2)$ is defined by the integral

$$
\begin{aligned}
F(s,m_1,m_2) \;=\;& -1+\frac{m_1^2+m_2^2}{m_1^2-m_2^2}\ln\frac{m_1}{m_2}\\
&-\int_0^1 dx\ln\frac{x^2s-x(s+m_1^2-m_2^2)+m_1^2-i\epsilon}{m_1m_2} \qquad (A.101)
\end{aligned}
$$

and has the analytic form [59]

$$
\begin{aligned}
F(s,m_1,m_2) &= 1+\left(\frac{m_1^2-m_2^2}{s}-\frac{m_1^2+m_2^2}{m_1^2-m_2^2}\right)\ln\frac{m_2}{m_1} \\
&\quad \begin{cases} +\frac{1}{s}\sqrt{\mu_+}\sqrt{\mu_-}\ln\frac{\sqrt{\mu_+}+\sqrt{\mu_-}}{\sqrt{\mu_+}-\sqrt{\mu_-}} & 0<\mu_- \\ -\frac{2}{s}\sqrt{\mu_+}\sqrt{-\mu_-}\arctan\frac{\sqrt{-\mu_-}}{\sqrt{\mu_+}} & \mu_-<0<\mu_+ \\ -\frac{1}{s}\sqrt{-\mu_+}\sqrt{-\mu_-}\left(\ln\frac{\sqrt{-\mu_+}+\sqrt{-\mu_-}}{\sqrt{-\mu_-}-\sqrt{-\mu_+}}-i\pi\right) & \mu_+<0 \end{cases}
\end{aligned}
\tag{A.102}
$$

where

$$\mu_+ = (m_1+m_2)^2-s \tag{A.103}$$

$$\mu_- = (m_1-m_2)^2-s. \tag{A.104}$$

There are more simple expressions for $F(s,m_1,m_2)$ for a few special cases. If one of the masses is zero, then

$$F(s,0,m)=1+\left(\frac{m^2}{s}-1\right)\ln\left(1-\frac{s}{m^2}-i\epsilon\right). \tag{A.105}$$

For small values of s ($s \ll m_1^2, m_2^2$),

$$F(s,m_1,m_2) = \frac{s}{(m_1^2-m_2^2)^2}\left(\frac{m_1^2+m_2^2}{2}-\frac{m_1^2m_2^2}{m_1^2-m_2^2}\ln\frac{m_1^2}{m_2^2}\right) \tag{A.106}$$

$$F(s,m,m) = \frac{s}{6m^2}, \tag{A.107}$$

while for large values of s ($s \gg m_1^2, m_2^2$),

$$F(s,m_1,m_2)=1-\ln\frac{s}{m_1m_2}+\frac{m_1^2+m_2^2}{m_1^2-m_2^2}\ln\frac{m_1}{m_2}. \tag{A.108}$$

References

[1] S.L. Glashow, Nucl. Phys. **B 22**, 579 (1961)

[2] S. Weinberg, Phys. Rev. Lett. **19**, 1264 (1967)

[3] A. Salam, in *Elementary Particle Theory*, edited by N. Svartholm (Almquist and Wiskell, Stockholm, 1968), p.367

[4] F. J. Hasert *et. al.*, Phys. Lett. **B46**, 138 (1973)

[5] G. Arnison *et. al.*, Phys. Lett. **B122**, 103 (1983)

[6] G. Arnison *et. al.*, Phys. Lett. **B126**, 398 (1983)

[7] J. Schwinger, Ann. of Phys. **2**, 407 (1957)

[8] M. Gell-Mann, Phys. Rev. **92**, 833 (1953);
K. Nishijima, Prog. Theor. Phys. **13**, 285 (1955)

[9] G. ‘tHooft, Phys. Lett. **B33**, 173 (1971); **B35**, 167 (1971)

[10] R. P. Feynman and M Gell-Mann, Phys. Rev. **109**, 193 (1958)

[11] V. D. Barger and R. J. N. Phillips, *Collider Physics* (Addison–Wesley, Reading, Massachusetts, 1987)

[12] G. Putzolu, Nuovo Cimento **20**, 542 (1961)

[13] R. W. Brown, K. O. Mikaelian and M. K. Gaillard, Nucl. Phys. **B 75**, 112, (1974)

[14] M. Böhm, W. Hollik, Nucl. Phys. **B 204**, 45 (1982)

[15] See, for example,

M.E. Levi et al., Phys. Rev. Lett. **51**, 1941 (1983)

W. Bartel et al., Phys. Lett. **B108**, 140 (1982)

B. Adeva et al., Phys. Rev. Lett. **48**, 1701 (1982)

H.J. Behrend et al., Phys. Lett. **B114**, 282 (1982)

[16] E. Eichten, I. Hinchliffe, K. Lane, and C. Quigg, Rev. Mod. Phys. **56**, 579 (1984)

[17] U. Amaldi et. al., Phys. Rev. **D 36**, 1385 (1987)

[18] M. Chaichian, M. Hayashi, and K. Yamagishi, Phys. Rev. **D 25**, 130 (1982)

[19] J.C. Collins and D.E. Soper, Phys. Rev. **D 16**, 2219 (1977)

[20] R. D. Peccei, DESY preprint DESY 89-043 (1989)

[21] S. van de Meer, Proceedings of the SLAC and Fermilab Summer Schools on the Physics of Particle Accelerators, edited by M. Dienes and M. Month, AIP Conference Proceedings **153**, American Institute of Physics, New York, 1987

[22] F. Abe *et. al.*, Nucl. Inst. and Meth. **A 271**, 387 (1988) and references contained therin.

[23] F. Abe *et. al.*, Phys. Rev. Lett. **63**, 720 (1989)

[24] G. S. Abrams *et. al.*, Phys. Rev. Lett. **63**, 724 (1989)

G. S. Abrams *et. al.*, Phys. Rev. Lett. **63**, 2173 (1989)

[25] Particle Data Group, to be published

B. Adeva *et. al.*, Phys. Lett. **B231**, 509 (1989)

D. DeCamp *et. al.*, Phys. Lett. **B231**, 519 (1989)

M. Akrawy *et. al.*, Phys. Lett. **B231**, 530 (1989)

P. Aarnio *et. al.*, Phys. Lett. **B231**, 539 (1989)

[26] E. Kearns, Ph.D. Thesis, Harvard University, 1990

[27] F. Paige and S.D. Protopopescu, BNL Report No. BNL 38034, 1986 (unpublished)

[28] F. Abe *et. al.*, Phys. Rev. Lett. **64**, 152 (1990)

[29] B. Winer, private communication

[30] L. Nakae, private communication

[31] R. D. St. Denis, Ph.D. Thesis, Harvard University, 1988

[32] I. Hinchliffe, in preparation

[33] F.E. James and M. Roos, Comput. Phys. Commun. **10**, 343 (1975)

[34] W. T. Eadie, D. Dryard, F. E. James, M. Roos, and B. Sadoulet, *Statistical Methods in Experimental Physics* (North–Holland, Amsterdam, 1971)

[35] J.P. Berge, private communication

[36] D.W. Duke and J.F. Owens, Phys. Rev. **D 30**, 49 (1984)

[37] M. Diemoz, F. Ferroni, E. Longo, and G. Martinelli, Z. Phys. **C 39**, 21 (1988)

[38] A. D. Martin, R. G. Roberts, and W. J. Stirling, Mod. Phys. Lett. **A 4**, 1135 (1989)

[39] R. J. Cashmore, C. M. Hawkes, B. W. Lynn, R. G. Stuart, Z. Phys. **C 30**, 125 (1986)

[40] D. A. Ross, J. C. Taylor, Nucl. Phys. **B 51**, 25 (1973)

[41] W. F. L. Hollik, DESY Preprint DESY 88-188

[42] W. J. Marciano, Phys. Rev. **D 20**, 274 (1979)
A. Sirlin, Phys. Rev. **D 22**, 971 (1980)
W. J. Marciano, A. Sirlin, Phys. Rev. **D 22**, 2695 (1980)

[43] P. Chiappetta, M. Le Bellac, Z. Phys. **C 32**, 521 (1986)

[44] J. Ng, private communication

[45] M. Greco, G. Pancheri-Srivastava, Y. Srivastava, Nucl. Phys. **B 171**, 118 (1980)

[46] F. A. Berends, K. J. F. Gaemers, R. Gastmans, Nucl. Phys. **B 63**, 381 (1973)

[47] M. Böhm, W. Hollik, in *Z Physics at LEP 1*, CERN 89-08, Volume 1, p 203, (1989)

[48] R. G. Wagner, unpublished

[49] F. A. Berends, R. Kleiss, Z. Phys. **C 27**, 365 (1985);
F. A. Berends *et. al.* Z. Phys. **C 27**, 155 (1985)

[50] M. Consoli, W. Hollik, in *Z Physics at LEP 1*, CERN 89-08, Volume 1, p 8, (1989)

[51] D. C. Kennedy and B. W. Lynn, SLAC pub 4039 (1986);
D. C. Kennedy and B. W. Lynn, Nucl. Phys. **B 322**, 1 (1988)

[52] D. Decamp *et. al.*, CERN preprint CERN-PPE/90-104, submitted to Z. Phys. **C**

[53] B. Adeva *et. al.*, L3 Preprint # 8 (1990)

[54] T. Müller, Fortschr. Phys. **37**, 339 (1989);
C. Albajar *et. al.*, Z. Phys. **C 44**, 15 (1989)

[55] F. Abe et. al., submitted to Phys. Rev. Lett.

[56] J. Alitti et. al., CERN preprint CERN-EP/90-22, submitted to Phys. Lett. **B**

[57] G. ‘tHooft, M. Veltman, Nucl. Phys. **B 153**, 365 (1979)

[58] F. A. Berends, R. Kleiss, S. Jadach, Nucl. Phys. **B 202**, 63 (1982)

[59] M. Böhm, W. Hollik, H. Spiesberger, Fortschr. Phys. **34**, 687 (1986)

Vita

Peter Todd Hurst was [redacted] [redacted] and spent his first 18 years there, graduating from [redacted]. He then enrolled at the Massachusetts Institute of Technology, and, for reasons which are not now entirely clear to him, majored in physics. He received his B.S. in physics from M.I.T. in 1985 and began graduate work at the University of Illinois in Urbana. In 1986 he earned his M.S. in physics, and completed his Ph.D. in 1990, after which he began to take himself far too seriously.